国際化推進共同研究概要

No. 1

20EA-1

タ イ ト ル： Dynamical mechanisms of stratospheric control on the tropical troposphere and ocean

研究代表者： UEYAMA Rei

所内世話人： 江口　菜穂

研究概要： ここ数10年間で西アフリカのサヘル域で顕著な降水現象が増加している。この降水トレンドのメカニズムを知るために、客観解析データ(JRA55)と衛星データから導出した熱帯対流圏界面に到達する積雲対流活動、およびメソスケール規模の対流活動の指標を用いて、解析を行った。西アフリカ上空では、対流圏は温暖化、下部成層圏は寒冷化していた。この傾向は温室効果ガスによる影響と一致するが、大西洋からの下層の水蒸気輸送による降水トレンドとは合致しない。背の高い積雲対流が活発となったサヘル域の上層では、気温の鉛直勾配が減少する一方、ギニア沿岸では対流圏が温暖化し、背の低い積雲活動が活発となっていた。西アフリカ域の降水トレンドの特徴は、成層圏循環場によって駆動された背の高い積雲対流活動に起因していることが示唆された。

Dynamical Mechanisms of Stratospheric Control on the Tropical Troposphere and Ocean

Rei Ueyama (NASA Ames Research Center)

I. Abstract

Extreme precipitation events in the Sahel region of West Africa have become more frequent over recent decades. We investigated the mechanism behind this recent precipitation trend using a combination of JRA-55 reanalysis, satellite precipitation measurements, and convection diagnostics including observations of tropical overshooting clouds and mesoscale convective systems.

We found that the recent changes over West Africa involve a cooling of the tropical lower stratosphere and tropopause layer, and a warming in the troposphere. This feature is similar to that which might result from increased greenhouse gas levels, but is distinct from the interannual variation of precipitation associated with the modulation of water vapor transport from the Atlantic Ocean. We suggest that the decrease in the vertical temperature gradient in the tropical tropopause region enhances extreme deep convection over the Sahel, where penetrating convection is frequent, whereas tropospheric warming suppresses the shallower convection over the Guinea Coast. The essential characteristic of the recent changes over West Africa is therefore the *depth* of convection, rather than the total amount of surface precipitation, which is largely driven by stratospheric forcing.

II. Introduction

West Africa is particularly susceptible to the impacts of climate change, with significant changes in the precipitation regime likely to occur over the next few decades (Gaetani et al., 2020). Assessing the role of the tropical tropopause layer (TTL; around 140–70 hPa) in driving precipitation trends is a valuable step towards improving our understanding of the present and future evolution of West African rainfall regimes.

Kodera et al. (2019) found that extreme deep convection in the ascending branch of the boreal summer Hadley circulation became active over recent decades, particularly over the African and Asian sectors. In West Africa, this increase in convective activity was associated with the recent recovery of rainfall over the Sahel following the long and severe drought conditions of the 1970s and 1980s. However, the recent increase in precipitation over the Sahel is not a simple recovery to the former wet state: The characteristics of rainfall have also changed, becoming more intense and intermittent. The analysis of mesoscale convective systems (MCSs) with cold cloud top temperatures (Taylor et al., 2017) corroborates the increasing intensity of deep convection over West Africa. Kodera et al. (2019) also note that the recent increase in tropical extreme deep convection occurred in association with a cooling of the tropical lower stratosphere, suggesting the possible role of TTL processes in the recent precipitation increase over the Sahel.

In this study, we demonstrate the importance of TTL processes in driving precipitation trends in West Africa.

III. Method/Data

We analyzed JRA-55 reanalysis data, surface precipitation measurements from Global Precipitation Climatology Project (GPCP), and deep convection diagnostics based on satellite observations of tropical overshooting clouds (COV). Our results are compared with occurrence frequencies of MCSs over the Sahel obtained by Taylor et al. (2017).

Preliminary analyses of satellite-derived convective cloud top altitudes (Pfister et al, 2021) were also used to corroborate the tropical convective overshooting cloud data. Our approach for calculating the convective cloud top altitudes is based on the assumption that rainfall, properly thresholded, can define the area where convection is occurring. These rainfall data, coupled with the infrared satellite information, can then define both the regions where the mass-transporting convective cores occur, and their altitude.

IV. Results

Precipitation during the summer monsoon season of July, August, and September (JAS) from the 1980s to the present increased over the Sahel (15°W–20°E, 12.5°N–17.5°N; Fig. 1c), but decreased over the Guinea Coast (15°W–20°E, 2.5°N–7.5°N; Fig. 1d). As such, surface precipitation does not exhibit a clear trend when averaged over the entire West African region (15°W–20°E, 2.5°N–17.5°N; (Fig. 1e).

A decreasing precipitation trend is particularly pronounced over the coastal regions west of the Guinea Highlands and South Cameroon Plateau (Fig. 1b). Over these elevated terrains, convergence of the air from the ocean results in heavy precipitation (Fig. 1a). Since convection over the coastal region is generally not deep enough to penetrate into the TTL, uplifted air diverges in the upper troposphere. In contrast, an increasing precipitation trend is found further inland in regions of high equivalent potential temperature near the surface, where extreme deep convective clouds with overshooting tops occur. This extreme deep convection over Sahel is also evident in the large horizontal divergence at higher levels in the TTL. These results suggest that the regional differences in recent precipitation trends (Fig. 1b) may arise from differences in convective activity. In particular, precipitation increased where extreme deep convection occurs frequently, but decreased where convection is relatively shallow. This implies the important role of the depth of convection in precipitation changes over the last few decades.

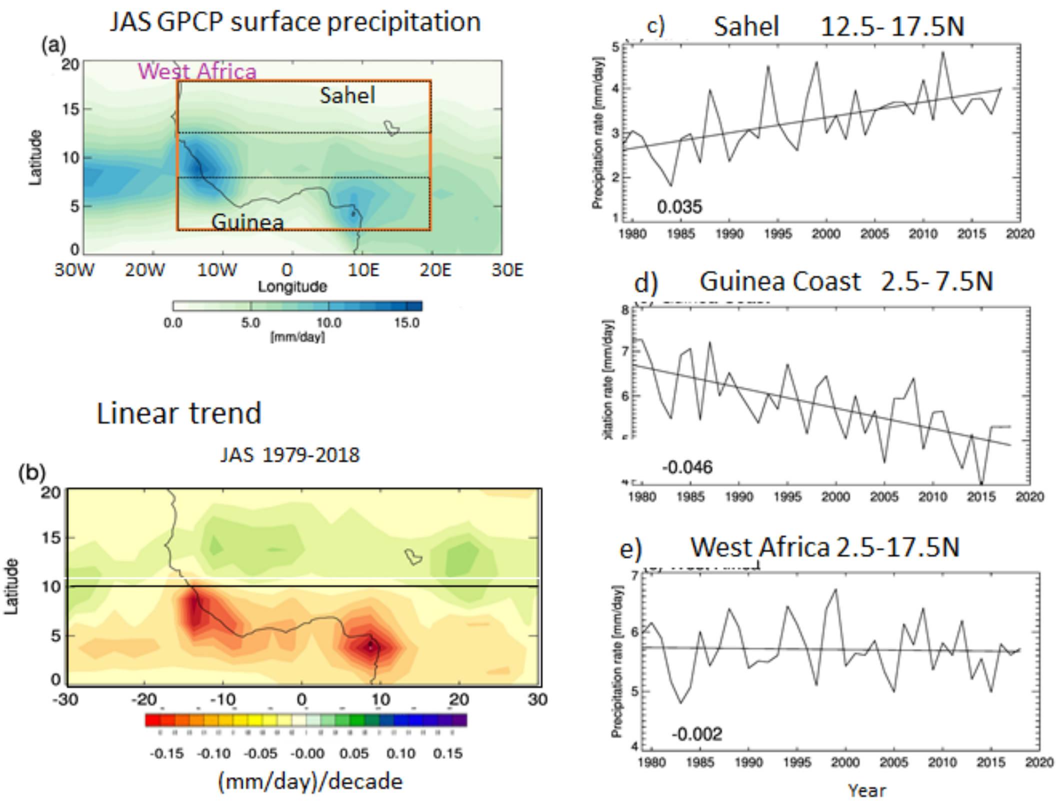

Figure 1: (a) Climatological mean surface precipitation over West Africa during JAS and (b) its linear trend over the period 1979–2018. (c, d, and e) Time series of JAS mean precipitation averaged over (c) the Sahel, (d) the Guinea Coast, and (e) West Africa. Lines and numbers indicate linear trend (mm/day/decade). Regions within West Africa are indicated by dotted lines within the brown box in (a).

Latitudinal differences between the two regions can clearly be seen in the meridional cross-section of JAS mean standardized temperature and vertical velocity anomalies shown in Figure 2. Although cooling in the TTL occurred over a wide range of latitudes, upwelling in the troposphere was enhanced only over the Sahel. This suggests that TTL cooling impacts only those regions where upwelling extends from the upper troposphere to the TTL (i.e., about 200 to 140 hPa), as indicated by the climatological divergence field (dotted lines). Figures 2b and 2c show the evolution of standardized COV frequencies during the period 2001–2018. The mean occurrence frequency of COV over the Sahel is 4.4 ‰, which is four times as large as that over the Guinea Coast. There is an increasing trend superimposed on the year-to-year variability in the COV occurrence frequency over the Sahel, which matches the evolution of MCSs with a cloud top temperature < −70°C reported by Taylor et al. (2017). In contrast, the COV occurrence frequency over the Guinea Coast exhibits a decreasing trend.

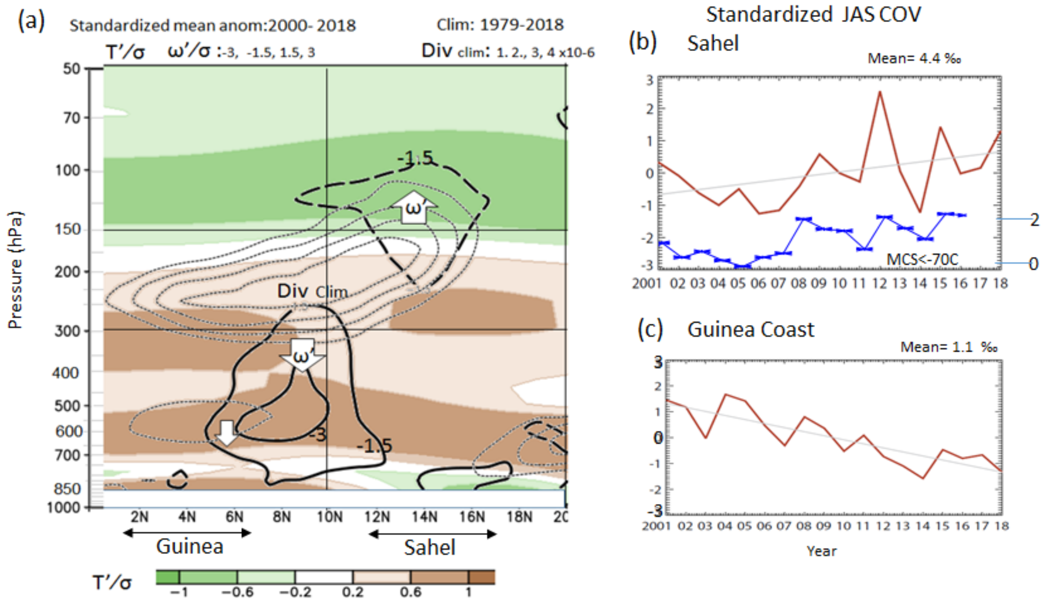

Figure 2: (a) Meridional cross-section of mean standardized anomalies for JAS 2000–2018 over the Sahel (15°W–20°E). Temperature and pressure vertical velocity are shown by color shading and contour lines, respectively. Climatology of the horizontal divergence is shown by dotted lines. (b, c) Standardized JAS mean COV occurrence frequency from 2001 to 2018 over (b) the Sahel and (c) the Guinea Coast. These two regions are indicated by the arrows along the x-axis of (a). Blue lines in (b) indicate the standardized JAS mean MCSs with cloud top temperature below −70°C from Taylor et al. (2017). Scale for the MCS is given on the right-hand side.

V. Discussion/Summary

The different precipitation trends seen over the Sahel and Guinea Coast can be interpreted as a result of the differences in the depth of convective clouds in the two regions. Penetrating deep convection over the Sahel is susceptible to temperature changes in the TTL and thus increases in response to TTL cooling. In contrast, convective activity over the Guinea Coast is not influenced by cooling in the TTL, but rather suppressed by warming in the troposphere. Therefore, the observed changes in TTL temperatures have led to an increasing precipitation trend over the Sahel, while it led to a decreasing precipitation trend over the Guinea Coast.

To better understand the details of the stratosphere–troposphere coupling process, we will investigate the coupling process as depicted in convective cloud top data (Pfister et al., 2021) in a future study. Specifically, the 0.25° longitude/latitude resolution, 3-hourly cloud top data will be useful for illustrating the time evolution of deep convective activity over a given region (e.g., Africa) in response to stratospheric forcing.

In this study, we analyzed vertical velocity and divergence data from the JRA-55 reanalysis. However, vertical velocity is not an observed variable and depends strongly on the model (i.e., the cumulus parametrization) used for the reanalysis. This is especially true in the TTL, where there is little observational data available. Preliminary analysis of the European Centre for Medium-Range

Weather Forecasts reanalysis data (ERA Interim and ERA 5) indicates that there is no clear increasing trend in the vertical velocity in the TTL over the Sahel. Further detailed verification of the reanalysis data is needed.

VI. References

Gaetani, M., S. Janicot. M. Vrac, A.M. Famien, and B. Sultan, 2020: Robust assessment of the time of emergence of precipitation change in West Africa. *Sci. Rep.*, **10**, 7670. https://doi.org/10.1038/s41598-020-63782.

Kodera, K., N. Eguchi, R. Ueyama, Y. Kuroda, C. Kobayashi, B.M. Funatsu, and C. Claud, 2019: Implication of tropical lower stratospheric cooling in recent trends in tropical circulation and deep convective activity. *Atmos. Chem. Phys.*, **19**, 2655-2669, doi:10.5194/acp-19-2655-2019.

Pfister, L., Ueyama R., Jensen E., and Schoeberl, M., 2021: A method for obtaining high frequency, global, IR-based convective cloud tops for studies of the tropical tropopause layer, in preparation.

Taylor CM, D. Belušić, F. Guichard, D.J. Parker, T. Vischel, O. Bock, P.P. Harris, S. Janicot, C. Klein, and G. Panthou, 2017: Frequency of extreme Sahelian storms tripled since 1982 in satellite observations. *Nature* **544**(7651): 475–478. doi: /10.1038/nature22069.

VII. List of Publications and Selected Presentations

- Kodera, K., Eguchi, N., Ueyama, R., Funatsu, B., Gaetani, M., and Taylor, C. (2021), The impact of tropical tropopause cooling on Sahelian extreme deep convection, *J. Meteor. Soc. Japan*, in review.
- Ueyama, R., E. Jensen, M. Krämer, L. Pfister, and M. Schoeberl (2020), Impact of convectively-detrained ice crystals on the humidity of the tropical tropopause layer during boreal winter, *PIRE-CIRRUS seminar*. (oral)
- Ueyama, R., E. Jensen, and L. Pfister (2020), Convective impact on the stratospheric-entry water vapor through the tropical UTLS in boreal winter and summer, *American Geophysical Union Fall Meeting 2020.* (oral)
- Ueyama, R., E. Jensen, and L. Pfister (2020), Convective impact on the stratospheric-entry water vapor through the tropical UTLS in boreal winter and summer, *American Meteorological Society Meeting 2021.* (oral)

VIII. Research meeting and discussion

Several virtual meetings with Rei Ueyama, Nawo Eguchi, and Kunihiko Kodera
Discussion topics:

- Relationship between sudden stratospheric warmings and typhoons
- JRA55 vs. ERA5 differences (e.g., omega trend at 150 hPa over Sahel)
- Update on ongoing research projects by each member of our group
- Future research topics to pursue together

IX. Additional information

Rei Ueyama has been on a reduced (75%) work schedule since March 2020 due to COVID-19 caregiving of two young children at home. Schools in San Mateo County, California, USA still remain closed. NASA has granted excused leave to employees with COVID-19 caregiving responsibilities. Due to this unprecedented circumstance, work capacity has been severely limited. All travel is still restricted so meeting in person was not possible this past year. However, we have maintained communication via email and virtual meetings.

X. Members

Rei Ueyama	NASA Ames Research Center
Nawo Eguchi	RIAM, Kyushu University
Kunihiko Kodera	Meteorological Research Institute

国際化推進共同研究概要

No. 2

20EA-2

タ イ ト ル： Turbulent mixing in the Kuroshio Current off Taiwan

研究代表者： JAN Sen

所内世話人： 遠藤　貴洋

研究概要：2018 年に開始された、国際化推進共同研究「Turbulent mixing in the Kuroshio current off Taiwan」では、昨年度に引き続き九州大学応用力学研究所にて研究集会を開催する予定であったが、コロナ禍のためオンラインで実施せざるを得なかった。それにも関わらず、海外から 5 名、日本から 15 名が参加し、黒潮が海山を乗り越えることで生じる強い乱流混合の時空間変動の解明を進めていく上で、有意義な国際研究集会となった。この共同研究の成果をもとに、国際誌へ論文 2 編が投稿された。

Report on 2020 RIAM International Joint Research Project

Turbulent mixing in the Kuroshio current off Taiwan

JAN, Sen (Institute of Oceanography, National Taiwan University)

Objective

Turbulent mixing in the ocean controls transport of heat, freshwater, dissolved gasses, and pollutants. Turbulent mixing is also of crucial importance for ocean biology, from determining the flow field for the smallest plankton to setting large-scale gradients of nutrient availability. Recent observations suggest that the interaction of large-scale, low-frequency geostrophic currents with steep topography produces a rich sub-mesoscale and mesoscale vorticity field, which initiates a cascade of energy down to small scales and turbulence. The Kuroshio off Taiwan is the very region where such processes are highly expected, especially over the I-Lan Ridge between Taiwan and Yonaguni Island, Japan (Figure 1). This joint research project, which started in 2018, aims to quantify the turbulent dissipation and associated nutrient transport in the Kuroshio current over the I-Lan Ridge.

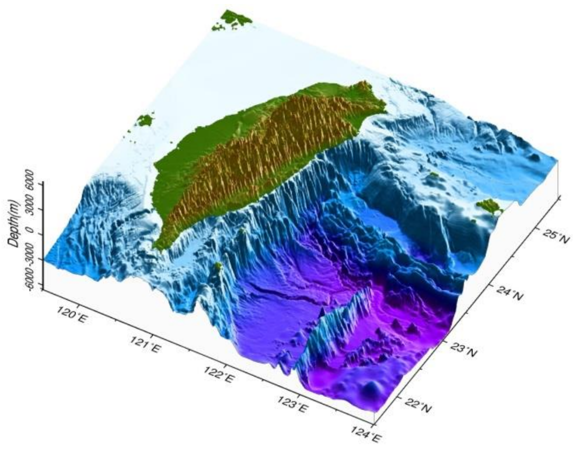

Figure 1. Bird's-eye view of bathymetry around the I-Lan Ridge. The Kuroshio current flows over the ridge to enter the East China Sea.

Research Plan

As part of this joint research project (18EA-2 and 19EA-3), we have carried out the field experiment over the I-Lan Ridge using R/Vs Ocean Researcher I and II (OR1 and OR2) and Legend. The RIAM researchers joined the OR1 and Legend cruises to deploy their microstructure profiler, TurboMAP, and our tow-yo microstructure profiler, VMP-250, respectively. Through the intercomparison of these microstructure data in the research workshop held in January at RIAM, we quantified the turbulent dissipation and associated nutrient transport in the Kuroshio current over the I-Lan Ridge as well as their downstream extent. In this fiscal year, we try not only to summarize our joint research but also to share and discuss turbulent mixing processes in the Kuroshio current over various kinds of bottom topography besides I-Lan ridge with Japanese researchers.

The members involved in this collaborative research and their roles are:

- JAN, Sen (NTU, Professor): Representative person
- YANG, Yiing Jang (NTU, Associate Professor): Analysis of the mooring data
- CHANG, Ming-Huei (NTU, Associate Professor): Analysis of the VMP-500 data
- CHEN, Jia-Lin (National Cheng Kung University, Assistant Professor): Numerical modelling using OpenFOAM
- CHENG, Yu-Hsin (NTU, Post-doc Researcher): Analysis of the VMP-500 and satellite data
- GUO, Xinyu (Ehime University, Professor): Numerical modelling using POM

- NAGAI, Takeyoshi (Tokyo University of Marine Science and Technology, Assistant Professor): Analysis of the tow-yo microstructure profiler data
- MATSUNO, Takeshi (RIAM, Emeritus Professor): Analysis of the TurboMAP data
- SENJYU, Tomoharu (RIAM, Associate Professor): Analysis of the mooring data
- ENDOH, Takahiro (RIAM, Associate Professor): In charge of the collaborative research
- TSUTSUMI, Eisuke (The University of Tokyo, Project Assistant Professor): Numerical modelling using MITgcm

Summary of collaborative research

Due to the COVID-19 pandemic, the workshop planned to be held at RIAM had to be changed to the online meeting entitled "Online meeting on turbulent mixing in the Kuroshio current over the topography", which was held on January 26 and 27, 2021. Associated with this, all the research budget provided for travel expenses has been returned. In addition to the members of our joint research project listed above, we invited two student speakers

- JIE, Gao (Ehime University, Doctoral Student)
- DURAN, Silvana (Tokyo University of Marine Science and Technology, Master's Student),

who study the biogeochemical responses to the turbulent mixing generated by the interaction of the Kuroshio current with an island and near-inertial internal gravity waves, respectively. In total, five overseas researchers as well as 15 Japanese researchers and students attended this online meeting. We discussed diversity and universality in the turbulent mixing generated by the interaction of the Kuroshio current with various topographic features (Figure 2).

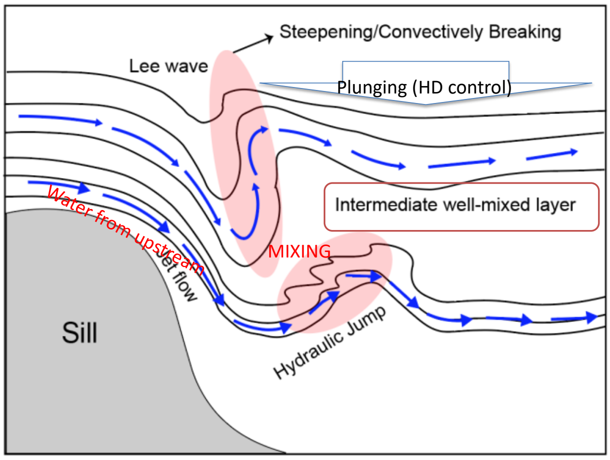

Figure 2. Schematic of the small-scale features resulting from the interaction between the Kuroshio and the I-Lan Ridge (adapted from the presentation by Dr. Ming-Huei Chang of NTU).

Based on this joint research project, the following two articles have been submitted to international journals.

1. CHANG, Ming-Huei, et al., Observations of Kuroshio flowing over a sill: small-scale processes and turbulent mixing, submitted in January, 2021.
2. NAGAI, Takeyoshi, et al., The Kuroshio flowing over seamounts and associated submesoscale flows drive 100-km-wide 100-1000-fold enhancement of turbulence, submitted in February, 2021.

The program of the online meeting is attached below.

Online meeting on turbulent mixing in the Kuroshio current over the topography

Time Table in JST

January 26 (Tue.)

14:30 Opening remarks

14:35 Sen Jan (IONTU): Update of the result from direct TKE dissipation rate measurements off Taiwan with the data collected in 2020

15:05 Ming-Huei Chang (IONTU): Observations of Kuroshio flowing over a sill: small-scale processes and turbulent mixing

15:35-45 Break

15:45 Jia-Lin Chen (NCKU): Mixing enhancement modulated by unsteady shear flow in the Kuroshio above a system of seamounts

16:15 Eisuke Tsutsumi (AORI): An updated analysis on the observation and numerical modeling of turbulent mixing in the I-Lan ridge

January 27 (Wed.)

10:00 Takeyoshi Nagai (TUMSAT): The Kuroshio Nutrient Stream, where the diapycnal mixing matters

10:35 Silvana Duran (TUMSAT): Elevated nutrient supply caused by an approaching Kuroshio to the southern coast of Japan

11:05 Jie Gao (CMES): Occurrence of phytoplankton bloom as the Kuroshio passes an island

11:35- Discussion and Closing remarks

国際化推進共同研究概要

No. 3

20NU-1

タ イ ト ル： Numerical simulation of EC and EBW in QUEST

研究代表者： BERTELLI Nicola

所内世話人： 出射　浩

研究概要:　コロナ禍の影響で研究代表者は来日できなかったが、本共同研究課題は、遠隔で開催された別課題の「Plasma start-up and sustainment in spherical tokamak configuration by RF」に関するワークショップでのQUEST に関する発表で議論された。
議論された QUEST に関する発表は、出射 浩：「QUEST における相対論的ドップラーシフト効果に基づく第２高調波電子サイクロトロン加熱の速度空間での制御」である。

Numerical simulation of EC and EBW in QUEST

BERTELLI Nicola
(Princeton University, U.S.A)

I could not visit Research Institute for Applied Mechanics in Kyushu University due to the Corona pandemic. This collaboration subject was discussed at the QUEST talk in the remote workshop on "Plasma start-up and sustainment in spherical tokamak configuration by RF" that is a different joint international research subject.

The related QUEST talk is as follows.

"Momentum-space control on relativistic Doppler-shifted resonance in second harmonic ECH on QUEST" by H. Idei

The 28 GHz heating equipment of the launcher system with a focusing / steering mirror and the quasi-optical polarizer system has been developed to conduct the EC plasma ramp-up with local heating effect, or real and momentum space control. Heating and ramp-up scenario were assessed following TASK/WR ray-tracing analysis (with full relativistic-effect) and resonant momentum pitch analysis. The refractive indexes in parallel to the magnetic field $N_{//}$s were scanned to control the resonant momentum space. In the larger $N_{//}$ case, the energetic electrons were effectively generated, and ramped plasma current became large. In the smaller $N_{//}$ case (~0.1), the bulk electrons were heated up to 500 eV at ~1-2 x 10^{18}m^{-3}.

国際化推進共同研究概要

No.4

20NU-2

タイトル：Plasma start-up and sustainment in spherical tokamak configuration by RF

研究代表者：SHEVCHENKO　Vladimir

所内世話人：出射　浩

研究概要：高温プラズマ理工学研究センターで毎年開催され、これまでに８回を数えるワークショップを遠隔会議として実施した。英国の研究者が応用力学研究所・国際推進共同研究としてワ ークショップを開催している。これまでも一部の発表はリモートで実施されていたが、今回は、ワークショップ参加者が見込めないため、３日間、１４件の講演を全て遠隔会議で実施した。英国、米国からの参加があることから、大きな時差がある中での開催であったが、「Plasma start-up and sustainment in spherical tokamak configuration by RF」につき、活発に最新の実験データ・解析、理論計算が議論された。ワークショップには、センターの海外連携分野の研究者も参加しており、QUEST 実験への提言、コメントも頂いている。

Plasma start-up and sustainment in spherical tokamak configuration by RF

SHEVCHENKO Vladimir
(Tokamak Energy Ltd., United Kingdom)

A workshop on “Plasma start-up and sustainment in spherical tokamak configuration by RF” was held remotely as follows because no participants to the workshop were expected due to Corona pandemic.

Agenda (25th to 27th Jan. in 2021)

Monday 1/25

JST 20:00 / GMT 11:00 / EST 6:00 [+ 10 min.]

Vladimir Shevchenko / Hanada

WS purpose and agenda

JST 20:10 / GMT 11:10 / EST 6:10 [+ 40 min.]

Yuichi Takase

Survey of RF research on TST-2

JST 21:00 / GMT 12:00 / EST 7:00 [+ 30 min.]

Akira Ejiri

Electron temperature and density profile measurements by Thomson scattering systems on TST-2 and QUEST

JST 21:30 / GMT 12:30 / EST 7:30 [+ 40 min.]

Kazuaki Hanada

Historical Progress on QUEST for steady operation
- What we could obtain? -

JST 22:10 / GMT 13:10 / EST 8:10 [+ 30 min.]

Makoto Hasegawa

Extension of Operation Region for Steady State Operation on QUEST
by Integrated Control with Hot Walls

Tuesday 1/26

JST 21:00 / GMT 12:00 / EST 7:00 [+ 40 min.]

Vladimir Shevchenko

ECRH & CD in spherical tokamaks

JST 21:40 / GMT 12:40 / EST 7:40 [+ 20 min.]

Erasmus du Toit

Developing a 0D model for studying EBW start-up in MAST

JST 22:00 / GMT 13:00 / EST 8:00 [+ 30 min.]

Syunichi Shiraiwa

Recent development in Petra-M FEM framework and application to tokamak experiments

JST 22:30 / GMT 13:30 / EST 8:30 [+ 30 min.]

Nicola Bertelli

High harmonic fast wave simulations in NSTX-Upgrade by using the Petra-M FEM framework

JST 23:00 / GMT 14:00 / EST 9:00 [+ 30 min.]

Masayuki Ono

Multi-Mode Excitation in Radio-Frequency Heating and Current Drive

---

Wednesday 1/27

JST 20:00 / GMT 11:00 / EST 6:00 [+ 30 min.]

Naoto Tsuji

Electron cyclotron heating assisted Ohmic start-up in the trapped particle configuration on spherical tokamaks

JST 20:30 / GMT 11:30 / EST 6:30 [+ 30 min.]

Hiroshi Idei

Momentum-space control on relativistic Doppler-shifted resonance in second harmonic ECH on QUEST

JST 21:00 / GMT 12:00 / EST 7:00 [+ 30 min.]

Ryuya Ikezoe

Development of a magnetic fluctuation measurement system on QUEST

JST 21:30 / GMT 12:30 / EST 7:30 [+ 30 min.]

Takeshi Ido

Design of a Heavy Ion Beam Probe for QUEST

JST 22:00 / GMT 12:30 / EST 7:30 [+ 30 min.]

Kengo Kuroda

Initial results from high-field-side Transient CHI start-up on QUEST

JST 22:30 / GMT 12:30 / EST 7:30 [+ 10 min.]

Vladimir Shevchenko / Hanada

Closing Remarks

Summary

Yuichi Takase

Survey of RF research on TST-2

RF experiments performed on TST-2 were reviewed. TST-2 started operation in 1999 on the Hongo Campus of U. Tokyo. During initial operation, plasma current of nearly 100 kA was achieved by OH operation, and ST plasma formation with 1 kA plasma current was achieved by 1 kW of ECH at 2.45 GHz. TST-2 was moved to Kyushu University in 2003 to perform EBW experiments at 8.2 GHz with 200 kW power. X-B mode conversion heating with up to 70% heating efficiency was demonstrated, and a steady state current of 4 kA was maintained. A plasma ramp-up scenario using RF and vertical field ramp was developed and applied to JT-60U where a formation of advanced tokamak with up to 90% bootstrap current fraction was demonstrated. TST-2 was moved to the Kashiwa Campus of U. Tokyo and resumed operation in 2005. It was shown that the formation of ST configuration by pressure driven current is possible using lower frequency RF waves (21 MHz, 200 MHz). Electron heating by HHFW at 21 MHz was demonstrated. Current drive by LHW at 200 MHz was developed using different methods of wave excitation, inductively coupled combline antenna, dielectric loaded waveguide antenna, and capacitively coupled combline antenna (outboard launch and top launch). The highest plasma current was achieved by top launch LHW, consistent with GENRAY/CQL3D modelling. Further improvements are expected at higher toroidal field based on both experimental and computational results. A new type of travelling wave antenna (finline antenna) is being developed for use at 2.45 GHz.

Akira Ejiri

Electron temperature and density profile measurements by Thomson scattering systems on TST-2 and QUEST

TS systems have been constructed and operated for TST-2 and QUEST. The systems can measure 5+5 (TST-2) / 6+6 (QUEST) spatial points with 6 wavelength channels. The minimum measurable density is around 1x1017m-3, and the systems suitable for RF driven low density plasma in TST-2 and QUEST.

RF induced transport model has been introduced to explain the HX spectra, central temperature and response of RF turn off. Some features can be explained by the model, and some cannot be.

A double pass TS scheme is under development to measure temperature anisotropy of bulk electrons in RF driven plasmas. Theoretical work on the scheme was done to find optimum configuration.
Increasing measurement days in QUEST is important, and some efforts were made, and some are in progress/preparation.

Kazuaki Hanada

Historical Progress on QUEST for steady operation

- What we could obtain? -

We could successfully promote steady state operation of tokamak with QUEST which has all-metal plasma facing walls and a hot wall more than 10 years. It found that hydrogen transport barrier is formed between a plasma-induced deposition layer and a substrate made of metal, which plays an essential role in fuel particle recycling. The hydrogen barrier gives rise to presence of new time constant for steady state operation which is related to the surface recombination coefficient. We have developed the way of monitoring of the value shot by shot using fuel emission just after the plasma termination. The method can be applied to all the plasma experimental devices.
Temperature dependence of surface recombination coefficient is a key to handle particle balance and the time constant. We have demonstrated that the higher wall temperature provides faster wall saturation and it leads to shorter pulse length. To overcome the difficulty, wall temperature control is a candidate. Recently, several 6 hours discharges could be obtained and we confirm that wall temperature control is a promising way to extend the pulse duration due to regulation of fuel particle balance.
In near future, we will try to achieve longer discharges under the high temperature relevant to fusion reactors.

Makoto Hasegawa

Extension of Operation Region for Steady State Operation on QUEST
by Integrated Control with Hot Walls

The plasma first wall could be maintained at a temperature over 600 K. Long plasma discharge over 6 hours could be obtained under a high temperature environment of 473 K with hot wall of APS-W and CS of SUS. The control of particle supply is sensitive to temperature changes in the first wall (HW and CS). Detailed temperature control of the first wall leads to an increase in operating area.

Vladimir Shevchenko

ECRH & CD in spherical tokamaks

In February-March 2020 there was a short experimental campaign P2.1 on ST40. This campaign was conducted to re-confirm operational status of ST40 after re-commissioning. After that several new diagnostics have been installed and commissioned. Solenoid and additional vertical field power supplies were installed and tested. 0.6 MW 25 keV Heating Neutral Beam (HNB) injector has been tested and installed. Some plasma heating and fuelling were observed with HNB injection into plasmas. To date plasma currents achieved in ST40 are above 0.5 MA with the current flattop up to 100 ms. Toroidal fields close to 2 T at the major radius of 0.4 m have been delivered on a regular basis. Kiloelectron volt range electron and ion temperatures have been regularly achieved during this campaign. All diagnostics were commissioned and prepared for full scale experiments. Currently, installation of liquid nitrogen cooling for TF and Bv coils is completed. Next experimental campaign P2.2 is prepared to achieve first plasma in February 2021.
Further upgrades of ST40 include installation of the 2nd HNB 1 MW 50 keV. It was commissioned and prepared for experiments with plasma. The contracts for two dual (140/105 GHz) frequency 1 MW gyrotrons were placed and first of them is scheduled for delivery in Q3 2021. Capabilities of limitations of ECRH and CD at both frequencies were discussed in relation to ST40 and the future project ST-F1.

Erasmus du Toit

Developing a 0D model for studying EBW start-up in MAST

Electron Bernstein wave (EBW) start-up, including the generation of a plasma current and formation of closed flux surfaces (CFS), was successfully demonstrated in the spherical tokamak MAST [1]. The formation of CFS is a crucial part of start-up, and, while various mechanisms have been proposed to explain their formation, no detailed theoretical studies have previously been undertaken to study the time-evolution of the plasma current and formation of CFS. In this work, we present a simple model that explains the experimental observations in terms of the underlying physics, by studying the time evolution of the electron distribution function under a number of effects, including an electron source, orbital losses, collisions, EBW heating, and plasma induction.
Simulations show good agreement with experiments, providing explanations for several experimentally observed effects, including the current drive mechanism and role of the vacuum magnetic field. In particular, we show that collisions are responsible for only a

small part of the current drive. The open magnetic field line configuration during start-up, which leads to an asymmetric confinement of electrons [2] and is controlled by the vacuum magnetic field, is responsible for the majority of the generated plasma current.

[1] V.F. Shevchenko et al., EPJ Web of Conf. 87, 02007 (2015).
[2] T. Yoshinaga et al., Phys. Rev. Lett. 96, 125005 (2006).

Syunichi Shiraiwa

Recent development in Petra-M FEM framework and application to tokamak experiments

We present the recent progress of Petra-M framework development. Petra-M is a finite element (FEM) analysis platform we are developing for the integrated RF modeling. The goal is to realize the full wave RF simulation which includes the entire tokamak plasma from antenna to the hot core region with high physics and geometrical fidelity. Petra-M uses the MFEM finite element library developed by LLNL for the FEM assembly and combine it with other Open Source software including ASCR developed efficient linear solvers and meshing algorithm. This year. significant development was made to enhance its geometry editing capability, allowing for creating the detailed antenna structure based on the information directly imported from the CAD software. We also extend our usage of the high order finite element basis to reduce the total degree of freedoms, which allows for resolving the high harmonic fast waves in the entire NSTX-U device for the first time. The verification and validation effort of Petra-M models are in progress through domestic and international collaborations. This collaboration network covers the almost all RF waves including ICRF, HHFW, Helicon and LH waves and major tokamak experimental facilities worldwide, which makes the extensive test of our simulation platform possible. Potential path to incorporate the arbitrary order finite Larmor radius (FLR) effects to FEM wave simulation is discussed. Initial test in the 1D geometry using the O-X-B mode conversion scenario foreseen on NSTX-U is consistent with the dispersion relation, and extension to 2D/3D is in progress.

Nicola Bertelli

High harmonic fast wave simulations in NSTX-Upgrade by using the Petra-M FEM framework

In this work we present the recent applications of the Petra-M finite-element-method (FEM) platform to NSTX-Upgrade. Petra-M code [1] is a state-of-the-art generic electromagnetic simulation tool for modeling RF wave propagation based on MFEM [http://mfem.org], open source scalable C++ finite element method library. This paper shows the full 3D NSTX-U device geometry including realistic antenna geometry and 3D scrape-off-layer (SOL) plasma in order to capture the 3D effects and the antenna-plasma interaction in the SOL plasma and, at the same time, the core wave propagation. The antenna geometry and the 3D NSTX-U geometry are from the NSTX-U CAD models.

A first ever HHFW full wave simulation for the full 3D NSTX-U torus has been shown [2]. A scan of the antenna phasing shows a strong interaction between FWs and the SOL plasma for lower antenna phasing, which is consistent with previous NSTX HHFW observations. A large electric field is found on the wall surface even far away from the antenna region. This quantity will be important, as a next step, for studying the antenna impurity generation and RF sheath effects. The evaluation of the launching wave spectra for three antenna phasing have been also presented. Such spectra are consistent with the RF wave theory. A comparison between the scattering matrix (S-matrix) between vacuum and plasma cases has been discussed. The S-matrix evaluation is the first step to be able to quantify the HHFW antenna performance and compared it with the measurements. Finally, we have discussed the PPPL-MIT collaboration on direct RF power level utilizing the RF probes installed on NSTX-U.

[1] S. Shiraiwa et al., EPJ Web of Conferences 157, 03048 (2017).
[2] N. Bertelli, S. Shiraiwa, et al, AIP Conf. Proceeding 2254, 030001 (2020).

Masayuki Ono

Multi-Mode Excitation in Radio-Frequency Heating and Current Drive

While the rf actuators are potentially quite attractive for use in fusion reactor systems particularly with the technology and economic advantages, there are quite significant rf-plasma interaction related issues still require improved understanding and predictive capabilities in order for the rf actuators to become the mainstream fusion reactor components. The main challenges for rf actuators is that the antenna or waveguide launcher is placed at the plasma edge where the plasma density is essentially zero. Then the launched waves much traverse the so-called plasma scrape-off layer where the density increases from zero to $10^{19}/m^3$ in a short distance of a few cm. Because of the large variation in the density, the full wave equations must be solved from antenna/launcher to the plasma core. There are also a large variation in the electron and ion temperatures. The rf actuators are presently in three frequency ranges: ECH (electron cyclotron heating) using gyrotrons in 28 -170 GHz, LHCD (lower hybrid current drive) in 2 – 8 GHz range, and ICRF (ion cyclotron range of frequency) in 10 – 140 MHZ ranges. More recently, helicon experiments are being performed in the 500 MHz range. It is also recognized that for the same wave frequency range, there is a possibility of exciting multiple modes. For

ECH, it is well known that there are X-mode and O- mode which can be excited. The X-mode and O-mode excitation can be controlled to a large extent by controlling the polarization and injection angle of the launched waves. In addition, EBW (electron Bernstein wave) excitation is possible. The EBW is considered for its accessibility to the high-density regime above the so-called ECH cut-off density limit. For helicon regime, it is also well known that there are both electromagnetic wave (“helicon”) and electrostatic electron plasma wave (EPW) which is the LHCD wave. Recent wave modeling work at PPPL showed that both helicon and LHCD waves can be excited simultaneously [1]. Our analyses found that the edge density profile is highly important for the EPW excitation. In particular, the density “gap” if created in front of the antenna can lead to a significant EPW excitation even for a perfectly aligned antenna. For HHFW/ICRH, there are also fast electromagnetic (FW) wave and electrostatic EPWs including the IBW (ion Bernstein wave) branches. Since the EPW waves can exists at the low-density edge region of the plasma even for the ICRF frequency range, it is important to includes those electrostatic waves to fully understand the rf coupling physics. One of the challenges of the rf coupling problem for the electrostatic waves is the treatment of the so-called “S”-resonance [2] where the cold plasma approximation breaks down. The FLR effects would lead to the IBW excitation at the “S” resonance. This suggests the potential importance of including the FLR effects in assessing the viability of rf actuators. The wave equations with the FLR effects have been developed for multiple harmonics. Once such wave equations are validated, it is then possible to incorporate them into the Petra-M 3-D full wave code [3] to obtain the full picture of the rf actuator wave coupling physics.

[1] Kim, E.-H., M. Ono, N. Bertelli, S. Wang, and H. K. Park (2020), AIP Conf. Proceeding 2254, 050010 (2020); https://doi.org/10.1063/5.0013978

[2] T.H. Stix, Waves in Plasmas (American Institute of Physics, New York, 1992).

[3] S. Shiraiwa, N. Bertelli, et. al., at this workshop.

Naoto Tsuji

Electron cyclotron heating assisted Ohmic start-up in the trapped particle configuration on spherical tokamaks

TST-2 experiment showed that breakdown became slower when electron cyclotron (EC) waves were applied to the start-up in the conventional field-null configuration. Prompt breakdown was recovered when the trapped-particle configuration (TPC) was used instead of the field-null configuration. A simple numerical analysis showed that breakdown indeed became slower at low neutral pressure and high EC power, consistently with the experimentally observed trends.

Hiroshi Idei

Momentum-space control on relativistic Doppler-shifted resonance in second harmonic ECH on QUEST

The 28 GHz heating equipment of the launcher system with a focusing / steering mirror and the quasi-optical polarizer system has been developed to conduct the EC plasma ramp-up with local heating effect, or real and momentum space control. Heating and ramp-up scenario were assessed following TASK/WR ray-tracing analysis (with full relativistic-effect) and resonant momentum pitch analysis. The refractive indexes in parallel to the magnetic field $N_{//}$s were scanned to control the resonant momentum space. In the larger $N_{//}$ case, the energetic electrons were effectively generated, and ramped plasma current became large. In the smaller $N_{//}$ case (~0.1), the bulk electrons were heated up to 500 eV at ~1-2 x $10^{18}m^{-3}$.

Ryuya Ikezoe

Development of a magnetic fluctuation measurement system on QUEST

Poloidal and toroidal arrays of pick-up coils have been firstly installed inside the QUEST vacuum vessel. Abrupt decrease in plasma current and corresponding variation of equilibrium field were measured. Prompt loss of energetic electrons might be related. High-frequency waves driven by energetic electrons in a whistler band has been measured in a spherical tokamak. RF pick-up coils installed at HFS and at the fast-reciprocating probe head have shown various features of high-frequency wave activities.

In the future, multi-channel data acquisition system will be operated in the next campaign to get all the pick-up coil signals at the same time. A dedicated experiment using the developed fast-reciprocating RF probes and HFS RF probes is planned in next February. Detailed analyses will be done to characterize the high-frequency waves driven by energetic electrons on QUEST and elucidate the physics behind. Continues to develop a nice wave measurement environment, control knobs for energetic electrons, and distribution function diagnostics.

Takeshi Ido

Design of a Heavy Ion Beam Probe for QUEST

Heavy Ion Beam Probe (HIBP) has been designed for QUEST to investigate physical mechanism of the particle and heat transport in plasmas. The injected probe beam for the HIBP on QUEST is singly charged cesium ions (Cs+), and the required beam energy ranges from 10 keV to 50 keV. By controlling the beam energy and incident angle of the probe beam, measurable area covers the upper half of the QUEST plasmas. According to the numerical calculation, the intensity of the detected beam current is large enough to measure micro turbulences at the central region of plasmas with the density of 1 x 10^{19} (m^{-3}) or less.

Kengo Kuroda

Initial results from high-field-side Transient CHI start-up on QUEST

T-CHI current start-up by using newly designed simple electrode has made important progress. Flux evolution from the LFS and HFS T-CHI were examined. The potential for flux evolution with a narrow footprint appears to be possible using HFS T-CHI compared to that for LFS T-CHI. Some anticipated HFS T-CHI improvements were observed on the modified system with in-vessel coil and cylinder electrode. On the low injector flux configuration, camera images suggest a persisting plasma although a confined plasma current is unclear. On the high injector flux configuration, current up to 35 kA was generated in plasma that evolved only to the mid-plane (full growth into vessel should rapidly increase the generated toroidal current for the same injector current). Optimization of gas injection system on the modified electrode configuration are planed for next tasks. This is necessary to make sure CHI initiation happens in the injector region while preventing absorber arc for formation.

国際化推進共同研究概要

No. 5

20NU-3

タ イ ト ル： High power mm wave transmission line technology for advanced fusion devices

研究代表者： LECHTE Carsten Hanno

所内世話人： 出射　浩

研究概要： ITER プラズマでの不安定性抑制のための大電力・高周波デバイスの開発を進めている。これまでに九州大学でデバイスの低電力試験を、量子科学技術研究開発機構・那珂核融合研究所で大電力試験を実施している。今年度、高周波電界の偏波面を変えて行う実験を実施する予定であったが、海外からの研究者の参加が見込めない中、遠隔会議を重ねることで、偏波面制御デバイスの開発（ドイツ）、据付・大電力試験（那珂核融合研究所）を進め、偏波面制御でこれまで起きていたアーキング現象を大幅に軽減することに成功した。遠隔会議での議論、遠隔支援のもとで実験を実施し、共同研究を推進した。

High power mm wave transmission line technology for advanced fusion devices

LECHTE Carsten Hanno
University of Stuttgart, Germany

The FAst DIrectional Switch (FADIS) system has been studied for ITER application at 170 GHz as a topic under joint international research framework at Research Institute for Applied Mechanics in Kyushu University. The system device was developed at University of Stuttgart, Germany, and shipped to Kyushu University in 2018. Basic performance was tested at low power level in Kyushu University, and shipped to Naka Institute of National Institutes for Quantum and Radiological Science and Technology in 2019. High power tests were conducted in Naka Institute along the low power test results in Kyushu University.

The incident wave-polarization has to be controlled for proper FADIS performance. The optimum incident wave into the FADIS is a linear-polarized wave with an azimuthal angle in the horizontal-vertical wave-field plane. The quarter wavelength polarizer (rotator) in Kyushu University was used to control the azimuthal angle of the polarization. The performance of the rotator was tested at the low power test facilities in Kyushu University. Although the azimuthal angle was properly controlled with the rotator, the ellipticity was also changed by setting of the azimuthal angle. The controlled wave was an elliptically polarized-wave, and not the optimum linearly polarized-wave. The FADIS system was installed at the transmission line of the high-power test-stand with the rotator in Naka Institute. Although the FADIS performance was tested at the high-power test-stand in Naka Institute, but we had many unwanted arcing events inside the FADIS.

To avoid the arcing events in the FADIS, a universal polarizer has been developed at University of Stuttgart. The universal polarizer can control the azimuthal angle of the polarization without changing of the ellipticity by rotating the device on the transmission-line axis. The optimum linearly polarized-wave can be excited with the universal polarizer. Figure 1 shows a photo and a drawing of the universal polarizer. It was tested at the low power level in University of Stuttgart, and shipped to Kyushu University. It was finally shipped to Naka Institute, and installed at the transmission line of the high-power test-stand. Figure 2 illustrates setup of the universal polarizer in the transmission. The polarizer was set with an angle of 17.65 degrees on the transmission-line axis to excite the optimal polarization with the azimuthal angle of 37.3 degrees. We communicated with e-mails together with to discuss how to install the polarizer and conduct the high-power test in Naka Institute, because we could not join the high-power test in Naka Institute due to the Corona pandemic. In the discussion on the high-power test, electropolishing of mirrors in the FADIS was proposed to avoid the arcing events. After the electropolishing of the mirrors, the high-power test was conducted in Naka Institute.

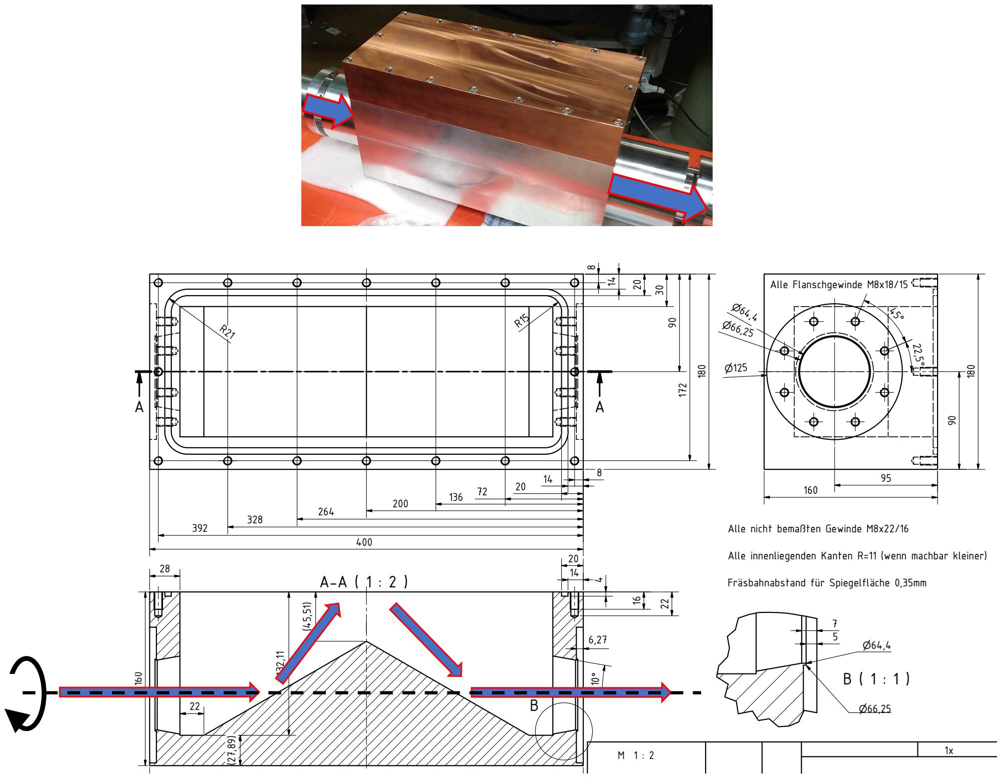

Fig.1: Photo and Drawing of universal polarizer developed at University of Stuttgart.

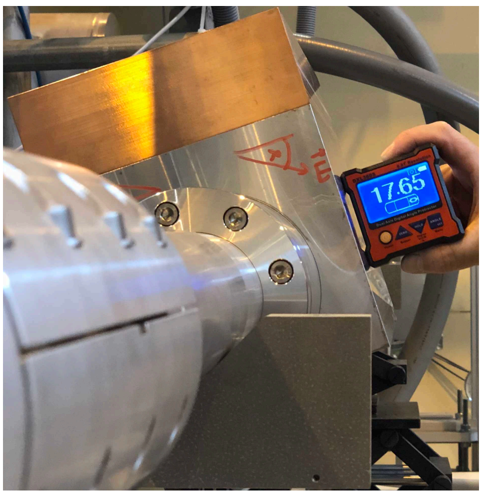

Fig.2: Setup of the universal polarizer in the transmission line. The polarizer is set with an angle of 17.65 degrees on the transmission-line axis to excite the optimal polarization.

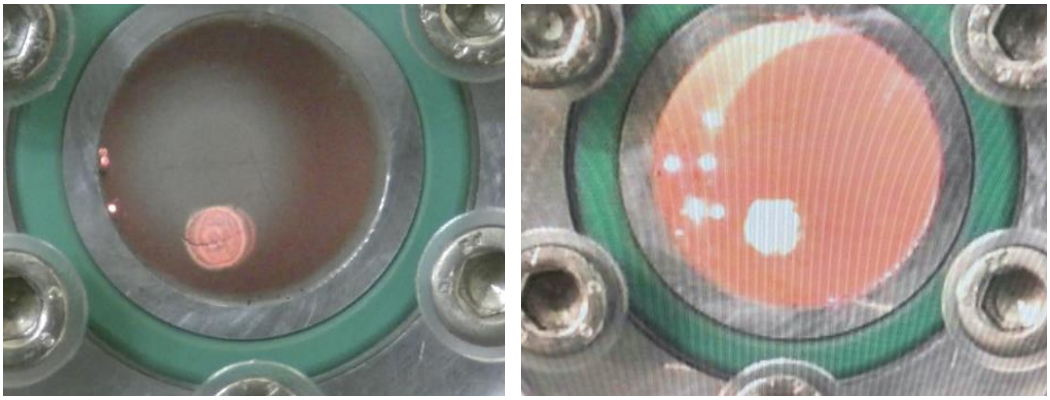

Fig.3: Left side is arc light with power of 341 kW in 2020. Right side is arc light in 2019.

The experiments are performed from 7th to 10th September in 2020. Radio Frequency (RF) power injection to FADIS was started with a relatively low power level of 130kW (Gyrotron beam current; I_b~10A). After the ~100kW (I_b ~10A) power test, the power increased up to 341kW (I_b ~30A). The arc light was observed, but the intensity of the arc light apparently deceased, compared with the experimental campaign in 2019 as shown in Fig. 3. After confirming the arc light decreased, a frequency scan was performed in

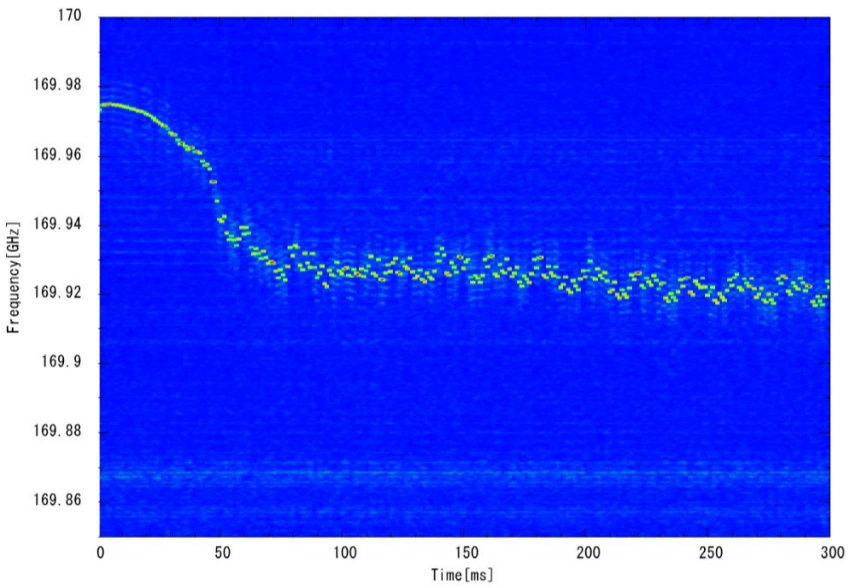

Fig.4: Time dependence of oscillated frequency in 10 A operation of I_b with gyrotron axial magnetic field B_c made at 86.7 A. The frequency becomes stable after 100 ms except for a ~ 5 MHz frequency oscillation.

order to find a resonant frequency of the FADIS. The time dependence of the frequency is shown in Fig. 4. As shown in the figure, the frequency becomes stable after 100 ms except for a ~ 5 MHz frequency oscillation.

By changing the gyrotron oscillation magnetic field B_c slightly, the stable frequency can be changed slightly. The result of the frequency scan by B_c is shown Fig. 4. As shown in Fig. 4, the frequency is changed from 169.87 GHz to 169.99 GHz (~ 120 MHz). The frequency scan was performed with both I_b ~ 10 A (100 kW) operation and I_b ~ 30 A operation (341 kW). Note, the frequency was measured around 250 ms for the I_b ~10 A operation and 200 ms for the I_b ~ 30 A operation, since the pulse width was not extended more than 200 ms for I_b ~ 30 A operation to avoid the risk of the gyrotron damage by RF reflection from the FADIS.

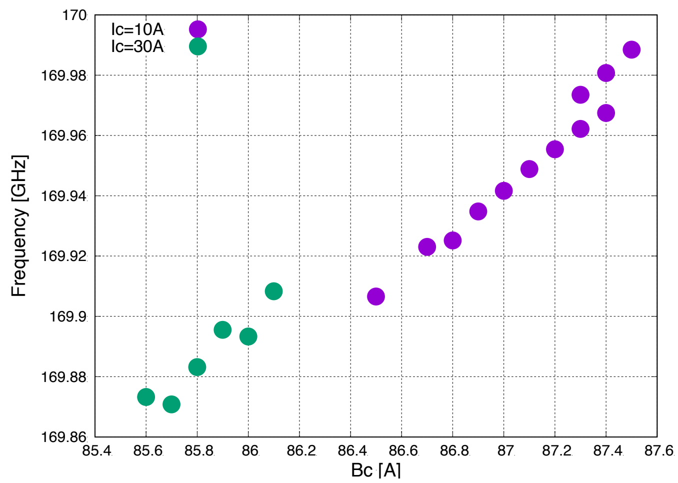

Fig. 5: Measured frequency according to gyrotron magnetic field B_c.

During the frequency scan, coupled power in non-resonant and resonant dummy loads in the FADIS was measured as shown in Fig. 6. The power increased as magnetic field B_c decreased, which is the nature of gyrotrons. The coupling into non-resonant or resonant dummy load should depend on the frequency as switching performance in the FADIS operation. However, as shown in Fig. 6, there was no specific change of power in the non-resonant and resonant dummy loads with any specific frequency. As a conclusion, we could not find any evidence that we operated with resonant frequency in the high-power test. The wider region of the frequency scan was not possible due to the gyrotron condition and power supply condition. Fine tuning of frequency or resonant conditions is needed to confirm the switching FADIS operation in the high-power test.

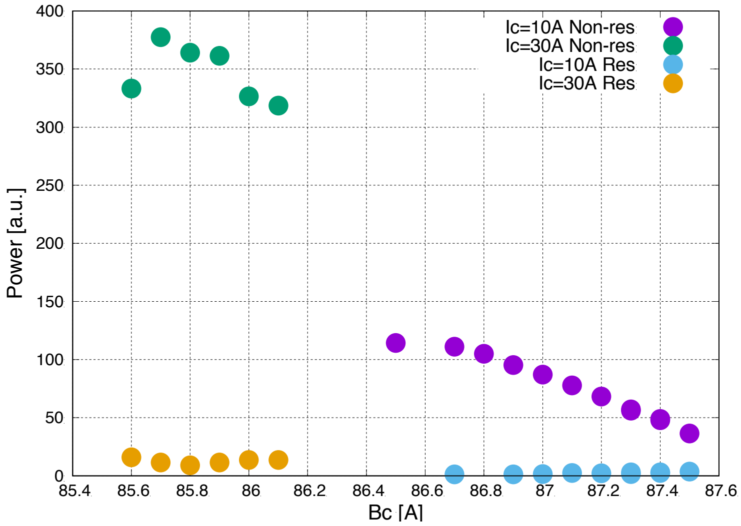

Fig. 6: Measured power according to gyrotron magnetic field B_c, *i.e.* frequency.

国際化推進共同研究概要

No. 6

20NU-4

タ イ ト ル： Development of Core-SOL-Divertor model for simulating tokamak plasmas with impurities

研究代表者： WISITSORASAK Apiwat

所内世話人： 糟谷　直宏

研究概要：
トカマクプラズマにおける不純物輸送について統合的な解析を可能とするために、TASK/TI コードへ SOL ダイバータ領域の効果を組み合わせるのが本研究の課題である。コア輸送モデルと SOL 流体モデルとの結合を図っている。本年度はコロナ禍の影響で応力研出張が取りやめとなった。代わってオンラインでの打ち合わせによりお互いの研究状況を理解し、今後の展望について議論した。

Development of Core-SOL-Divertor model for simulating tokamak plasma with impurities

Apiwat Wisitsorasak, Department of Physics,
King Mongkut's University of Technology Thonburi, Thailand

Impurities in tokamak plasma introduce several deleterious effects on the overall performance of the devices. Large amount of the impurities can dilute the fuel and reduce the rate of the fusion reactions. Furthermore, one of the most immediate effect is the radiated power loss which leads to lower the temperature of the plasma. For examples, impurity ions, such as oxygen and carbon, which are originating from the tokamak vessel, cool the plasma strongly near the edge. However, too much edge cooling destabilizes the plasma and leads to plasma disruption which can severely damage the wall and other structures [1, 2]. On the other hand, metal ions from the plasma-facing components, such as tungsten, can travel farther from the edge and cause significant radiation in in the core. This prevents the plasma to reach high enough temperature for ignition. Hence the concentration of the impurities should be minimized. For a tokamak with the divertor configuration, the impurities shall be pumped away near the divertor, otherwise they will accumulate in the vessel. Besides the downside effects of the impurities, the radiation of the plasma impurities nevertheless has some helpful consequences. Injection of noble gases, such as argon or neon, is intentionally used to increase the radiation in the edge region of the plasma. A well-controlled amount of these seeded impurities helps to disperse the plasma power exhaust over wider surface areas and reduce the temperature in front of the plasma facing components.

This work ultimately aims to understand the transport behavior of the underlying physical mechanisms of the impurities by using a simulation. TASK is a major code in Japan for integrated plasma simulation. The module TI for impurity transport in TASK has been developed by Prof. Emeritus Atsushi Fukuyama in Kyoto University in collaboration with Prof. Naohiro Kasuya in Kyushu University and Theory group in National Institute for Quantum and Radiological Science and Technology (QST). It is based on a fluid description of the plasma and able to compute the profile evolution of the densities and temperatures of all ion stages. The code is a one-dimensional (radial) code in which a method of flux averaging is used. However, the present version of the code only considers the transport in the plasma core in which the magnetic field lines are closed. The transport in the scrape-off layer (SOL), the region outside the plasma core, is not considered yet. Thus, this work will eventually develop the edge transport modeling code and couple it to the impurity transport code in the core by collaboration with RIAM.

The dynamics of the plasma in the edge is complex and involves several nonlinear plasma phenomena [2]. To simulate the plasma in this region, one may reduce the complexity of the problem by only considering the transport along a magnetic field line. The dynamics five-point model is further simplifying the transport and is developed to investigate the response of the plasma in the SOL and divertor regions at five points: the stagnation point (0), upstream throats of divertors (u_A, u_B), and divertor plates (s_A, s_B), see figure 1 [3, 4].

The five-point model simply considers that the plasma particles are transported along an open magnetic flux tube which is divided into four regions (figure 1). By integrating the fluid equations along the magnetic flux tube in each region, one obtains the dynamical equations of the density (n), ion particle flux (Γ), electron (T_e) and ion (T_i) temperatures at each point along the SOL as follows [3, 4].

$$L_{\mathrm{SOL}} dn_0/dt = -\Gamma_{\mathrm{uB}} - \Gamma_{\mathrm{uA}} + S_0 L_{\mathrm{SOL}}, \tag{1}$$

$$L_{\mathrm{div}} dn_{\mathrm{sA,B}}/dt = -\Gamma_{\mathrm{uA,B}} - \Gamma_{\mathrm{sA,B}} + S_{\mathrm{A,B}} L_{\mathrm{SOL}}, \tag{2}$$

$$0.5 m_i \left(l_{a,b} + (R_{\mathrm{A,B}} + 1) L_{\mathrm{div}}\right) d\Gamma_{\mathrm{uA,B}}/dt = n_0 (T_{e0} + T_{i0}) - n_{\mathrm{sA,B}} \left(2T_{\mathrm{esA,B}} + (1+g) T_{\mathrm{isA,B}}\right), \tag{3}$$

$$1.5 L_{\mathrm{SOL}} d(n_0 T_{j0})/dt = -Q_{j\mathrm{uB}} - Q_{j\mathrm{uA}} - \delta_j J (\phi_{\mathrm{uB}} - \phi_{\mathrm{uA}}) + (W_{j0} + W_{j\mathrm{eq}0}) L_{\mathrm{SOL}}, \tag{4}$$

$$1.5L_{\mathrm{div}}d(n_{\mathrm{sA,B}}T_{j\mathrm{sA,B}})/dt = -Q_{j\mathrm{uA,B}} - Q_{j\mathrm{sA,B}} - \delta_j\sigma_{\mathrm{A,B}}J(\phi_{\mathrm{uA,B}} - \phi_{\mathrm{sA,B}}) + (W_{j\mathrm{A,B}} + W_{j\mathrm{eqA,B}})L_{\mathrm{div}}, \tag{5}$$

where the subscript j refers to particle species (i for ions and e for electron) with $\delta_e = 1, \delta_i = 0, \sigma_A = -1$ and $\sigma_B = 1$. S_0 and W_0 are the particle and energy source in the radial direction. The neutral particle source and the ionization energy due to these neutrals are given by $S_{\mathrm{A,B}}$ and $W_{j\mathrm{A,B}}$, respectively. Γ and Q are the particle and heat flux from the core.

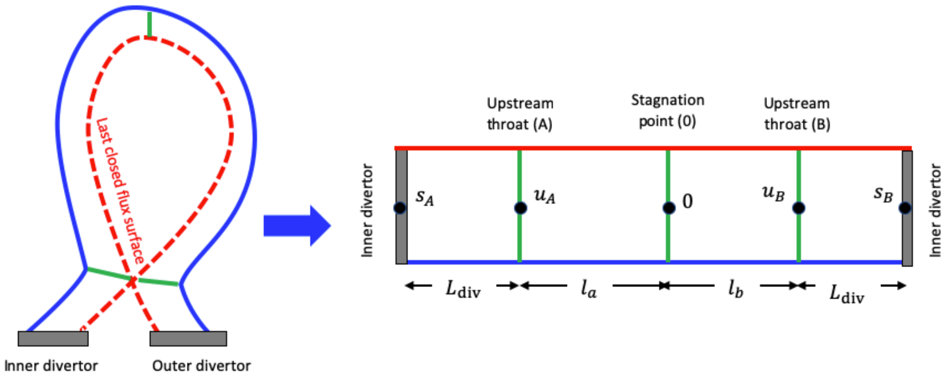

Figure 1: Schematic diagram showing the geometry of the five-point model which considers the transport along the magnetic field.

The dynamic five-point model can be extended to explicitly describe impurity production and transport in the tokamak edge region. This task can be achieved by considering the multifluid equations of impurity species. In the edge, the temperature and density of the plasma are typically less than 200 eV and 10^{21} m^{-3}, respectively [2]. Thus, the charge recombination of the impurity ions may be neglected. Upon neglecting the inertia terms and only considering the transport along the field line, the impurity transport equations of each charge state at the steady state can be written as

$$\frac{\partial n_k v_k}{\partial z} = n_{k-1}\alpha_{k-1} - n_k\alpha_k, \tag{6}$$

$$n_k v_k = -\frac{\tau_k T_i}{m_Z}\frac{\partial n_k}{\partial z} - \frac{ken_k\tau_k}{m_Z}\frac{\partial \phi}{\partial z} + n_k v_i \equiv -D_k\frac{\partial n_k}{\partial z} + w_k n_k, \tag{7}$$

where the subscript k denotes the charge state of impurity ($k = 1,\ldots,Z_{\max}$), m_Z is the impurity mass, v_k is the parallel velocity, $\alpha_k = n_e\langle\sigma v\rangle_k$ is the ionization rate coefficient of impurity species k [5, 6]. These two equations can be solved in two different limits which are based on the relative magnitudes of the ionization and parallel transport contribution for the density of each charge state. For the lower charge state ($k < K < Z_{\max}$), the characteristic time of the ionization process is approximately faster than the parallel transport process. This subsequently leads to the following relation:

$$n_k = \frac{\alpha_{k-1}}{\alpha_k}n_{k-1}. \tag{8}$$

On the opposite case, for the higher charge state ($k \geq K$), the ionization process will occur on the time scale much longer the parallel transport. The continuity equation then becomes

$$n_k v_k = \int_z^{\infty} \alpha_{k-1}n_{k-1}(z)\,\mathrm{d}z, \tag{9}$$

where the integration is performed along the magnetic field line (z direction). Finally, one can explicitly solve equations (6) and (7) for the density of the k^{th} charge state:

$$n_k(z) = e^{P_k(z)}\left(n_{k,\mathrm{sA,B}} + \int_0^z e^{-P_k(z')}\int_{z'}^{\infty}\frac{\alpha_{k-1}}{D_k}n_{k-1}(z'')\ \mathrm{d}z''\ \mathrm{d}z'\right), \tag{10}$$

where $P_k(z)$ is an integrating factor which depends on local velocities and electric potential [5]. In principle, once the background plasma is numerically determined by the basic five-point model, equations (8) and (10) can be directly used to solve the impurity density of each charge at each point along the field line.

Even though the ultimate goal of this work is to develop the calculation method for providing the plasma boundary conditions for self-consistently simulating the impurity transport in the core, such calculation has not been integrated into the transport code yet. The COVID-19 pandemic has large impact on international travel in which several commercial flights have been canceled and many countries have also imposed restrictions for all travelers. These limited visiting RIAM during the last year. However, we have communicated and collaborated the project by using online tools such as *Zoom* and exchanging emails.

In the future work we have planned to implement the calculation of the impurity transport into TASK/TI code which will be a useful and effective method to simulate complex plasmas in both core, SOL, and divertor regions. The simulation result based on this scheme will be eventually evaluated with experimental results from QUEST, PLATO, WEST, and other tokamak, based on availability of the data.

References:

[1] Wesson, J., & Campbell, D. J. (2011). Tokamaks (Vol. 149). Oxford University Press.
[2] Stangeby, P. C. (2000). The plasma boundary of magnetic fusion devices (Vol. 224). Philadelphia, Pennsylvania: Institute of Physics Publication.
[3] Hayashi, N., Takizuka, T., Hatayama, A., & Ogasawara, M. (1998). Onset condition of thermoelectric instability in divertor tokamaks. Nuclear Fusion, 38(11), 1695.
[4] Hayashi, N., Takizuka, T., & Hosokawa, M. (2007). Modeling of dynamic response of SOL-divertor plasmas to an ELM crash. Journal of Nuclear Materials, 363, 1044-1049.
[5] Zagorski, R., & Romanelli, F. (1996). Modelling of impurity production and transport in the scrape-off layer of a high-density limiter tokamak. Nuclear Fusion, 36(7), 853.
[6] Stangeby, P. C., & Elder, J. D. (1995). Impurity retention by divertors: one dimensional models. Nuclear Fusion, 35(11), 1391.

国際化推進共同研究概要

No.7

20NU-5

タイトル：Design of a Permanent CHI injector coil for QUEST

研究代表者：RAMAN Roger

所内世話人：花田　和明

研究概要：
これまでの QUEST の CHI 実験において、バイアス電極とセンタースタック間に入射磁束を形成して CHI 放電を行う場合、その入射領域におけるプラズマ着火が困難であることが示された。また入射領域から磁場形成コイル(PF5-1)の距離が離れているため高いコイル電流を印加する必要があり、その結果電極に接続する 2 本の磁束の脚(footprint)は入射領域を超えた領域まで広がってしまった。2020 年度の実験では CHI 放電のために磁場コイルを増設する案を想定して、その評価のための簡易的な試作コイル(2x12mm の角型カプトン被膜導体を 12 巻したコイル)を真空容器内の電極近傍位置に導入した。更に磁束の形成を入射領域のみに制限するための垂直円筒板をバイアス電極に設置した。放電結果では、入射磁束量を下げた配位において磁束は大きく拡大し、入射電流の駆動が終了した後もドーナッツ形状のプラズマが容器中心部で持続する様子が観測された。この結果は閉磁気面の形成によりプラズマが閉じ込めれていることを示唆している。本実験での結果に基づき次の CHI システムの改造が検討された。まず一つ目に本実験で導入した垂直円筒板をバイアス電極に対して下方向に設置する。これにより垂直円筒板がプラズマ形成に影響を与えることはなくなるので ECH などとの併用が可能になる。二つ目にバイアス電極を現状位置より下げる。これにより適切な入射磁束を PF5-1 のコイルにより形成することが可能になり、コイルを増設する必要がなくなる。現状増設コイルの設置には装置下部の改造が必要であり、PF5-1 コイルを使用する方が好ましい。また電極を下げることでアブソーバー放電の発生が低減すると考えられる。2021 年度に QUEST での高温壁温度制御実験が予定されているため、高温壁の水冷管とバイアス電極の距離を十分に離す必要がある。上記改造は 2021 年度に実施する予定である。CHI 立ち上げによる閉じ込め配位の形成が達成されれば、これと ECH の組み合わせ手法を用いた QUEST での非誘導電流駆動方式による長時間定常運転の進展が期待される。

Design of a Permanent CHI injector coil for QUEST

2 January 2020

R. Raman[1], K. Kuroda[2], K. Hanada[2], M. Ono[3], B.A. Nelson[1], T. Onchi[2], M. Hasegawa[2], J. Rogers[1], M. Nagata[4], O. Mitarai[5], S. Kojima[2], T.R. Jarboe[1]

[1] University of Washington, Seattle, WA, USA

[2] Kyushu University, Kyushu, Japan

[3] Princeton Plasma Physics Laboratory, Princeton, NJ, USA

[4] University of Hyogo, Himeji, Japan

[5] Institute for Advanced Fusion and Plasma Education, Japan

Introduction

Methods for starting a plasma discharge in a spherical tokamak (ST) without reliance of the center solenoid are essential for the validity of the ST concept. These methods could also simplify and reduce the cost of tokamak-based systems and make them more economical by eliminating components that are not needed during steady-state operation. Coaxial Helicity Injection (CHI) for an ST, first developed on HIT-II at the Univ. of Washington and then further developed on NSTX, is the method for which scaling to larger devices such as reactors is well understood. On QUEST, this method would be further developed using the unique all metal capability of QUEST, which is predicted to reduce low-z impurities. In addition, CHI on QUEST will develop a new configuration that is much more suited to an ST-FNSF.

Basic concept for CHI operation on QUEST

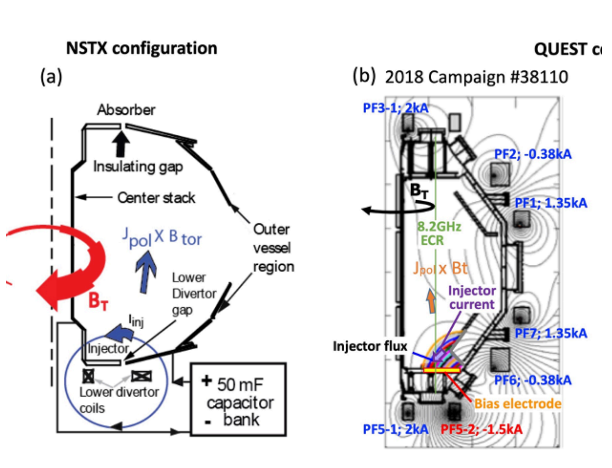

Figure 1: (a) Layout of the transient CHI startup systems in NSTX. The blue circle is the poloidal injector flux produced by the lower divertor coils. This connects the two lower divertor plates, which are insulated. Gas is injected in the region below the divertor gap. On NSTX typically a 5 to 15mF capacitor bank charged up to 1.7kV is used to produce the injector current. (b) Typical vacuum field line configuration for CHI discharge initiation on QUEST.

On HIT-II, and on NSTX, CHI is implemented by driving current along externally produced field lines that connect the inner and outer vacuum vessel components in the presence of externally generated toroidal and poloidal magnetic fields. This is qualitatively shown in Fig. 1 (a). On QUEST, as briefly described in Fig. 1 (b), a toroidal ring electrode is mounted on top of the existing lower divertor plate, and the electrode separated from the divertor plate using a toroidal alumina insulator. Magnetic flux generated by the lower divertor coils connects this electrode plate (the cathode) to the outer vessel (the anode). Gas is injected in the gap between these electrodes and a 20-30mF capacitor bank, charged up to 2kV is discharged across these electrodes to generate the CHI plasma. In experiments conducted during 2019, in which the electrode was biased with respect to the center stack on QUEST it was found that difficulty in forming a suitable injector flux using the existing PF coil set on QUEST resulted in difficulty in good discharge initiation in the region between the electrode and the center stack. Furthermore, because the PF5-1 coil is far away from the injector region, a relatively high coil current was required, and the resulting flux footprint was also widespread and beyond the main injector region.

Permanent Coil and CHI System for QUEST

In support of a permanent coil and CHI system on QUEST, during 2020, experiments were conducted using a temporary in-vessel coil to develop an understanding of the needs for a permamnt coil. Figure 2 shows that concept. This coil allowed improved localization of the injector flux footprint locations (to induce reconnection in this region), This coil is composed of 12 turns wound Kapton insulated copper rectangular conductor. In a second modification, a steel cylindrical electrode was attached to the bias electrode so that the outer leg of the injector flux is limited to the radius of this cylinder.

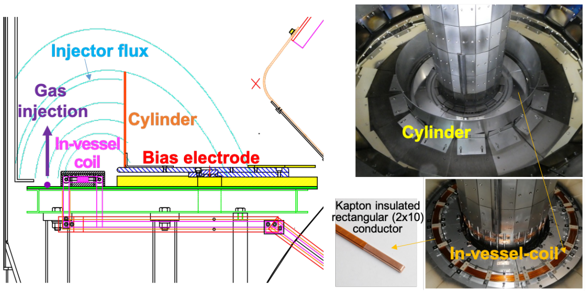

Fig. 2 Modification of t-CHI system. Temporarily installed in-vessel-coil and cylinder attached to the bias electrode.

Fig. 3 shows improved results due to these modifications. Shot #42640 is a discharge when the injector flux magnitude is low, in which about 3 mWb injector flux is formed by 0.5 kA of in-vessel-coil current and 1.0 kA of PF5-1 coil current. After the flux evolution, and after some of this extended flux decays, a detached plasma seen to persists in the camera image even though the injector current has been reduced to zero at $t = 38.75$ms. The camera images are encouraging in that they suggest the formation of closed flux plasma, because a doughnut shaped plasma at the vessel mid-plane, apparently not connected to any other part of the vessel could probably only exist if currents are flowing on closed field lines. Unfortunately, the extensive absorber arching, which in some discharges produces a transient negative current signal, does not permit a Rogowski coil to clearly detect the CHI produced toroidal current.

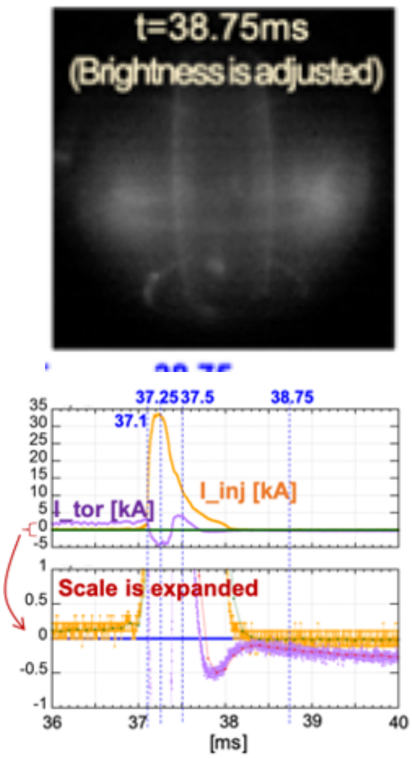

Fig. 3 Improved CHI discharge in shot #42640.

However, these studies provided sufficient information that was used to develop a design for a permanent coil and CHI system for QUEST. The concept is shown in Figure 4. The primary advantages are:

Instead of the 'L' shaped region that sticks into the vessel in the temporary system shown in Fig. 2, the 'L' shaped region is now below the divertor plates, so that it does not protrude into the main plasma region. Thus, this is compatible with normal plasma operations on QUEST. This would support operations of CHI + ECH.

The CHI electrode is lowered. This is important for two reasons. First, it allows the existing PF5-1 coil to be used as the main CHI injector coils as the flux generated by this coil in the injector region is actually now superior to the flux generated by the in-vessel coil shown in Fig. 2. Since it is quite expensive to wind a high current coil without dismantling parts of the components below the QUEST vessel, this would save considerable time and cost as the PF5-1 coil ratings are much more than what is needed for CHI operations.

The second benefit is that the electrode plates are now farther away from the water lines that will feed the hot wall components during QUEST operations during 2021 and beyond. This larger separation distance combined with the fully enclosed CHI region (which will now avoid the CHI gas from leaking down below the divertor plates) should reduce absorber arcing.

These improvements are planned to be implemented during 2021. With these important changes, it is anticipated that routine CHI operations that generate significant amounts of closed flux, can be combined with ECH operations to develops heating and non-inductive current drive capabilities in support of long-pulse steady-state operations on QUEST.

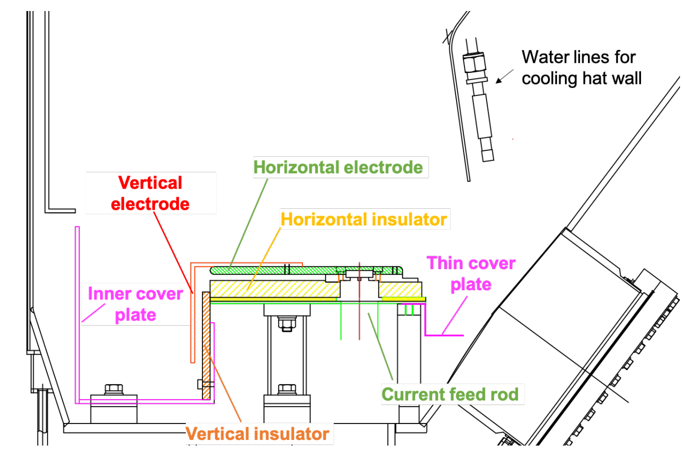

Fig 4: Concept drawing of the new CHI system

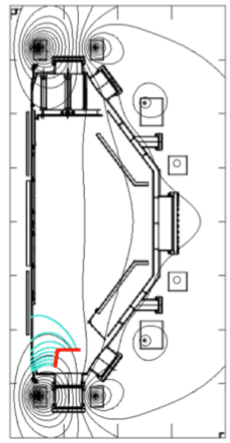

Fig 5: Vacuum flux pattern in the modified CHI region resulting from the use of the PF5-1 coil as the main injector flux coil.

References

[1] Kuroda K et al 2018 Plasma Phys. Contr. Fusion 60 115001.

[2] Raman R et al 2004 Phys. Plasmas 11 2565.

[3] Raman R et al 2011 Phys. Plasmas 18 092504

---

* We acknowledge helpful discussions with Prof. Zushi, Mr. Noda (V-Tech Limited) and Mr. Rogers (Univ. of Washington) and with other members of the QUEST Team.

国際化推進共同研究概要

No.8

20NU-6

タイトル： Joint study of long pulse high beta discharges and related egde turbulence transport in steady state operation (SSO) plasmas on QUEST and EAST

研究代表者： GAO Xiang

所内世話人： 花田　和明

研究概要： 今年度は遠隔でのディスカッションを行った。QUEST で開発された熱負荷計測を EAST の長時間 H-mode プラズマに適用した。IR カメラ計測では表面のわずかな堆積層が発熱することで表面温度が上がるので絶対値の計測が困難であった。一方、冷却水の経路に沿って積算された熱負荷しか測れないため分布の計測が困難である。この両者の欠点を補いあうことで、ダイバータ部の熱負荷分布を絶対値まで含めて行った。この結果は論文として出版された。また当該学生は本研究により中国で学位を取得した。

[1] Y.K. Liu, X, Gao, K. Hanada, Y.W.Yu, H.Q.Liu,…,Y.X.Jie, J.P.Qian et al., Nuclear Fusion **60**(2020) 096019.

（様式 11・拠点）

RESEARCH REPORT

Date: March 5　2021

Visiting scientists: (name) Xiang Gao

(position) Professor

(university / institute) Institute of Plasma Physics, Chinese Academy of Sciences

Host scientist: (name) Kazuaki Hanada

(position) Professor

(university / institute) Kyushu University

Research period: (from) ______________ (to) _____________

Research subject: **Joint study of long pulse high beta discharges and related egde turbulence transport in steady state operation (SSO) plasmas on QUEST and EAST**

Introduction

This year, given the situation of COVID-19, the joint research was done remotely.

Steady state operation (SSO) of tokamak plasma is one of the basic requirements for future fusion reactors. Long pulse high beta operation is one of important missions for ITER. Joint study long pulse high beta discharges in SSO plasma research field on QUEST and EAST is strongly supporting ITER experiment from both experience and theory. In this year, the collaboration research focused on the power balance in SSO high performance discharge, which is benefit for the SSO high beta discharges of EAST and QUEST.

New results in 2020

The Experimental Advanced Superconducting Tokamak (EAST) research program concentrates on demonstrating steady-state high-performance H-mode operations with ITER-like tungsten divertor. Calorimetry was applied to actively water-cool the plasma facing components (PFCs) by increasing the water temperature for power balance investigation. Considering the energy balance of EAST long-pulse high-performance discharges with upper single null (USN) configuration, thus far, approximately 78% of the injected energy could be accounted for.The method of estimation of heat flux on upper tungsten divertor target with a high time- and spatial-resolved infrared camera has been developed, and the sum of its heat load was found to be significantly consistent with that measured through calorimetry. The record longest steady-state H-mode plasma #73 999 was sustained for up to 101.2 s with net injected energy exceeding ~0.25 GJ in the USN configuration. Heat load analysis of this discharge using calorimetric measurement indicates that the modification of heat load distribution was observed and this was induced by a slight change in the magnetic configuration. Not all temperature increments in the five cooling water modules reached the saturated state for the 100 s level discharge, which means that 100 s timescales are insufficient as compared to the thermal transport timescale in the targeted PFCs. The heat load on the tungsten divertor targets is not evenly distributed with the ratio of ~2 in favour of the outer divertor.

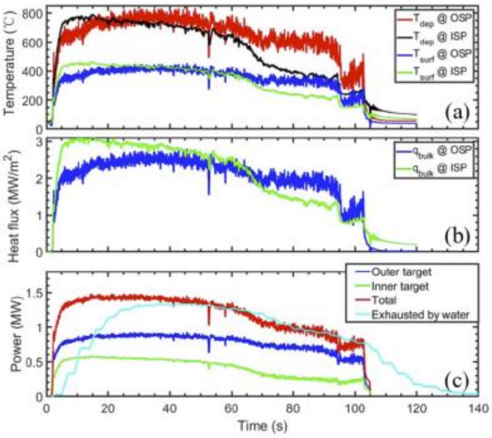

Figure 1 Time evolution of Tdep and Tsurf at the outer and inner strike points (a), of heat flux at the outer and inner strike points (b), of power load (c) for #73 999..

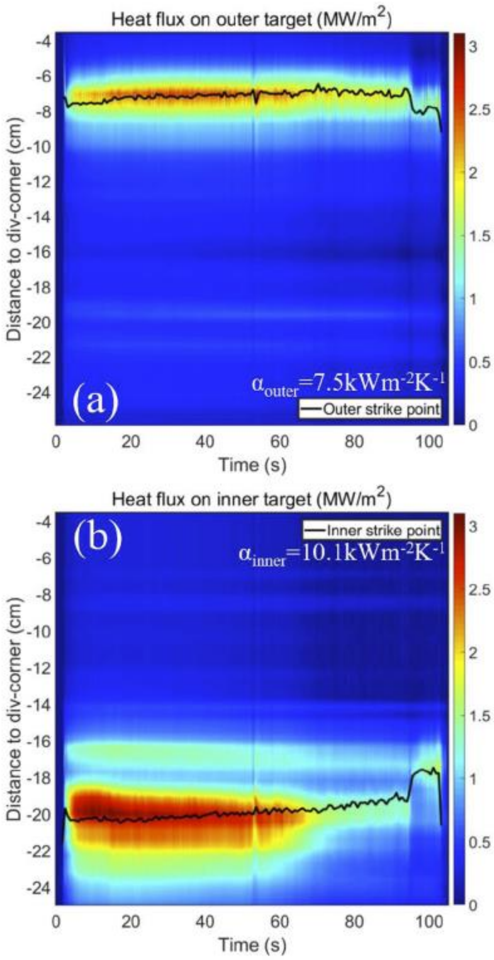

Figure 2 Time evolution of heat flux deposited on outer (a) and inner (b) targets of tungsten divertor for #73 999. The black lines show the distance between strike points and divertor corners..

As shown in Figure 1, the time evolutions of temperature and heat flux at outer and inner strike points for #73 999 are shown in figures 1(a)–(b), heat transmission coefficients for outer and inner targets are 7.5 and 10.1 $kWm^{-2} K^{-1}$, respectively. The maximum of T_{surf} on inner target is slightly above that on outer target, and is not larger than ~450 ◦C. The maximums of heat flux deposited on outer and inner targets are below ~3 MW m^{-2}, which is three tenth of the limit of heat flux on the monoblock for steady state, 10 MW m^{-2}. This means that the divertor monoblock has a capability to withstand 3.3 times of injected power of #73999, which is about 8.3 MW if no mitigation of heat flux on divertor targets can apply. The total power load on divertors decreased by 0.56 MW from 53 s to 103 s due to slight variation of magnetic configuration. The total power on divertor targets is balanced with exhausted power of 1.33 MW by cooling water in steady state. Figure 2 shows the time evolution of heat flux deposited on tungsten divertor targets by above method of fast estimation based on bulk temperature. The measurement denotes that heat deposition on the whole divertor targets was individually observed and the reduced heat flux must be deposited on the other PFCs. The total injected energy and power during the discharge must be equal to that lost on all PFCs. However, the power lost to PFCs also must keep normal distribution. Especially for the achievement of steady-state plasma operation, it is easy for PFCs to cause overheating and production of impurity, ultimately discharge termination if power distribution is extraordinary for a long time. Therefore, the real-time and reliable monitoring of deposited power by diagnostics of surface heat load is crucial in achieving of long-pulse operation.

Discussions

The major motivation of this project is to realize SSO plasma, based on QUEST and EAST device. In 2021, this subtheme will continue pursue in long pulse high beta discharges and related pedestal structure and egde turbulence transport in SSO plasma on QUEST and EAST. Comparsion and combination study of the results will be done on both devices. We will focus on the studying of limit cycle oscillations (LCO) on EAST and QUEST. LCO had been found in many devices during L-H-L transitions. It suggests that to understand the underlying physics mechanism of LCO is important for obtaining steady state high performance plasma. The LCO had been found during L-H transitions on EAST and also had been found during L-LCO-L on QUEST. The combined study will be helpful for understanding the underlying physics and obtaining H mode plasma on QUEST. It is benefit for the long pulse high beta discharges of EAST and QUEST.

Further, I discussed the task of particle orbit calculating arranged by Professor K.Hanada with student Mr. Yunfei Wang, who entered in the Kyushu university for doctor course with Prof. Hanada in last year.

Acknowledgement and comments:

Work supported by the international joint research at the Joint Usage of Research Centers for Applied Mechanics for 2020. I would like to thank our host, Professor K. Hanada, who helps a lot during our remotely research and very appreciate the fruitful discussions and comments. Also RIAM and QUEST staffs are thanked for her kindly helps for this year’s joint research. We hope that the international joint research at the Joint Usage of Research Centers for Applied Mechanics could continue to enhance China-Japan cooperation on fusion plasma research in the future.

My Co-Publications in 2020-2021:

[1] Y.K. Liu, X, Gao, K. Hanada, Y.W.Yu, H.Q.Liu,…,Y.X.Jie, J.P.Qian et al., Nuclear Fusion **60**(2020) 096019.

(Signature)________________________________

(Name in print) Xiang Gao

国際化推進共同研究概要

No.9

20NU-7

タイトル： Soft x-ray spectra in inboard poloidal field null (IPN) configuration and relevant physical research on QUEST

研究代表者： JIE Yinxian

所内世話人： 花田　和明

研究概要： QUESTに設置された２次元のX線カメラに関する共同研究を実施した。対象としては非常に高いX線放射を伴う高βP放電（IPN配位）で、大半径内側にX点が存在する。この配位はTFTRで1991年に報告されており、QUESTでは容易にこの配位が形成できることを活用して高速電子の粒子軌道の観点から議論を行った。高速電子の粒子軌道はEASTの長時間Hモード維持を阻害するhot spot形成に関して重要である。

（様式 11・拠点）

RESEARCH REPORT

Date　March 5　2021

Visiting scientist: (name) Yinxian Jie

(position) Professor

(university / institute) Institute of Plasma Physics,

Chinese Academy of Sciences

Host scientist: (name) K.　Hanada

(position) Professor

(university / institute) Kyushu　University

Research period:　(from) ________ (to) ________

Research subject: Soft x-ray spectra in inboard poloidal field null (IPN) configuration and relevant physical research on QUEST

Due to COVID-19 pandemic，this year we worked remotely.　Soft x-ray spectra system is a very important diagnotic on tokamaks. It is one of the most widely used in measuring the palsma electron tempreture and MHD phenomenons. The whole system needs modification to get more detail date to get the position of IPN and relevant physical research on QUEST.

First, I discussed the mission with Mr. Canbin HUANG. The mission of QUEST is to develop the scientific basis for achieving a steady state condition at sufficiently high beta (~20%), with high confinement and low collisionality. Operating Tokamak at a high poloidal beta value is usually attactive and this makes the spherical tokamak an interesting choice for future reactors.The maximum achievable　βp, however, is limited by a so called equilibrium limit, where an inboard poloidal magnetic field null (IPN) appears at the high field side of the vacuum vessel.Inboard poloidal field null (IPN) configuration in a high Bp discharging was reported first time on TFTR in 1991. In those discharge the evolution of the poloidal field measured at the midplane on the inboard side of the TFTR vacuum vessel was studied.As Ip was ramped down, and Bp increased, the midplane poloidal field decreased and eventually become negative, indicating that the separatrix had crossed the coil position and moved into the vacuum vessel. The separatrixlimited discharge was sustained until the end of the beam heating phase.　In QUEST, such an IPN configuration is easily achieved under a high magnetic mirror ratio and high Bz/Bt values (≈10%) via electron cyclotron (EC) heating and current drive. A soft x-ray spectra system was set up on QUEST and got some primary date.The whole system needs modification to get more detail date to get the position of IPN on QUEST.　Then I discussed the task of particle orbit calculating arranged by Professor K.Hanada with student Mr. Yunfei Wang.

My Co-Publications in 2020-2021:

[1] Y.K. Liu, X, Gao, K. Hanada, Y.W.Yu, H.Q.Liu,…,Y.X.Jie, J.P.Qian et al., Nuclear Fusion **60**(2020) 096019.

(Signature) Y. Jie

(Name in print) Yinxian Jie

国際化推進共同研究概要

No.10

20NU-8

タイトル： Joint study of calorimetric measurement of heat load and power balance estimation in steady state operation (SSO) plasmas on QUEST and EAST

研究代表者： LIU Haiqing

所内世話人： 花田　和明

研究概要： QUEST で開発された冷却水の水温変化で行う熱負荷計測を EAST に適用した。EAST で得られた 100 秒を超える H-mode のプラズマのパワーバランスを計測し、放電後半でダイバータへの熱負荷が減っていることを確認した。この減ったパワーは局所的な熱負荷となって hot spot を形成し、そこからの炭素放出が H mode 放電の終焉に関係していることを見出した。本研究成果は以下の論文の一部となっている。

[1] Y.K. Liu, X, Gao, K. Hanada, Y.W.Yu, H.Q.Liu,…,Y.X.Jie, J.P.Qian et al., Nuclear Fusion **60**(2020) 096019.

（様式 11・拠点）

RESEARCH REPORT

Date: March 5　2021

Visiting scientists: (name) **Haiqing LIU**

(position) **Professor**

(university / institute) **Institute of Plasma Physics,**

Chinese Academy of Sciences

Host scientist: (name) **Kazuaki Hanada**

(position) **Professor**

(university / institute) **Kyushu University**

Research period: (from) ___________ (to) _______

Research subject: Joint study of calorimetric measurement of heat load and power balance estimation in steady state operation (SSO) plasmas on QUEST and EAST

Introduction

This year, given the situation of COVID-19, the joint research was done remotely.

Steady state operation (SSO) of magnetic fusion devices is one of the goals for fusion research. As it is predicted that an enormous heat flux (10MW/m^2) is coming to the diverter (vertical heat target) locally from the plasma in the future fusion reactor, the heat load distrubution (power balance, particle balance) and its control should be investigated to realize future fusion power plants. In last year, EAST energy balance results obtained by calorimetry in long-pulse high-performance discharges provide the foundation for the long-pulse operation of ITER and CFETR. QUEST device, the temperature measurement has been done to measure water cooled movable limiters and other part PFCs. In this year, the collaboration research focused on the power balance investigation in long pulse high performance discharge with ITER-like tungsten divertor on EAST and estimation of fuel particle balance in SSO with hydrogen barrier model on QUEST. From 2020, EAST energy balance results obtained by calorimetry in long-pulse high-performance discharges provide the foundation for the long-pulse operation of ITER and CFETR, and even provide experience for blanket calorimetry to measure plasma reactivity in burning plasma experiment. QUEST device, the temperature measurement has been done to measure water cooled movable limiters and other part PFCs. Although the strong modification of plasma configuration was applied, much of the heat load to the outer vessel was still remained. It means that the heat load is mainly supplied from energetic electrons which are generated by injected RF electric field. The measurement of heat load and researching of power balance in EAST and QUEST will provide crucial support for ITER and CFETR.

Recent results in 2020

During the 2017 campaign, the longest steady-state H-mode plasma was achieved (#73 999 discharge) with the USN divertor configuration in toroidal field direction in which the ion $B \times \nabla B$ drift pointed away from the active X-point. It lasted 101.3 s at a plasma current of 0.4 MA, a central line averaged density of 3×10^{19} m^{-3}, a core electron temperature of 4 keV, and a confinement enhancement factor $H_{98,y2}$ of 1.1. Figure 1 shows the evolution of plasma parameters for the discharge. The central line averaged density < ne > decreased slightly owing to an accidental absence of density feedback controlled by the supersonic molecular beam injection (SMBI) and radiated power signal shows a sharp spike at 53 s. Then it goes down from 53 s to 69 s. The plasma stored energy and radiated power loss increase gradually after 69 s, at which time a number of events occurred.

Figure 2(a) shows the waveforms for the incremental changes in the cooling water temperature in the A, C, E modules.The maximum value of the temperature difference in the A module reached 9.1 ◦C. It should be noted that the water temperature increment of the A module became almost constant after 28 s, then decreased after 55 s. Then, the timegradient of temperature increment in the E module increased as denoted in figure 2(c). This indicates that the heat load distribution on the first wall was significantly changed. The heat load decrement on the A module is 22.6 MJ from 55 s to 105 s, as shown in yellow, if the small injected power reduction in the later stage of this discharge is ignored and the time constant of the exhausted power is the same with the exponential cooling time constant, it is 20.1 MJ after taking injected power reduction into account. The clear reduction of power deposited on the A module was observed after the absence of density feed back control and we investigatied where the power load increased. The visible camera observed several hot spots on the outer plate of the lower dome and the temperature gradient measured by the thermocouples inserted in the guard limiter of 2.45 GHz and 4.6

GHz LHW systems increased, which suggested that a part of power was delivered from the A module PFCs to the E module PFCs and to the guard limiters of the LHW injection systems. The time-integrated heat load exhausted by one part of the E module viewed by visible camera diagnostic, is 30.9 MJ. The ratio of heat load on the E module to total injected energy is about 13.5% when no hot spots appeared on the E module. According to the consideration, the deposited power caused by hot spots can be estimated to be 14.3 MJ, which corresponds to more than the half of the decrement heat load on the A module (20.1 MJ). The power deposited by the hot spots is 0.29 MW, averaged during 50 s, which will make a great threat to the safety of lower divertors with power exhaust capability of lower graphite divertor, 2 MWm^{-2}. The power balance modification may be a reason of the limited plasma pulse duration. If an in-situ monitoring of power balance is available, maintenance of H-mode will be necessary.

A method to quickly estimate the heat flux on tungsten divertor has been developed that analyzes the targets heat flux for #73999. There is a good agreement between heat load measured by the infrared camera and that calculated by calorimetry,and the target power load is not even for this discharge.The detailed understanding of power load in-out asymmetry for long pulse discharges might be an interesting topic, and more work would be needed to know the power loss share of each loss channel.

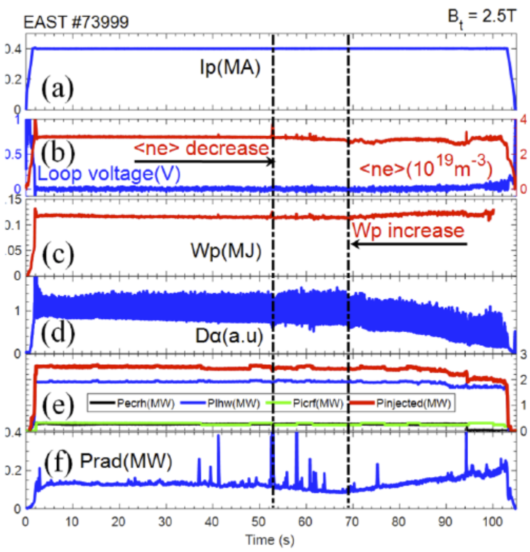

Figure 1 Time evolution of the (a) plasma current Ip, (b) loop voltage and central line averaged density < ne >, (c) plasma stored energy Wp, (d) intensity of the Dα emissions, (e) RF heating power (Pecrh, Plhw, Picrf) and total auxiliary heating power Pinjected, and (f) the radiated power loss Prad.

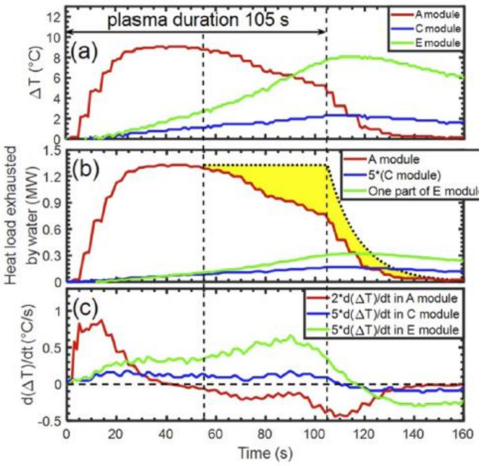

Figure 2 (a) Time evolution of cooling water temperature increment in the A, C, E modules. (b) Time evolution of heat load exhausted by cooling water in the A, C, E modules. (c) Time gradient of water temperature of the A, C and E modules (red line, blue line, and green line, respectively). In this campaign, measurement of heat load on the D module was not available for thelong-pulse (>20 s) discharge period owing to the damages to the temperature sensor on the D module. The B module was also inadequate for monitoring the exhausted heat load for this target campaign.

Discussions

In 2020, we recommended a new student, Mr. Yunfei Wang, to enter in doctor course in Kyushu university and continue to study the power balance (particle balance) estimation and energetic electrons loss in steady state operation (SSO) plasmas on QUEST and EAST. I discussed the task of particle orbit calculating arranged by Professor K.Hanada with student Mr. Yunfei Wang during his interview.

Energetic electrons are the main source of heat load which are generated by injected RF electric field. ECW (Electron cyclotron Wave) is the main source of energetic electrons on QUEST. LHW (Lower Hybrid Wave) is an efficient way to heating and drive the plasma current, and is the main source of energetic electrons on EAST. A significant fraction of LHW power applied to EAST can be lost to the scrape-off layer (SOL) and deposited in hot spots on the divertor rather than in the core plasma. This topic has been researched on many devices such as JET and Tore-Supra. The result show that the LHW power flows to these hot spots along magnetic field lines passing through the SOL in front of the antenna, implying that the LHW power couples across the entire width of the SOL rather than mostly at the antenna face. The energetic electrons tracing code combined with the EFIT equilibrium code is a good simulation framework for the research both on QUEST and EAST. Electron orbit mapping provided by the code combination can be used to explain the experiment observations. This is a very interesting issue for the coming year's joint research.

Acknowledgement and comments:

Work supported by the international joint research at the Joint Usage of Research Centers for Applied Mechanics for 2020. I would like to thank our host, Professor K. Hanada, who helps a lot during our remotely research and very appreciate the fruitful discussions and comments. Also RIAM and QUEST staffs are thanked for her kindly helps for this year's joint research. We hope that the international joint research at the Joint Usage of Research Centers for Applied Mechanics could continue to enhance China-Japan cooperation on fusion plasma research in the future.

My Co-Publications in 2020-2021:

[1] Y.K. Liu, X, Gao, K. Hanada, Y.W.Yu, H.Q.Liu,…,Y.X.Jie, J.P.Qian et al., Nuclear Fusion **60**(2020) 096019.

(Signature)____

(Name in print) Haiqing Liu ____________________________

国際化推進共同研究概要

No.11

20NU-9

タイトル： Improved EFIT code of the plasma equilibrium reconstruction for physical study on QUEST

研究代表者： QIAN Jinping

所内世話人： 花田　和明

研究概要： QUEST 用に導入された EFIT を用いた共同研究を実施した。EAST のダイバータ部の磁気面を詳細に解析することで、ダイバータ部の熱負荷分布の同定に貢献した。また、QUEST で行われた 28GHz の ECCD 実験で、電流が立ち上がっていく過程での磁気面再構成を行い、βP 値からプラズマ圧力を導出し、結果として高速電子の持つ圧力と RF 駆動電流から高速電子の密度と温度を算出した。この結果からプラズマ立ち上げの過程が明確になった。今研究は論文投稿を予定するとともに、QUEST の博士後期課程学生の学位論文に貢献した。

（様式 11・拠点）

RESEARCH REPORT

Date March 5 2021

Visiting scientist: (name) Jinping Qian

(position) Professor

(university / institute) Institute of Plasma Physics,

Chinese Academy of Sciences

Host scientist: (name) K. Hanada

(position) Professor

(university / institute) Kyushu University

Research period: (from) ________ (to) ________

Research subject: **Develop and improve EFIT code of the plasma equilibrium reconstruction for SSO operation and advanced physical study on QUEST**

Due to COVID-19 pandemic，this year we worked remotely. As a start, I help one student familiar with QUEST device and teach him how to run EFIT, which includes checking the connection of PF coils & power supply, update EFIT and EFUND, benchmarking all QUEST FLUX data. We discussed how to optimize the fitting weights of flux loop data to make QUEST EFIT robust. Meanwhile, we are developing how to set up and compile EFIT for different tokamaks. More training for physics understanding of EFIT and how to add more constraints in the equilibrium reconstruction will be ongoing in this year.

In addition, we investigated the q profile optimization in EAST high β_P discharges. Using pure RF heating and current drive, EAST high β_P plasmas have been extended and maintained to long pulse duration with the integrated control. In the experiments, high density operation results in more off-axis lower hybrid current drive (LHCD) that further broadens the current density profile, leading to an improved confinement (H_{98y2}≤1.3)) with the f_{BS} up to 45%. With this ~45% f_{BS}, the NCS q profile was still not observed in EAST high β_P discharges.

The recent integrated modeling prediction we chose high plasma density for enhancing the electron-ion coupling, together with ion heating by Neutral Beam and Ion Cyclotron Resonant Frequency . The efforts of optimization of heating and current drive (H&CD) scheme includes 2.1 MW ECH, 2.0 MW Lower Hybrid Wave (LHW), 2MW co-Ip NB and 2.0 MW ICRF. The existing larger radius ITB and higher β_P allow higher bootstrap current fraction allows the formation of negative centra shear q profile and large radius ITB, where the f_{BS} increases from 45% to ~ 63%. Note that this result submitted to physics of plasma.

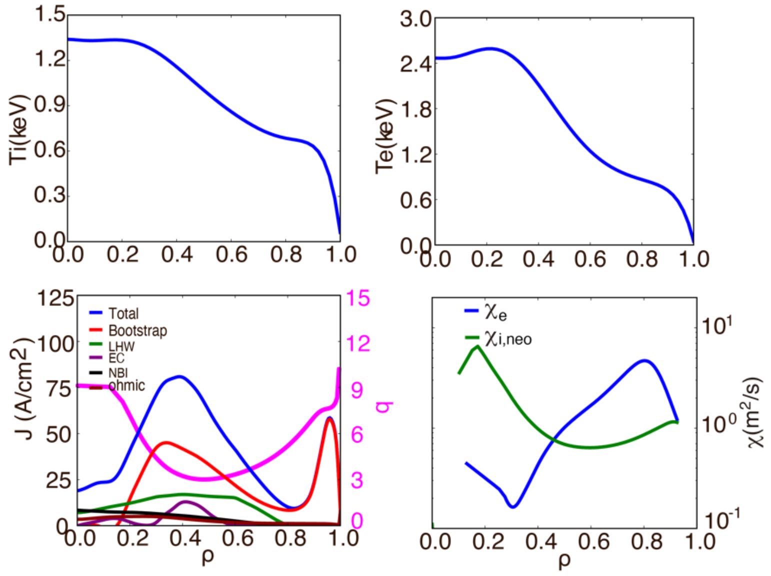

Figure 1 Predicted reversed q profiles with ITB for EAST high betap with optimized heating and current drive scheme

My Co-Publications in 2020-2021:

[1] Y.K. Liu, X, Gao, K. Hanada, Y.W.Yu, H.Q.Liu,…,Y.X.Jie, J.P.Qian et al., Nuclear Fusion **60**(2020) 096019.

(Signature) J. Qian

(Name in print) Jinping Qian

国際化推進共同研究概要

No.12

20NU-10

タ イ ト ル: Development of mm-wave fast switch system to stabilize neoclassical tearing mode in tokamaks

研究代表者： BROEKENS Kristiaan Albert

所内世話人： 出射　浩

研究概要：　本共同研究課題は、研究代表者がコロナ禍の影響で来日できずキャンセルされた。

Development of mm-wave fast switch system to stabilize neoclassical tearing mode in tokamaks

BROEKENS Kristiaan Albert
(TNO Optomechatronics, The Netherlands)

This collaboration program was cancelled because I could not visit Japan due to the corona pandemic.

国際化推進共同研究概要

No.13

20NU-11

タイトル：Identification of chemical compositions of nano-sized oxide particles in high performance ODS ferritic steels for application to accident tolerant fuel cladding

研究代表者：DOU Peng

所内世話人：渡邉　英雄

研究概要：

酸化物分散強化材料は、ナノサイズの酸化物を鉄合金に分散させて分布させることにより、特に高温重照射環境に耐える材料として期待されている。本材料は、特に核融合炉や次世代原子炉の構造材料として期待されているが、微細粒子の照射下での安定性についての情報が不可欠である。共同研究では、核融合炉原型炉に向けて応力研設置のイオン照射装置や収差補正電子顕微鏡にて、ナノサイズ粒子の照射環境下での健全性についての研究を開始している。

Identification of chemical compositions of nano-sized oxide particles in high performance ODS ferritic steels for application to accident tolerant fuel cladding

Peng Dou(Chongqing University)

Super ODS steels have been developed for application to advanced nuclear systems such as fusion DEMO and Gen-IV reactors. Recently, thess materials was considered as a candidate material for so called accident tolerant fuel cladding materials because of their high performance including high-temperature strength, corrosion resistance and radiation tolerance, which are also the critical properties for fusion blanket structural materials.

One of the remained issues for the super ODS steels is the identification of the nano-sized oxide particles dispersed in the matrix of the steels. In this collaborative research, we investigate the chemical compositions of the very fine (less than 5 nm) oxide particles in a ODS steel added with a small amount of zirconium which is considered to play a significant role in the appearance of much higher materials performance. Since the oxide particles are so fine that it is almost impossible to identify them without using the HR-TEM/HAADEF/EDS apparatus in your institute. The utilization of your TEM is essential for an accomplishment of this research.

Nano/meso structure control for high-temperature strengthening of FeCrAl ODS ferritic steel
--Optimization of recrystallization treatment--

I. Project basis and research content

1. Project basis

1.1 Heat resistant advanced ferritic steels

Recent fast economy evolution in China demands highly efficient energy transfer in power generation systems and massive-transportation systems such as nuclear and non-nuclear power reactors, jumbo air crafts and huge tankers and so on. High energy efficiency needs a high-temperature operation of the energy systems [1], which indicates that the structural material should have an excellent high-temperature strength. Heat resistant ferritic steels have been used as structural materials for a variety of energy systems because they have a good cost performance and good enough materials properties at elevated temperatures.

Recently, oxide dispersion strengthened (ODS) ferritic steels have been developed for applications to advanced nuclear power reactors which require a rather high-temperature operation and resultantly better heat resistant steels [2-5]. The ODS advanced ferritic steels are strengthened by dispersion of ultra-fine oxide particles in the matrix of martensite or ferrite phase and possess much higher performance than the previous non-ODS ferritic steels. The amount of Cr is ranging between 9 to 20 wt% which determines the structure of the matrix of the steels. The ODS steels with 9-12wt%Cr have a complex martensitic (9%) and ferritic phase (12%) consisting of dislocations in very high density, dislocation cell structure, packets and lath structure and carbides [2, 3], while the steels with Cr more than 13 wt.% have a simple ferritic phase with some dislocations [4, 5].

The comparison between martensitic steels and ferritic steels reveals that both the steels have both merits and demerits according to the strengthening mechanisms of materials. The complex microstructure of martensite structure is considered to be better for strengthening than the simple microstructure of ferrite structure, because a variety of lattice defects may additively contribute to the strengthening. However, if we consider the thermal stability of the phases, the martensite phase is not stable at temperatures above 850 °C because of the transformation of martensite to austenite, as shown in Fig. 1. Here, the structural material selection for a practical use depends on the operation temperature of the energy system. For example, an electricity power plant can be operated below 700 °C, while the turbine blades of jet engines are imposed an extremely high heat environment above 850 °C, where extremely high thermal stability is inevitable for the materials at temperatures up to 1200 °C, which gives a limit of the application of martensitic steels to the turbine blades. Therefore, generally speaking, the ODS ferritic steels essentially have a wider range of operation temperature of the energy systems because of no transformation of the steel phase in the operation temperature range up to 1500 °C [4, 5].

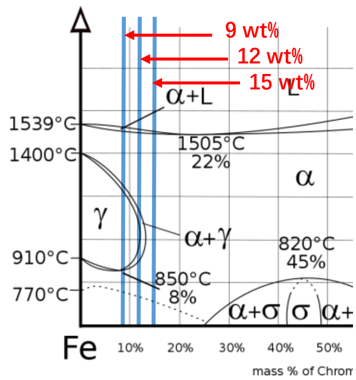

Fig.1 Fe–Cr phase diagram showing α and γ phases depending on the Cr content.

However, it should be noted that a practical use of materials needs shaping and/or welding processes which are often accompanied by recrystallization process. It can be said that recrystallization process is a critical for final material performance because this process is usually given as a final processing of materials production. In ferritic steels, recrystallization causes the grain growth resultantly softening, while offering ductility, which is the first trade-off issue in this research **(Trade-off A)**. For applications to high-temperature materials, too much ductility for shaping is not necessary but rather higher strength is required. But small grain size may sometimes result in grain boundary sliding at elevated temperatures, which is the second trade-off issue in this research **(Trade-off B)**. Therefore, an adequate recrystallization treatment is essential for the practical applications of the ODS ferritic steels as structural materials of advanced nuclear as well as non-nuclear energy systems operated at elevated temperatures.

1.2 Factors controlling high-temperature strengthening

Materials science and engineering has given us several strengthening mechanisms on the bases of dislocation theory [6], which includes solid solution hardening, precipitation hardening, grain boundary hardening, cold work hardening and so on [6]. For ODS ferritic steels, grain boundary strengthening as well as oxide particles dispersion strengthening are the main strengthening mechanisms, while in the ODS martensitic steels, hardening by high density dislocations and carbides are added as the other potential hardeners.

Considering the thermal stability of these three factors, dislocations, grain boundaries and carbides in the ordinary steels (non-ODS steels), dislocations are less stable than the others showing “recovery” process with dislocation climb at temperatures above 450 °C through the vacancy migration [7]. Further rising temperature up to 700 °C causes “recrystallization” process which is accompanied by a remarkable grain boundary migration and coarsening carbides [8]. Above 850 °C, martensite phase transforms to gamma (austenite) phase.

In the ODS ferritic steels, however, the above processes happen at completely different temperature regions because of the presence of oxide particles which hinder the motion of dislocations and grain boundaries [9, 10]. Therefore, the high-temperature strength of the ODS steels are offered by oxide particles in origin, which suppress the recovery and recrystallization, and consequently, the reduction of tensile strength at elevated temperatures is retarded in the ODS steels in comparison to the non-ODS steels [10].

As for the strengthening mechanism at elevated temperature, there are two important microstructures in the ODS ferritic steels, oxide particles and grain boundaries, of which the contribution to the strengthening is represented by Orowan mechanism [11, 12] and Hall-Petch relation [13, 14], as shown in Fig. 2.

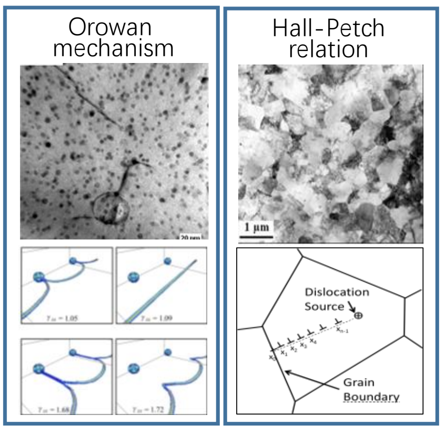

Fig.2 Strengthening mechanism at high temperatures: Orowan mechanism for oxide particles and Hall–Petch relation for grain boundaryies.

Orowan mechanism indicates that finely dispersed particle, namely, finer particles in a higher number density, contribute more to strengthening. Hall-Petch relation also indicates that finer grains with larger grain boundary area contribute more. With increasing processing temperature, however, oxide particles become coarser with lower number density and the grain growth happens to reduce grain boundary area. Thus, the processing temperatures can be as low as possible but a lower processing temperature reduces ductility or fracture toughness of the materials, as mentioned as Trade-off A. This gives us an issue for optimization of processing of temperature and period. As for creep properties, the rapture time is often reduced by reduction of grain size, which is well-known as grain boundary sliding induced creep deformation (Trade-off B).

Now, two questions arise. One is "Which is more contributing to strengthening"; oxide particles or grain boundaries? This issue is rather critical to optimize the recrystallization processing conditions such as temperature, period and the level of cold working. Another is the assessment of an adequate grain size being effective to both high-temperature tensile stress and creep rapture time.

In the most of ODS steels, since the size of oxide particles is in the range from a few nm to 20 nm (nano-scale) and the average grain size is about 1 μm (meso-scale) [15], "**nano/meso structure control"** is necessary to obtain high-temperature strength.

2. Research contents

2.1 Objectives

The objective of this research is to optimize the recrystallization treatment conditions such as temperature, period and cold working level to strengthen ODS steels at elevated temperatures with an enough ductility at RT in terms of nano/meso structure control. For this purpose, the contribution of each factor, oxide particles and grain boundaries, to high-temperature strengthening, both tensile and creep properties, as well as tensile ductility at RT are assessed for an FeCrAl-ODS ferritic steel.

2.2 Key scientific problems

The reason why the contribution assessment for high-temperature strengthening is necessary can be seen in Fig.3, where four cases of nano/meso structure conditions are shown, Case-1: finely dispersed oxide particles and fine grains, Case-2: finely dispersed oxide particles and coarse grains, Case-3: coarsely dispersed oxide particles and fine grains, Case-4: coarsely dispersed oxide particles and coarse grains. We learned from materials science and engineering [11-14] that the Case-1 is the best for strengthening and the worst is the Case-4, while ductility is often the best in the Case-4 and the worst in the Case-1. In order to obtain both the high-temperature strength and ductility, the assessment is necessary to evaluate the contribution of each microstructure, oxide particle dispersion morphologies and grain size to distinguish the total balance in the effectiveness comparing between Case-2 and Case-3.

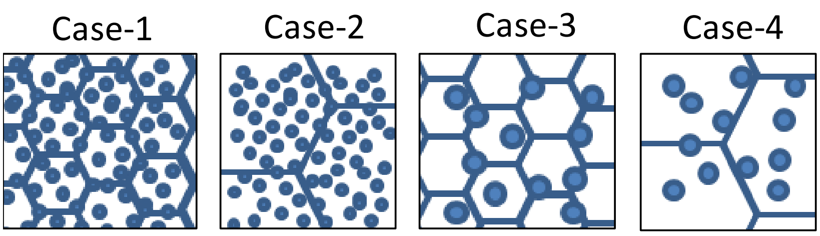

Fig.3 Four cases of nano/meso structure conditions, Case−1: finely dispersed oxide particles and fine grains, Case−2: finely dispersed oxide particles and coarse grains, Case−3: coarsely dispersed oxide particles and fine grains, Case−4: coarsely dispersed oxide particles and coarse grains.

Creep is another important property for high-temperature structural materials. Creep rupture time depends on not only strength but also grain size when the grain size is fine. In contrast to tensile stress at a high strain rate, creep rate sometimes becomes faster with decreasing grain size, which is interpreted in terms of grain boundary sliding at elevated temperatures [15]. Thus, so-called inverse Hall-Petch relation becomes an issue for the steels with fine grain size [16] as mentioned before. Since most of ODS steels has a fine average grain size, it is considered that obtaining both the high-temperature strength in tensile property and long rapture time in creep property is one of the keys of the development of ODS ferritic steels.

Thus, the target of this research is to control both of these nano structure and meso structure to meet the requirements of high-temperature tensile strength, creep rapture time and ductility at RT, namely, the control of both the particles dispersion morphologies such as the size and number density of the oxide particles and grain size of the ODS steel. The difficulty to control nano/meso structures is due to the close relationship between the dispersion morphologies of oxide particles and grain size. It is hard to control simultaneously the oxide particles dispersion morphology and grain size, because changing dispersion morphology of the particles mostly results in the change in the grain size, depending on the heat treatment temperature, period and cold work level [10].

3. Research plan

3.1 Outline of research

A 15wt%Cr-5wt%Al ODS ferritic steel is used for this research. The oxide particle dispersion morphologies and grain size of the steel are altered by changing thermal heat treatment conditions such as temperature and period. Some specimens were cold rolled with different cold work levels before the heat treatment. After the heat treatment, these nano/meso structures are observed by TEM, SEM and XRD before mechanical tests. The tensile properties are measured at 700 °C and RT for the specimens with a variety of oxide particle size and number density as well as with different grain size to investigate the dependence of the yield stress and ductility on the size and number density of oxide particles and grain size. Creep rupture time is measured for specimens with different nano/meso structures. Based on the temperature dependence of Orowan stress (strengthening factor; α) and Hall-Petch relation (constant; k), the conceptual design direction for recrystallization conditions is determined to show which is better between Case-2 and Case-3. Finally, considering the way of solution of Trade-off issues A and B, the recrystallization conditions adequate for high-temperature strengthening with enough ductility at RT are proposed and confirmed by applying the proposed conditions to the practical recrystallization process.

3.2 Technical pathways

The first pathway is the **search for appropriate annealing temperature and period as well as amount of pre-strain** for alteration of oxide particle dispersion morphologies and grain size. Since the thermal stability is different from each other between oxide particles and grain boundaries, there should be an appropriate temperature range for changing effectively each feature of particle and grain boundary. It is considered that the grain size of the ODS steel can be changed by the annealing at a temperature with almost no change in the oxide particle dispersion morphologies. However, it will be very difficult to change the dispersion morphologies of oxide particles without changing grain size, because the dispersion morphology changes require a rather higher annealing temperature at which the grain size is also changed easily [9, 10].

The solution of above issue will be given by computer simulation study, where the effect of dispersion morphology change without grain size change is obtained under the assumption that the Orowan stress is independent of grain size which is considered to be very likely according to the dislocation theory [6].

Next issue is an assessment of an appropriate grain size according to both the tensile property preferring fine grains and creep property preferring coarse grains. It is expected that Case-2 will be the most adequate combination of oxide particle dispersion morphology and grain size according to both tensile and creep properties, which should be proved. It is noted that the Case-2 should be assessed on the availability of tensile ductility at RT.

3.3 Evaluation methods

Nano/meso structures are controlled by changing heat treatment conditions, temperature, period and cold work level, namely, amount of pre-strain. The microstructures are observed by TEM, SEM, XRD as well as APT if necessary, and defined in terms of the size and number density of oxide particles and grain size. The grain size is measured on the surface plane of which the normal is parallel to the extrusion direction so that the grain shape appears to be equiaxed. Tensile tests are carried out at 700 °C and RT, and creep tests at 700 °C. Particle size and number density dependence of tensile properties including yield stress, ultimate stress, uniform elongation and total elongation are investigated. Based on the microstructure observation and tensile test results of the specimens with different nano/meso structures, Orowan stress and Hall-Petch relation is derived to assess the contribution of oxide particles and grain boundaries to the strengthening of the ODS steel. A computer simulation study helps to understand the contribution difference between the oxide particles and grain boundaries. The effect of grain size on the creep rapture time is discussed. Finally, uniform elongation as an indicator of ductility is discussed along with the strength at high-temperatures to show the validity and effectiveness of the nano/meso structure control to optimize recrystallization conditions.

3.4 Feasibility assessment

According to the dislocation theory, the strengthening by oxide particles and grain boundaries are given by Orowan equation and Hall-Petch relation, respectively, as follows:

1) Orowan equation-1

$$\Delta\sigma_{OR1}=\alpha Gb\sqrt{Nd} \qquad (1)$$

where α is the strength factor, G is the shear modulus of the matrix, b is the Burgers vector in the matrix. N and d are the number density and average diameter of the oxide particles, respectively. This formula has been used for obstacles induced by radiation and smaller than a few tens nm in diameter [11].

2) Orowan equation-2

$$\Delta\sigma_{OR2}= 0.1Gb\frac{f^{1/2}}{r}\ln\left(\frac{r}{b}\right) \qquad (2)$$

where G is shera modulus, b is the Burgers vector in the matrix. f and r are the volume fraction and average radius of the oxide particles, respectively. This formula was used for larger obstacles than several 100 nm in diameter [12].

3) Hall-Petch relation

$$\sigma_{YS}=\sigma_0 + k/\sqrt{d} \qquad (3)$$

$$\Delta\sigma_{HP}= k/\sqrt{d} \qquad (4)$$

where σ_{YS} is the yield stress, σ_0 is the frictional stress resisting the glide of dislocation, k is a constant, d is the average grain diameter [13, 14].

In the above equations, α and k may depend on deformation temperature. The temperature dependence of α and k will give an important insight into the optimization of recrystallization conditions, namely, optimized nano/meso structures shown in Fig. 3, where Case-2 or Case-3 will be an appropriate structure recognized as the conceptual design direction. It is expected that the temperature range where k depends significantly on deformation temperature is much lower than the temperature range where α depends on it [9, 10]. This indicates that each of the strengthening mechanism works effectively depending on deformation temperature, resultantly, the nano/meso structure control to obtain high-temperature strength with keeping some ductility is full of feasibility.

4. Features and innovations of the research

The importance of this research is to determine the conceptual design direction of nano/meso structure control to obtain high-temperature strength of ODS ferritic steels which absolutely needs recrystallization process for fabrication of plates, tubes, and etc. The recrystallization of ODS steels are well known to show two steps of recrystallization behavior, primary and secondary recrystallization [17, 18]. The primary recrystallization is an equiaxed grain growth and secondary one is accompanied by a partial abrupt grain growth. Since the dispersion morphology change of oxide particles triggers the grain growth, the change in grain size may be accompanied by the change in oxide particle morphology more or less. It can be said that making clear which factor is the key of strengthening, oxide particle morphology or grain size, is more effective to determine the recrystallization conditions. The solution of this issue provide us a concept of design microstructure to consider the high-temperature strength of structural materials.

An example showing that nano/meso structure control is a sort of innovation is described in Fig. 4, indicating the contribution of strengthening factors at two deformation temperatures for the ODS steels with fine or coarse grains. From the view of engineering aspect, ductility and fracture toughness is required to structural materials at RT, and recrystallization is imposed on them to offer ductility of the materials. The Hall-Petch relation indicates that grain growth reduces the strength at RT as shown in the figure. Since the research on deformation temperature dependence of Hall-Petch relation is so limited for ODS steels, it is unclear how the Hall-Petch relation is effective at 700 °C in this materials. If it is not so effective that coarsening results in no significant softening as shown in the figure, where the difference in $\Delta\sigma_{HP}$ at 700 °C is smaller than at RT, recrystallization conditions, are easily determined to be those keeping oxide particles distribution morphology to be stable while large grain growth is acceptable like Case-2 in Fig. 3. The materials innovation in this research is due to declaration of more effective strengthening factor at high-temperatures, which provide us conceptual design of recrystallization methodology required for ODS advanced ferritic steels for applications to large energy systems.

国際化推進共同研究概要

No. 14

20RE-1

タ イ ト ル：Initialization of collaboration in the theoretical modeling of growth of III-nitride in molecular beam epitaxy

研究代表者： MUZIOL Grzegorz

所内世話人： 寒川　義裕

研究概要：

III 族窒化物を用いた LED（Light Emitting Diode）や LD（Laser Diode）では量子井戸（Quantum Well: QW）と呼ばれる活性層（発光層）が用いられる。量子井戸は電子-正孔対の閉じ込めに使用されるため、通常は数 nm の膜厚に設定されているが、本研究では、～30 nm までの範囲で膜厚を変更し、膜厚と光学特性の相関を調査した。実験結果から、長波長、特に緑色の波長領域デバイスでは、厚膜の QW が有効であることが示された。

Initialization of collaboration in the theoretical modeling of growth of III-nitride in molecular beam epitaxy

Grzegorz Muziol
(Institute of High Pressure Physics,
Polish Academy of Sciences)

The III-nitride semiconductor family is known to have extremely high spontaneous and piezoelectric polarization. In particular, optoelectronic devices can suffer from separation of carriers and low overlap of electron and hole wave functions in the quantum wells (QWs). The overlap strongly drops if the thickness of the QW is increased. However, from the point of view of internal quantum efficiency, it would be beneficial to use wide QWs. Wide QWs should have a lower carrier density and thus reduce the detrimental impact of the non-radiative Auger process, which is known to cause the efficiency "droop" in III-nitride light emitting diodes. In this research, we investigated the relationship between QW thickness and optical properties.

In this report, we discuss that wide InGaN QWs can have highly efficient transitions through the excited states [1] while the transition between ground states is extremely low, as expected due to the built-in field. This highly efficient transition is not present without excitation. It emerges only after screening of the polarization fields.

Photoluminescence (PL) study reveals the complex nature of the transitions in wide QWs. For a low excitation power, the PL intensity drops with the QW width. This could be explained by a decrease of the wave function overlap between carriers. Indeed, this is expected from the band structure of the QWs. However, under a higher excitation power the trend is opposite – the PL intensity increases with the QW width. This is a consequence of a change in the nature of the transitions. In case of the wide QWs, the wave function overlap between carriers is extremely low and they cannot recombine. Thus, under excitation, their density increases up to a point in which the built-in electric field gets screened. Then, even though the overlap between ground states $\langle e1|h1\rangle$ is still small, a new transition path emerges – through excited states. The wave function overlap of the excited states is actually higher than in the case of ground states in a standard thin QW.

A time-resolved photoluminescence study was carried out in order to investigate the dynamics of the carrier recombination. For the thin QWs (thickness of 1 to 5 nm) we observe a staggering, yet expected due to separation of carriers, increase of the decay time. However, when the QW width is further increased the decay time drops significantly. Together with the higher PL intensity, we interpret this as a sign of an increase in the wave function overlap of the wide QWs.

In this research, a comprehensive theoretical and experimental study was performed to show the interplay of transitions between ground and excited states as the thickness of the QW is changed.

Importantly, it was found that the wide QWs can be used in long wavelength devices. Surprisingly, the higher the indium content of the QWs the higher the difference in transition efficiency between ground and excited states. This makes the use of wide QWs advantageous especially in the green spectral regime, in which a drop of efficiency is observed.

An application of the wide QWs to LEDs and LDs was investigated. An enhancement of the optical gain in LDs is measured by means of Hakki-Paoli technique for wide InGaN QWs, resulting in a lower threshold current of the devices [2]. The experimental results will be compared with theoretical predictions.

We discuss an anomalous photocurrent generated in p-i-n diodes with wide QWs [3]. Illumination of the photodiode with light, with photon energy which excites only the QW, results in a forward photocurrent. Under a high-intensity illumination the photocurrent switches to the standard reverse direction. This observation is explained by separation of excited carries by the built-in electric field under the low-intensity illumination and full screening of the built-in field in the high-intensity regime.

References

[1] G. Muziol, H. Turski, M. Siekacz, K. Szkudlarek, L. Janicki, M. Baranowski, S. Zolud, R. Kudrawiec, T. Suski, and C. Skierbiszewski, ACS Photonics 6, 1963 (2019).

[2] G. Muziol, M. Hajdel, M. Siekacz, K. Szkudlarek, S. Stanczyk, H. Turski, and C. Skierbiszewski, Appl. Phys. Express 12, 072003 (2019).

[3] A. Bercha, W. Trzeciakowski, G. Muziol, M. Siekacz, and C. Skierbiszewski, Opt. Express 28, 4717 (2020)

国際化推進共同研究概要

No.15

20RE-2

タイトル： Analysis of Multi-Rotor System Wind Turbines

研究代表者：ISMAIEL Amr Mohamed Metwally

所内世話人： 吉田　茂雄

研究概要：

経済性に優れた将来の超大型の風車のコンセプトとして，1本のタワー上に複数の風車を設置するマルチロータシステム（MRS）が有望視されている．ここで，支持構造の荷重計算と最適化の手法がいまだ確立されていない．本研究では，MRS の連成解析ツールを開発している．今年度は，シングルロータで検証を行い，2～4 ロータの MRS について解析を実施した．検討の結果，タワーの応答において固有振動数が重要であることや，4 ロータ MRS の技術的実現性を明らかにした．

RIAM International Joint Research

General Information

Grant No. 15 20RE-2
Title: Analysis of Multi-Rotor System Wind Turbines
Name of the research representative: Assist. Prof. ISMAIEL, Amr Mohamed Metwally
Affiliation: Future University in Egypt (FUE)

Research subject field: Renewable Energy
Name of RIAM attendant: Prof. Shigeo YOSHIDA

Abstract:

Multi-Rotor System (MRS) wind turbines can be a good alternative to large-scale wind turbines in terms of structural and logistic advantages. An in-house tool was developed in order to analyze the support structure of MRS wind turbines. The tool was verified by comparing the results of a single-rotor wind turbine to an equivalent analysis using the software tool FAST. Then, three different configurations of MRS were studied: including two, three, and four rotors. The tower dynamics were calculated for the main tower in each configuration, as well as the side-booms supporting the two rotors in the twin-rotor configuration. The analyses have shown that the natural frequencies are of big importance and are dominant over the loading regarding the tower dynamics. It has also shown that by comparing the tower dynamics of three and four-rotor configurations, the four-rotor configuration is more technically feasible. In the future, some of the assumptions which were used in developing the code will be removed, in order to get more realistic results and be able to analyze the wind turbine over all ranges of wind speeds.

Research outcomes:

This research is an extension to a PhD thesis made by the research representative. In the PhD phase, aeroelastic analysis has been made for a twin-rotor configuration and compared to a single rotor which has been verified numerically [1].

As an extension, analysis for the side booms holding the rotors on the T-shaped tower has been conducted. Deflections of the side-boom tip in the fore-aft (Out of plane) and in the side-side (In plane) has been calculated for different turbulent wind fields of classes A, B, and C. Figure 1 shows the deflections for wind turbulence class A. Different diameters for the side booms were studied to determine the relation between the boom size and its structural behavior.

It was found that in the in-plane deflections are dominated by the weight of the rotors, regardless of the turbulence of the wind field, the deflection kept almost a constant value. While the out-of-plane deflections were dominated by the random behavior of the aerodynamic loads in the turbulent wind field and induced high, unfavorable vibrations. It was also found that the bending stiffness of the side-booms is directly proportional to its diameter and has a second-order relation with the mean deflection value [2].

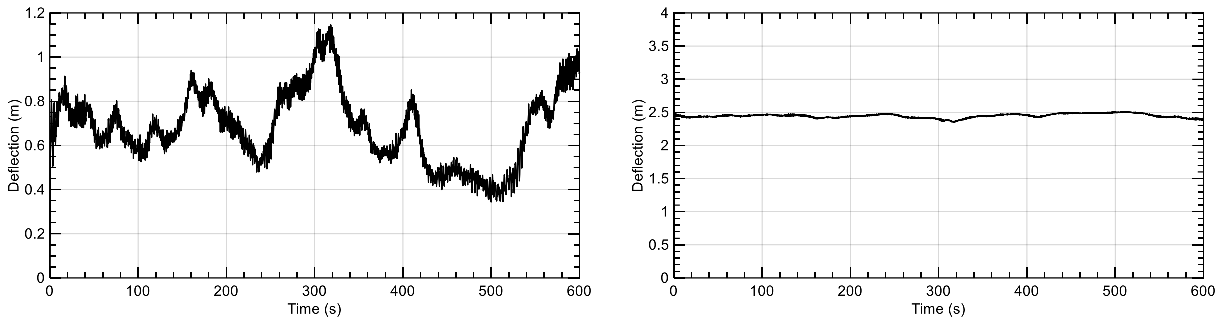

(a) Fore-aft direction (b) Side-side direction
Figure 1. Deflections of the side booms tip for turbulence class A

Furthermore, analyses for three and four rotors have been made for comparison. Tower-top fore-aft and yawing deflections have been calculated for turbulent classes A, B, and C. Tables 1 and 2 show the statistic analysis for the results of the fore-aft deflections for three and four-rotor configurations.

Table 1. Statistical analysis for tower-top deflection in turbulent cases – Three-rotor

Turbulence Class	Mean Value	Standard Deviation	Dominant Frequencies
A	0.343	0.057	0.32 Hz and 2.24 Hz
B	0.343	0.044	0.32 Hz and 2.24 Hz
C	0.344	0.036	0.32 Hz and 2.24 Hz

Table 2. Statistical analysis for tower-top deflection in turbulent cases – Four-rotor

Turbulence Class	Mean Value	Standard Deviation	Dominant Frequencies
A	0.463	0.082	0.32 Hz and 2.22 Hz
B	0.462	0.056	0.32 Hz and 2.22 Hz
C	0.463	0.049	0.32 Hz and 2.22 Hz

As compared to the results of the twin-rotor configuration, both new configurations have shown a significant increase in the tower-top deflection, which is due to the increased height of tower and increased weight and aerodynamic loads. On the other hand, the yawing deflection has decreased, due to the larger and stiffer main tower.

The results of this work have also emphasized that the tower natural frequencies are dominant over the loads in regards of the tower dynamic responses, and hence the importance of the natural frequencies.

Comparing the dynamic responses of the three-rotor and the four-rotor configurations, they both show comparable results. The tower-top deflection of the four-rotor configuration has shown a very slight increase in its value compared to the three-rotor configuration. While keeping in mind that the produced power of the four-rotor configuration is about 30% more, this slight increase in the deflection value can be ignored. Accordingly, the four-rotor configuration can be considered more technically feasible than the three-rotor configuration based only on the tower deflections.

Future Approach

In order to have a better judgment on the feasibility of the three-rotor compared to four-rotor wind turbines, more analyses should be conducted. Pitch control should be added and then compare different wind loads in the high-power region. Power output and cost of energy should also be taken into consideration for comparison.

References

[1] A. Ismaiel and S. Yoshida, "Aeroelastic Analysis of a Co-Planar Twin Rotor Wind Turbine," *Energies,* vol. 12, p. 1881, 2019.

[2] A. Ismaiel and S. Yoshida, "Aeroelastic Analysis for Side-Booms of a Coplanar Twin-Rotor Wind Turbine," *International Journal of Aerospace Engineering,* vol. 13, no. 4, pp. 135-140, 2020.

国際化推進共同研究概要

No.16

20RE-3

タイトル：　Joint study on the next generation of high-reliable and controllable power semiconductor device technologies

研究代表者：　EKKANATH MADATHIL Sankara Narayanan

所内世話人：　齋藤　渉

研究概要：　代表的なパワーデバイスである IGBT において、ターンオフスイッチング時に発生するダイナミックアバランシェは、ターンオフ損失を制限するだけではなく、ノイズ（dV/dt）の制御性や長期信頼性を悪化させる。TCAD シミュレーションと実測結果を元にダイナミックアバランシェの発生原因が電界集中であることを明らかにした。加えて、Clustered IGBT 構造により電界集中を抑制することで、大電流動作においてもダイナミックアバランシェフリーのターンオフスイッチングを実現した。

Joint study on the next generation of high-reliable and controllable power semiconductor device technologies

Sankara Narayanan Ekkanath Madathil, University of Sheffield, Sheffield,

***Abstract*—It is well known that Dynamic Avalanche (DA) phenomenon poses fundamental limits on the power density, turn-off power loss, dV/dt controllability and long-term reliability of MOS-bipolar devices. Therefore, overcoming this phenomenon is essential to improve energy efficiency and ensure their safe operation. In this work, detailed analysis of 1.2 kV MOS-Bipolar devices are undertaken through both calibrated TCAD simulations and experiments to show the fundamental cause of DA and the impact of current density, supply voltage as well as 3D scaling rules on the DA performance. Furthermore, the dynamic avalanche performance of a 1.2 kV NPT Trench Clustered IGBT is evaluated for high current density and low power loss operations. The results indicate that this device configuration is free of DA and can be used for ultra-high current density operation in an energy efficient manner.**

***Index Terms*—IGBT, Clustered IGBT, dynamic avalanche, dV/dt controllability, high current density operation, energy efficiency, power density.**

I. Introduction

TRENCH Insulated Gate Bipolar Transistor (TIGBT) is a key component in various power electronics applications today, such as Electric Vehicle (EV), motor drives and transportations. Recent development of TIGBTs is focused on increasing power densities and switching frequencies with the aims to compete with Wide Band Gap (WBG) power devices and achieve design optimization and cost reduction for power conversion systems [1]. Several novel technologies have been implemented to continuously improve the switching loss (E_{off}) and on-state voltage drop ($V_{ce(sat)}$) trade-off through emitter side Injection Enhancement (IE) effect [2-4]. The improvements in the E_{off}-$V_{ce(sat)}$ trade-off have resulted in not only low loss operations but also increases in current densities and improved cost performance of TIGBT modules. Low E_{off} (high dV/dt) can reduce the system size, because passive component can be shrunk with high frequency operation. However, it is found that high current density and high dV/dt during switching can induce Dynamic Avalanche (DA) within the TIGBTs, which poses fundamental limits on the power density, turn-off power loss, dV/dt controllability as well as long-term reliability of the IGBT modules [5-7]. Overcoming this phenomenon is crucial to increase energy efficiency and ensure safe operation in IGBT applications. Tremendous efforts have been devoted to suppressing DA and eliminating associated reliability concerns. Using p-layers to protect the trench bottoms can suppress but not eliminate DA in the TIGBTs [7], and the holes evacuation is not enhanced. Moreover, an asymmetric gate oxide approach with a designed variable thickness to realize stable long-term operation in TIGBTs and to reduce the switching delay and gate charge without sacrificing the electrical performance has been reported [8, 9]. However, this design cannot suppress DA and no effective designs have been proposed to eliminate DA so far.

In previous work, an in-depth analysis of the TIGBT switching behavior focusing on DA was presented through calibrated 3D TCAD models to show, for the first time, that removal of the high electric field concentration beneath the trench gates was the most important solution to manage the DA in TIGBTs. Moreover, for the first time, a DA free design with high current density operation capability was demonstrated in a Trench Clustered IGBT (TCIGBT), through in both simulations and experiments [10]. In this paper, the operation of this device is studied in detail to explain the reason for its DA free behavior. In addition, the influence of current density and supply voltage on the DA performance of TIGBTs is experimentally investigated. Finally, the impact of 3-D scaling rules of TIGBTs [3, 4] on the DA behavior is evaluated in detail.

II. Dynamic Avalanche in TIGBTs

A. Schematic of DA in TIGBTs

Fig. 1 shows the schematic of DA in the turn-off transient of trench gated IGBTs. During on-state, the carrier density ($p \approx n$) is typically in the range of 10^{16} to 10^{17} cm^{-3} due to conductivity modulation, which is at least two or three orders of magnitude higher than the background doping concentration (N_D). When the device turns off, an increase in the potential drop occurs within a small space charge region of the device with a large

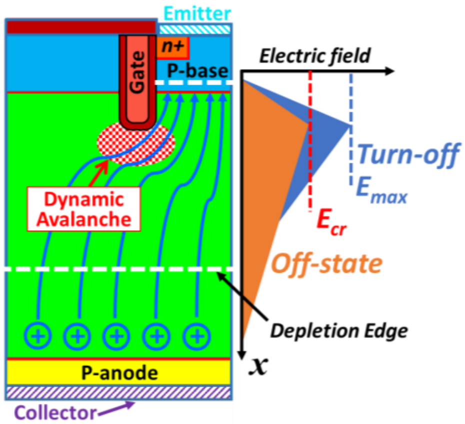

Fig. 1. Schematic of DA during turn-off of TIGBT.

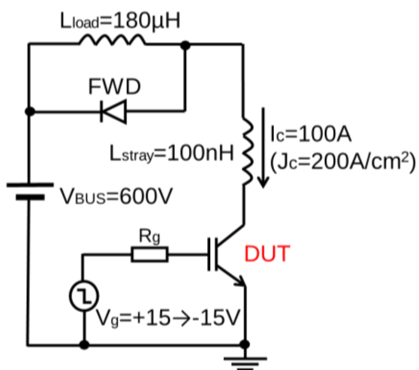

Fig. 2. Test circuit configuration.

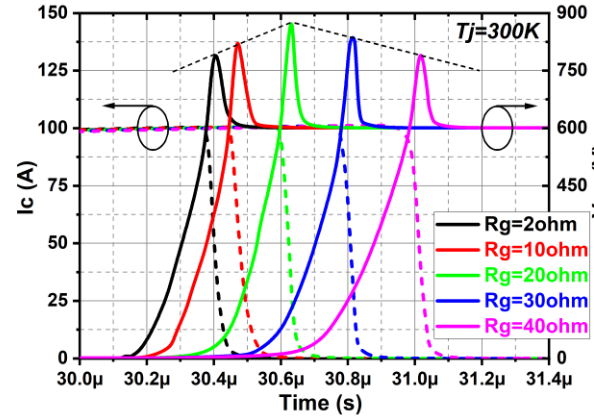

Fig. 3. Switch-off characteristics of TIGBT at various R_g.

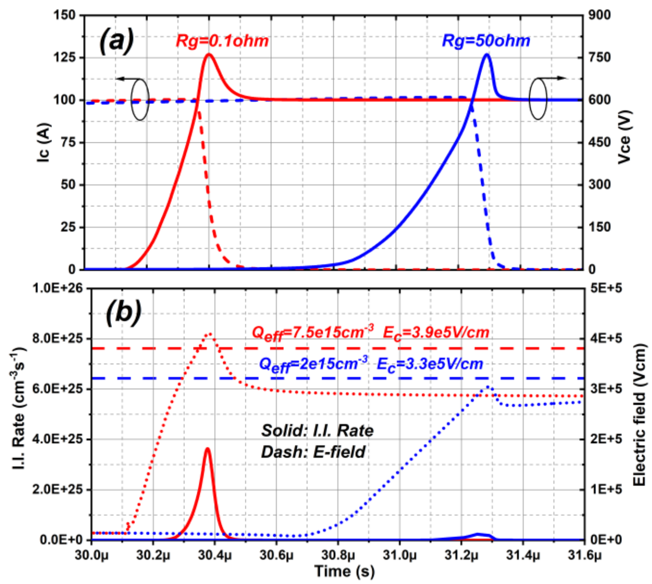

Fig. 4. Comparison of (a) Turn-off curves and (b) I.I. rates and E_{max} of a TIGBT at $R_g = 0.1\ \Omega$ and $R_g = 50\ \Omega$.

part of stored carriers still present. The electric field distribution within the device can be expressed as

$$\frac{dE}{dx} = \frac{q}{\varepsilon}(N_D + p - n). \tag{1}$$

As depicted in Fig. 1, the stored excess holes evacuate through the P-base region, resulting in a peak electric field (E_{max}) which is much higher than the off-state electric field strength. As electric field crowds beneath trench gates, the E_{max} appears at trench bottom rather than at the P-base/N-drift junction. If the resulting E_{max} exceeds the concentration dependent critical electric field (E_{cr}), DA will be triggered even when the collector voltage is well below the off-state breakdown voltage. More excessive carriers are thus generated to result in additional E_{off} and lower dV/dt. Moreover, the excessive carriers generated due to Impact Ionization (I.I.) can have enough energy to be injected into the trench oxide to affect the gate stability and cause associated reliability concerns.

B. Influence of DA on the TIGBTs Electrical Performance

To analyze the DA in silicon TIGBTs, the 3D Sentaurus Device [11] is utilized to simulate the switching behavior, with a circuit configuration for mix-mode simulation as specified in Fig. 2. The dependence of switch-off characteristics of a 1.2 kV TIGBT in Field-Stop (FS) technology on gate resistance (R_g) is shown in Fig. 3. In practice, smaller R_g should induce larger dV/dt during turn-off, the relationship between R_g and dV/dt can be expressed as

$$I_g = \frac{V_{th} + I_c/g_m}{R_g} \tag{2}$$

$$\frac{dV_{CE}}{dt} = \frac{I_g}{C_{GC}} \tag{3}$$

where I_g is the gate current, V_{th} is the threshold voltage, g_m is the transconductance of the MOSFET structure, I_c is the collector current, and C_{GC} is the miller capacitance. However, the DA decreases the dV/dt, which results in decrease in surge voltage even with small R_g conditions, as shown in Fig. 3. This clearly indicates that DA occurs in the cases of $R_g < 20\ \Omega$. Fig. 4(a) compares the turn off curves while Fig. 4(b) compares the maximum electric fields (E_{max}) and maximum I.I. rates in the cases of $R_g = 0.1\ \Omega$ and $R_g = 50\ \Omega$, respectively. In the case of $R_g = 0.1\ \Omega$, due to faster increase in collector voltage (higher dV/dt), the stored excessive holes do not have enough time to be evacuated from the device and flow along the trench bottom, leading to a peak electric field strength which exceeds the critical value, as shown in Fig. 4(b). The critical electric field strength is calculated with (4) and (5),

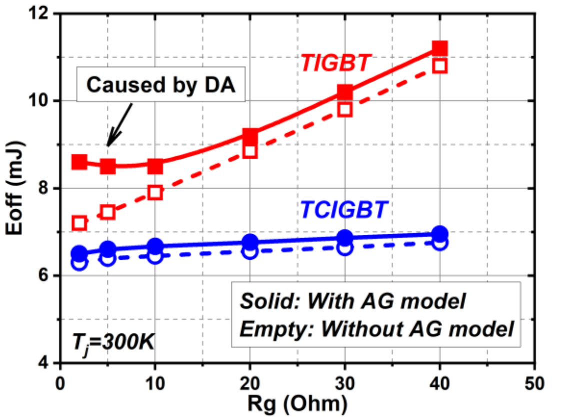

Fig. 5. Dependence of E_{off} on R_g with AG model and without AG model.

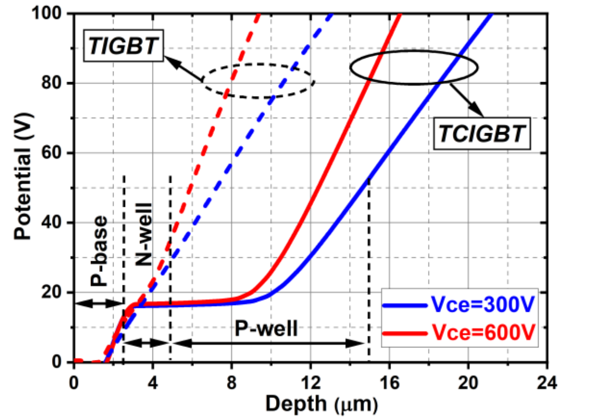

Fig. 7. Simulated potential distributions as a function of collector voltage during turn-off of the TIGBT and TCIGBT.

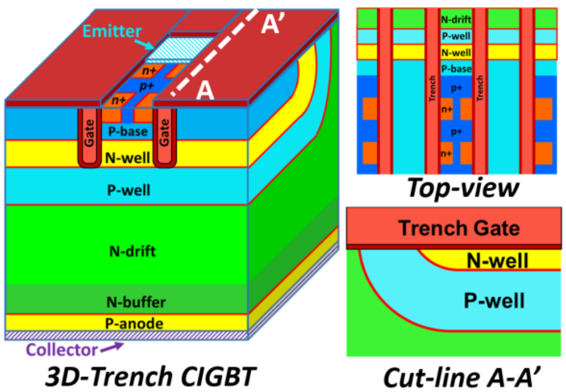

Fig. 6. 3-D cross-sectional view of TCIGBT.

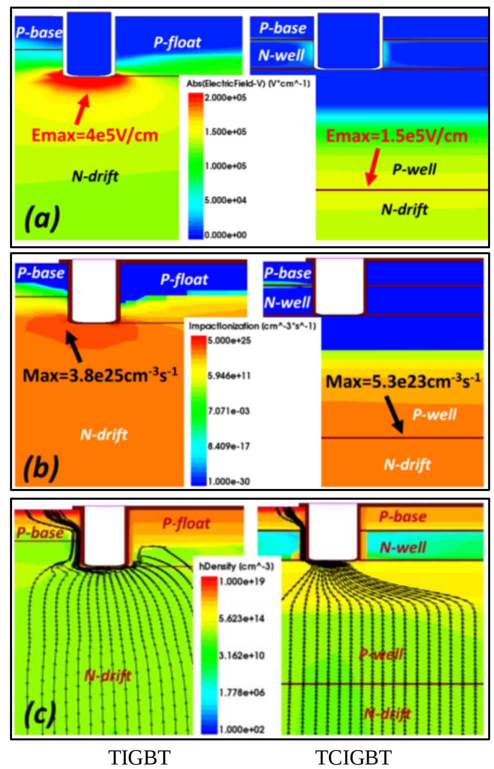

Fig. 8. Comparison of (a) electric field distributions, (b) I.I. rate distributions and (c) hole densities when V_{ce} raises to 600V (R_g = 0.1 Ω).

$$E_{cr}(Silicon) = 4010 \times {Q_{eff}}^{1/8}\ [12] \tag{4}$$

$$Q_{eff} \approx N_D + p \tag{5}$$

where Q_{eff} is the space charge at trench corner. As a result, DA occurs and generates more excessive charge to lower the dV/dt. In contrast, under large R_g conditions, the time to reach supply voltage takes longer, during which most stored charges are removed and DA does not materialize. However, this comes at the expense of increased switching loss and longer turn-off delay time. Moreover, Fig. 5 shows the simulated E_{off} with and without Avalanche Generation (AG) model. The saturation trend of E_{off} with AG model at small R_g conditions is due to DA.

In summary, DA can be triggered by high current density operation, high dV/dt condition, and current filamentation [13]. This phenomenon poses fundamental limits on operating current density, switching frequency, dV/dt controllability, and leads to reliability issues due to hot carrier effect. Therefore, eliminating DA is essential for the development of TIGBTs.

III. Dynamic Avalanche Free Design: TCIGBT

Fig. 6 shows the 3D cross-sectional view of the TCIGBT. The TCIGBT features a MOS-gated thyristor structure, which consists of P-anode, N-drift, P-well and N-well. Its turn-on mechanism has been explained in [14]. In the on-state, the N-well and P-well are conductivity modulated and the device undergoes self-clamping. During turn-off, due to self-clamping, the potential of the N-well layer, which acts as the body of the PMOS is held at a fixed collector potential of less than 20 V, which is the self-clamping voltage of the TCIGBT, as shown in Fig. 7. When the gate voltage decreases below its threshold voltage, because of the increase in body potential, holes are formed along the sidewall of trench gates to connect the P-well layer with P-base region through PMOS action, as shown in Fig. 8(c). Therefore, whether the gate potential goes negative or not during turn-off has no impact on the turn-off behavior. Such a unique design, not available in TIGBTs, provides a direct evacuation path for excess holes to be collected within emitter region. The E_{off} is thus significantly reduced compared to the TIGBT, as shown in Fig. 5. Moreover, as the collector voltage is supported by the P-well/n-drift junction, the trench gates are protected from high electric field so that there is no electric field

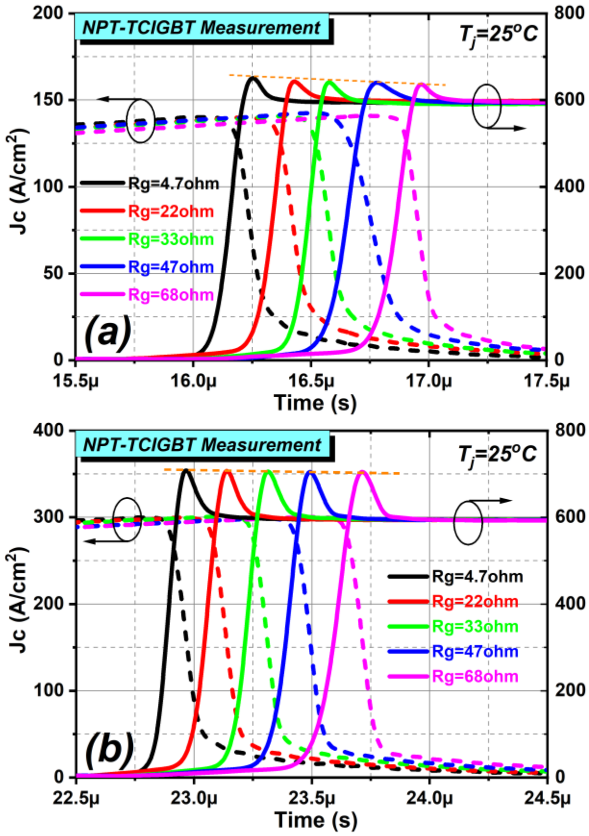

Fig. 9. Experimental switch-off curves of TCIGBT at various R_g at (a) J_c = 140 A/cm^2 and (b) J_c = 300 A/cm^2.

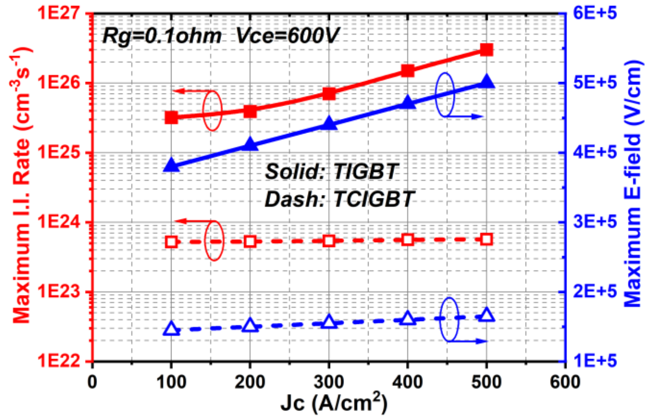

Fig. 10. Impact of current density on E-field and I.I. rate during turn-off.

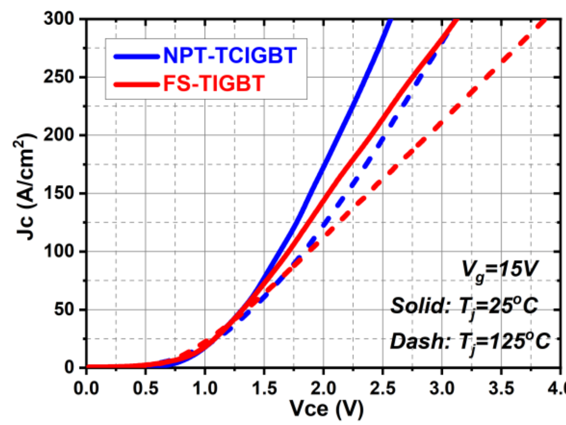

Fig. 11. Experimental results of the I-V curves of TIGBT and TCIGBT.

crowding in TCIGBT, as shown in Fig. 8(a). Thus, it provides a fundamental solution for electric field management at trench regions to prevent occurrence of DA, as shown in Fig. 5.

Figs. 8(a), (b) and (c) show a comparison of the electric field distributions, I.I. rates and hole densities at the time point of V_{ce} increases to 600 V between TIGBT and TCIGBT under R_g = 0.1 Ω and identical $V_{ce(sat)}$ conditions, respectively. As can be seen, the trench gates of TCIGBT are protected from high electric field concentrations during turn-off. In comparison, the TIGBT shows a strong electric field crowding in excess of the E_{cr} under the trench bottom and leads to a high I.I. rate.

Absence of DA in TCIGBT is clear from the experimental results of the switching waveforms of 1.2 kV TCIGBTs measured as a function of R_g, as shown in Figs. 9(a) and (b). These devices show a $V_{ce(sat)}$ of 1.8 V at 140 A/cm^2 at Room Temperature (R.T.) and can support 1.6 kV and are short circuit proof [15]. Although the demonstrated devices were made in Non-Punch-Through (NPT) technology, moving to a thinner FS technology has no impact on the DA, as discussed later. Fig. 9(b) shows that TCIGBT does not show DA even at J_c = 300 A/cm^2. This confirms that TCIGBT can be operated at high current density without DA and associated reliability concerns and with very low power losses.

IV. Impact of Current Density on DA Performance

The continuous increase of power density is crucial for the development of IGBTs to achieve low cost and design optimization for power electronic systems. Higher power density requires higher operating current density as well as low power loss per chip area. However, Fig. 10 shows that DA is significantly enhanced at high current density operations, which poses a limit on the operating current density of TIGBTs. In order to clarify the influence of current density on the DA performance, a 1.2 kV 25 A TIGBT device in FS technology [16] was investigated in detail and compared with the measured results of a 1.2 kV NPT TCIGBT. Fig. 11 shows the comparison of the measured IV characteristics at 25 ºC and 125 ºC. Despite the fact that the FS TIGBT (device thickness = 115 µm) features a much thinner device thickness than the NPT TCIGBT (device thickness = 200 µm), the TCIGBT shows much lower on-state losses in comparison to that of TIGBT at both rated current density (J_c = 140 A/cm^2) and high current densities due to thyristor conduction. The other characteristics of NPT-TCIGBT and FS-TIGBT have been reported in [15]. Fig. 12 shows the measured E_{off} of the TIGBT as a function of R_g at various operating current densities. The E_{off} increases more significantly at small R_g in the case of high current density operations due to enhanced DA. In contrast, the self-clamping feature ensures TCIGBTs to remain DA free performance at high current density operations, as shown in Fig. 13. The E_{off} shows linear decreases as R_g reduces at both R.T. and 125 ºC. Therefore, TCIGBTs are well suited for operating at high current densities without DA effects.

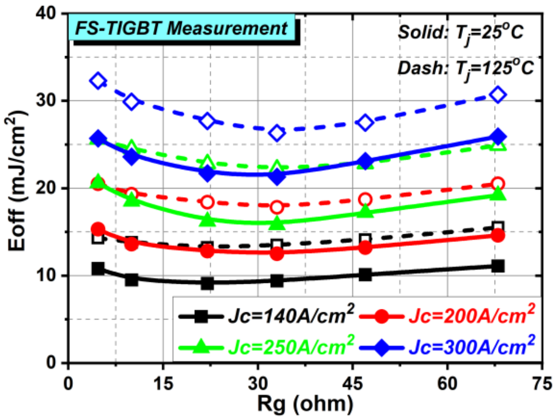

Fig. 12. Impact of current density on the E_{off} of TIGBT.

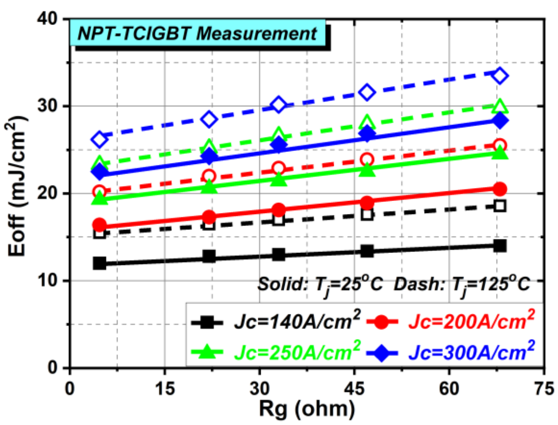

Fig. 13. Impact of current density on the E_{off} of TCIGBT.

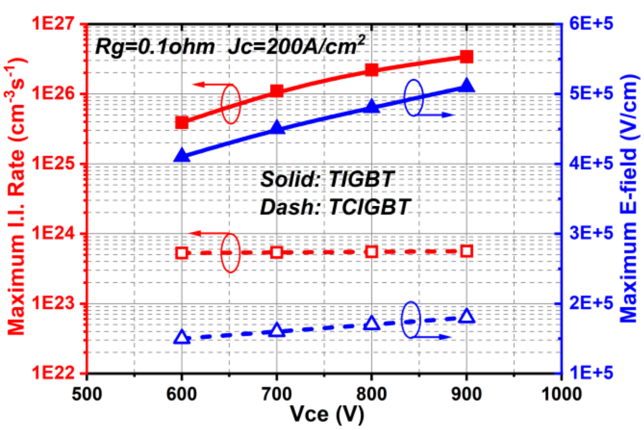

Fig. 14. Impact of supply voltage on E-field and I.I. rate during turn-off.

V. Impact of Supply Voltage on DA Performance

As the collector voltage has a direct impact on the electric field strength within the TIGBT during turn-off, the DA phenomenon is enhanced as supply voltage increases, as shown in Fig. 14. The measured E_{off} of the TIGBT as a function of R_g at various supply voltages is shown in Fig. 15. Note that the minimum E_{off} at V_{ce} = 800 V appears at a larger R_g in comparison to the case of V_{ce} = 600 V, which confirms that higher supply voltage enhances the DA performance of TIGBTs. In contrast, the supply voltage has no impact on the DA free performance of TCIGBT, as shown in Fig. 16.

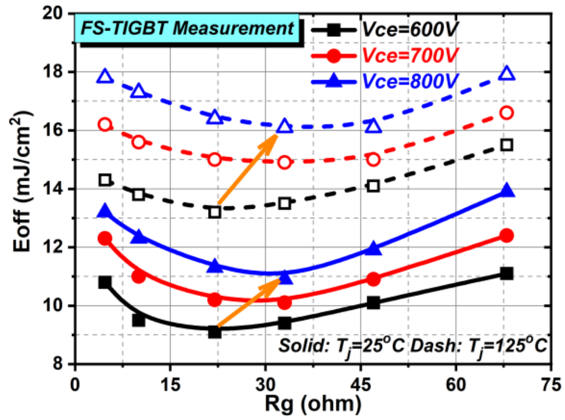

Fig. 15. Impact of supply voltage on the E_{off} of TIGBT.

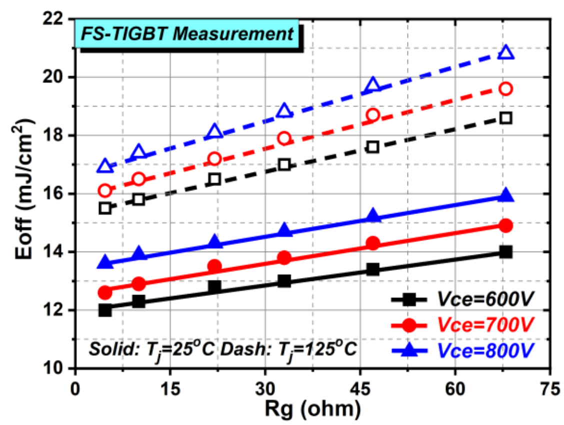

Fig. 16. Impact of supply voltage on the E_{off} of TCIGBT.

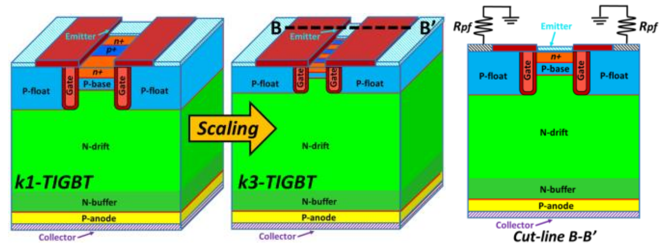

Fig. 17. 3-D scaling rules of TIGBT [4]. Structural parameters are from [4].

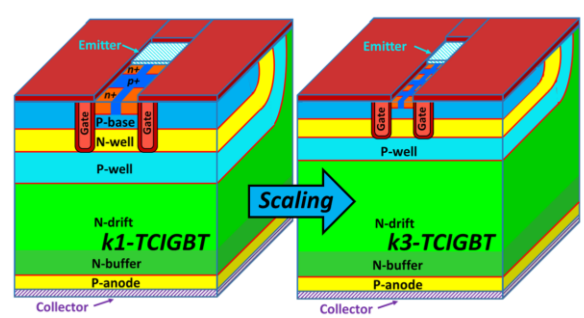

Fig. 18. 3-D scaling rules of TCIGBT. Structural parameters of cathode cells are from [17].

VI. Impact of 3D Scaling Rules on DA Performance

To understand the impact of the 3D scaling rules on the DA performance of the devices, scaled TIGBTs [4] as well as scaled TCIGBTs [17] in FS technologies are considered, as shown in

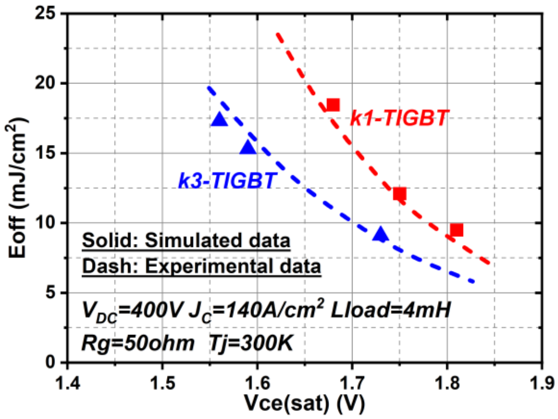

Fig. 19. Calibration of simulated 3-D TIGBT models with experimental data in [4].

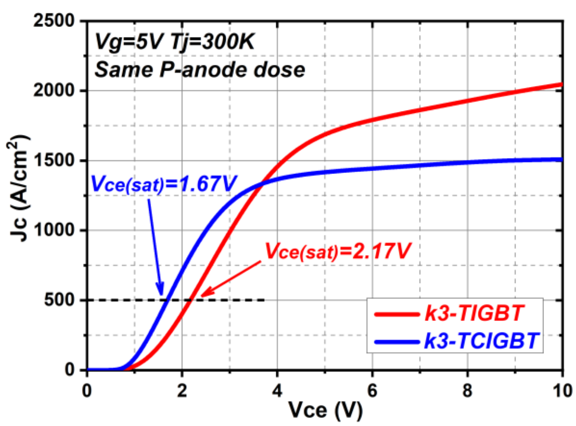

Fig. 20. Comparison of *I-V* curves between *k3*-TIGBT and *k3*-TCIGBT.

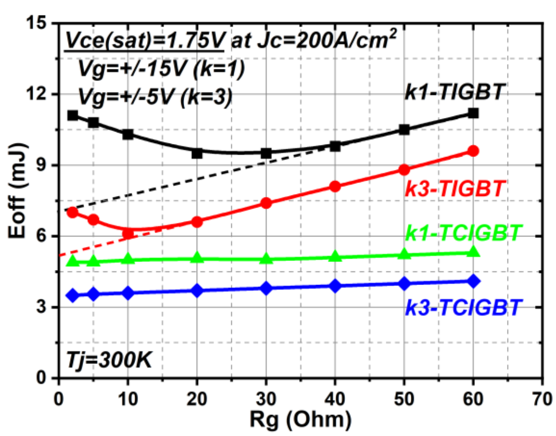

Fig. 21. Impact of E_{off} versus R_g with scaling in TIGBTs and TCIGBTs under same $V_{ce(sat)}$ condition.

Fig. 17 and Fig. 18, respectively. The structures were evaluated through 3D modelling with models calibrated against measured data, as shown in Fig. 19. Note that the device thickness in all structures are identical as in [4] in order to compare the electrical characteristics. Fig. 20 compares the *I-V* curves of *k3*-TIGBT and *k3*-TCIGBT under identical threshold voltage and same P-anode conditions. The *k3*-TCIGBT yields a low $V_{ce(sat)}$ of 1.67 V even at J_c = 500 A/cm^2 at R.T., which is 23 % lower than that of *k3*-TIGBT. Furthermore, the non-saturated *I-V* behavior of narrow mesa TIGBTs is effectively suppressed in

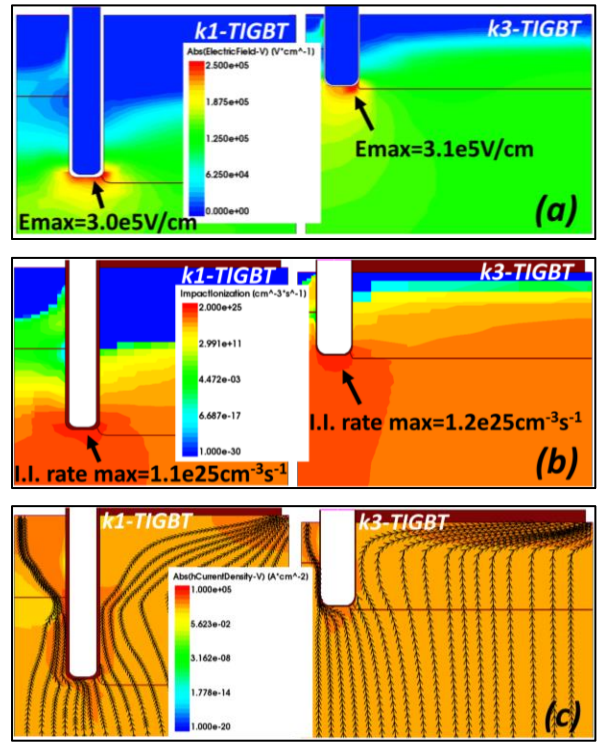

Fig. 22. Comparison of (a) electric field distributions, (b) I.I. rates and (c) hole densities when V_{ce} raises to 600 V (R_g = 20 Ω).

k3-TCIGBT due to enhanced self-clamping feature [17]. The E_{off} dependence on R_g between scaled TIGBTs and TCIGBTs were compared under same $V_{ce(sat)}$ conditions, as shown in Fig. 21, which is achieved by adjusting P-anode concentration. The low switching losses of both devices decrease as a function of scaling rule. Moreover, the lower losses of *k3*-TCIGBT is clear as shown in Fig. 21. In TIGBT, 3D-scaling rule does not suppress DA, because enhanced IE effect influences are stronger than relaxation of electric field concentration as shown in Fig. 22. However, as can be observed from Fig. 21, *k3*-TIGBT does not show any obvious increase in E_{off}, which is due to fast hole evacuation by shallow trench. In any case, care must be taken to address reliability concerns with thinner gate oxides in TIGBTs.

The impact of the on-state carrier profile on DA in *k3*-TIGBT is analyzed by changing the resistance R_{pf} between the p-float region and the emitter, as shown in Fig. 23(a). The carrier concentration at the emitter-side can be increased with high R_{pf} due to the IE effect. The rate of change of voltage (dV/dt) is increased with decrease in R_{pf} (Fig. 23(b)). Both I.I. rates and E_{max} values are enhanced by the positive charge of excess holes around the trench gate bottom (Fig. 23(c)). Most importantly, these results shown in Fig. 23 demonstrate that diversion of holes away from the trench bottom alone does not suppress DA. In Figs. 24(a), (b) and (c) are shown some analysis of DA due to the increase in carrier concentration at the collector-side. Although the turn-off time can be increased by increasing P-anode concentration (Fig. 24(b)), the collector-side carrier concentration has no influence on the DA performance of *k3*-TIGBT (Fig. 24(c)).

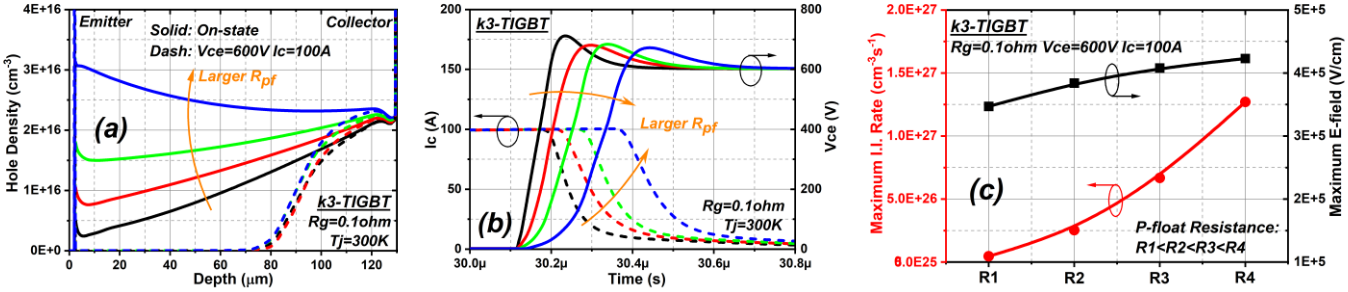

Fig. 23. Influence of R_{pf} on (a) on-state hole density and excess hole density when V_{ce} raises to 600 V, (b) switch-off characteristics, and (c) maximum electric field and maximum I.I. rate when V_{ce} raises to 600 V in the case of *k3*-TIGBT. (V_g = +/- 5 V)

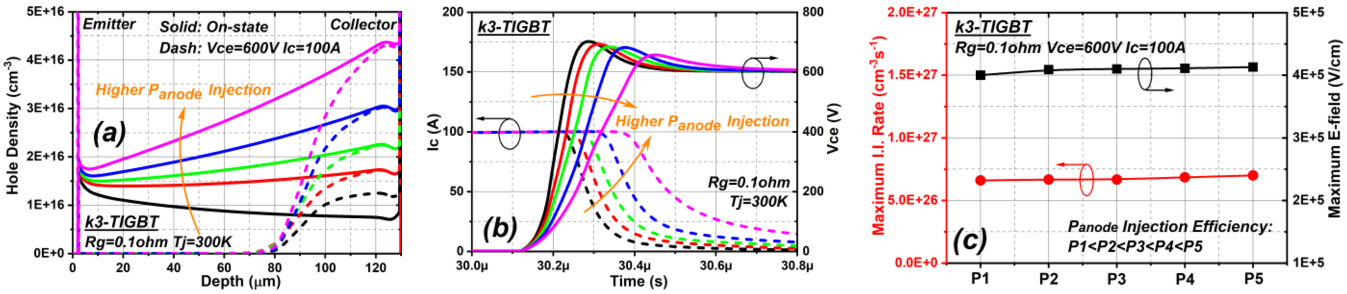

Fig. 24. Influence of anode injection efficiency on (a) on-state hole density and excess hole density when V_{ce} raises to 600 V, (b) switch-off characteristics, and (c) maximum electric field and maximum I.I. rate when V_{ce} raises to 600 V in the case of *k3*-TIGBT. (V_g = +/-5 V)

VII. Conclusions

The 1.2 kV Trench IGBT (TIGBT) switching behavior focusing on the DA was analyzed through calibrated 3D TCAD models. Management of the electric field concentration beneath trench gates is the most critical way to minimize the DA. In addition, a DA free turn-off operation is demonstrated in a Trench Clustered IGBT (TCIGBT), through in both simulations and experiments. As a MOS controlled thyristor device, TCIGBT can be operated with very low power losses at high current densities without DA and associated reliability concerns. This is because of the its PMOS action, which eliminates electric field crowding at trench bottom during turn-off transients. Moreover, experimental results confirm that DA is enhanced at high current densities and high supply voltages and results in significant increase in E_{off} in the TIGBTs. In comparison, TCIGBTs remain DA free performance at high current density operations and high supply voltage conditions. Low turn-off energy loss can be easily achieved by reducing gate resistance. Finally, the impact of device scaling design on the DA has also been analyzed with calibrated models.

References

[1] T. Laska, "Progress in Si IGBT Technology – as an ongoing Competition with WBG Power Devices," in *IEDM Tech. Dig.*, Dec. 2019, pp. 12.2.1-12.2.4, doi: 10.1109/IEDM19573.2019.8993459.

[2] C. Jaeger, A. Philippou, A. V. Ilei, J. G. Laven, and A. Härtl, "A new sub-micron trench cell concept in ultrathin wafer technology for next generation 1200 V IGBTs," in *Proc. 29th Int. Symp. Power Semiconductor Devices and IC's (ISPSD)*, May 2017, pp. 69-72, doi: 10.23919/ISPSD.2017.7988895.

[3] K. Kakushima, T. Hoshii, K. Tsutsui, A. Nakajima, S. Nishizawa, H. Wakabayashi, I. Muneta, K. Sato, T. Matsudai, W. Saito, T. Saraya, K. Itou, M. Fukui, S. Suzuki, M. Kobayashi, T. Takakura, T. Hiramoto, A. Ogura, Y. Numasawa, I. Omura, H. Ohashi, and H. Iwai, "Experimental verification of a 3D scaling principle for low $V_{ce(sat)}$ IGBT," in *IEDM Tech. Dig.*, Dec. 2016, pp..6.1-10.6.4, doi: 10.1109/IEDM.2016.7838390.

[4] T. Saraya, K. Itou, T. Takakura, M. Fukui, S. Suzuki, K. Takeuchi, M. Tsukuda, Y. Numasawa, K. Satoh, T. Matsudai, W. Saito, K. Kakushima, T. Hoshii, K. Furukawa, M. Watanabe, N. Shigyo, K. Tsutsui, H. Iwai, A. Ogura, S. Nishizawa, I. Omura, H. Ohashi, and T. Hiramoto, "Demonstration of 1200V Scaled IGBTs Driven by 5V Gate Voltage with Superiorly Low Switching Loss," in *IEDM Tech. Dig.*, Dec. 2018, pp. 8.4.1-8.4.4, doi: 10.1109/IEDM.2018.8614491.

[5] T. Ogura, H. Ninomiya, K. Sugiyama, and T. Inoue, "Turn-off switching analysis considering dynamic avalanche effect for low turn-off loss high-voltage IGBTs," *IEEE Trans. Electron Devices*, vol. 51, no. 4, pp. 629-635, Apr. 2004, doi: 10.1109/TED.2004.825109.

[6] J. Lutz and R. Baburske, "Dynamic avalanche in bipolar power devices," *Microelectronics Reliability*, vol. 52, no. 3, pp. 475-481, Mar. 2012, doi: 10.1016/j.microrel.2011.10.018.

[7] S. Machida, K. Ito, and Y. Yamashita, "Approaching the limit of switching loss reduction in Si-IGBTs," in *Proc. 26th Int. Symp. Power Semiconductor Devices and IC's (ISPSD)*, Jun. 2014, pp. 107-110, doi: 10.1109/ISPSD.2014.6855987.

[8] C. Sandow, P. Brandt, H. Felsl, F. Niedernostheide, F. Pfirsch, H. Schulze, A. Stegner, F. Umbach, F. Santos, and W. Wagner, "IGBT with superior long-term switching behavior by asymmetric trench oxide," in *Proc. 30th Int. Symp. Power Semiconductor Devices and IC's (ISPSD)*, May 2018, pp. 24-27, doi: 10.1109/ISPSD.2018.8393593.

[9] L. Ngwendson, I. Deviny, C. Zhu, I. Saddiqui, J. Hutchings, C. Kong, Y. Wang, and H. Luo, "New Locos Trench Oxide IGBT Enables 25% Higher Current Density in 4.5kV/1500A Module," in *Proc. 31th Int. Symp. Power Semiconductor Devices and IC's (ISPSD)*, May 2019, pp. 323-326, doi: 10.1109/ISPSD.2019.8757651.

[10] P. Luo, E. M. S. Narayanan, S. Nishizawa, and W. Saito, "Dynamic Avalanche Free Design in 1.2kV Si-IGBTs for Ultra High Current Density Operation," in *IEDM Tech. Dig.*, Dec. 2019, pp. 12.3.1-12.3.4, doi: 10.1109/IEDM19573.2019.8993596.

[11] I. Synopsys, *Sentaurus Device User Guide*: Ver. L-2017. 09.

[12] B. J. Baliga, *Fundamentals of power semiconductor devices*: New York, NY, USA, Springer, 2016.

[13] Y. Shiba, I. Omura, and M. Tsukuda, "IGBT avalanche current filamentaion ratio: Precise simulations on mesh and structure effect," in *Proc. 28th Int. Symp. Power Semiconductor Devices and IC's (ISPSD)*, Jun. 2016, pp. 339-342, doi: 10.1109/ISPSD.2016.7520847.

[14] O. Spulber, M. Sweet, K. Vershinin, C. K. Ngw, L. Ngwendson, J. V. S. C. Bose, M. M. D. Souza, and E. M. S. Narayanan, "A novel trench clustered insulated gate bipolar transistor (TCIGBT)," *IEEE Electron Device Lett.*, vol. 21, no. 12, pp. 613-615, Dec. 2000, doi: 10.1109/55.887483.

[15] H. Y. Long, M. R. Sweet, M. M. D. Souza, and E. M. S. Narayanan, "The next generation 1200V Trench Clustered IGBT technology with improved trade-off relationship," in *Proc. Applied Power Electronics Conference and Exposition (APEC)*, Mar. 2015, pp. 1266-1269, doi: 10.1109/APEC.2015.7104510.

[16] Datasheet: Infineon IGBT, Available: http://pdf.tixer.ru/517408.pdf [Online].

[17] P. Luo, H. Y. Long, M. R. Sweet, M. M. D. Souza, and E. M. S. Narayanan, "Numerical Analysis of 3-D Scaling Rules on a 1.2-kV Trench Clustered IGBT," *IEEE Trans. Electron Devices*, vol. 65, no. 4, pp. 1440-1446, Feb. 2018, doi: 10.1109/TED.2018.2807318.

国際化推進共同研究概要

No.17

20RE-4

タ イ ト ル： Renewable Energy Dynamics

研究代表者： MANICKAM Srinivasan

所内世話人： 柿本　浩一

研究概要： 本研究では、シリコン太陽電池を安価に製造するために必要な結晶育成炉の設計のために、大規模数値解析を行った。その結果、ルツボ底部の温度分布の最適化が非常に重要であることが分かった。特に温度分布制御の時系列変化を最適化することが重要であることが分かった。現在最適化の途中であり、今後も継続的に共同研究を行っていく予定である。

Dislocation Analysis of Si grown by Directional Solidification Method

MANICKAM Srinivasan
SSL, Chennai, India

Abstract:

This paper reports the relationship between oxygen concentration and dislocation multiplication in silicon crystals during directional solidification using numerical analysis. This analysis involved oxygen diffusion from the bulk to dislocation cores during crystal growth and annealing processes in a furnace based on the Alexander–Haasen–Sumino model. The calculated results showed that the dislocation density increased during cooling process, rather than crystal growth, when the effect of oxygen diffusion to dislocation cores was ignored. Meanwhile, the dislocation density increased during both crystal growth and cooling processes when the effect of interstitial oxygen diffusion was considered.

Introduction:

Dislocation is one of the most harmful defects in silicon crystals, causing current leakage in photovoltaic cells and large scale integrated circuits. M'Hamdi et al. reported that the dislocation density increased during the cooling process, rather than during crystal growth. The effect of interstitial oxygen on dislocation multiplication was not discussed. Imai et al. reported that oxygen concentration affected the dislocation velocity as a function of shear stress in silicon crystals. The crack was introduced into silicon crystals grown by the floating zone, Czochralski (CZ)-grown, and magnetic field-applied CZ methods. They also reported the measured dislocation velocity under applied stress at elevated temperature having different oxygen concentrations.

In this study, we focus on the relationship between oxygen concentration and dislocation multiplication in silicon crystals. We studied the effects of interstitial oxygen on the dislocation multiplication in silicon crystals having inhomogeneous distribution of oxygen concentrations during both crystal growth and cooling processes using numerical analysis. We also took into account oxygen diffusion. The model included the effect of the dislocation density which was equivalent to the distance between dislocations when the diffusion of interstitial oxygen atoms was considered.

Calculation method:

We applied the viscoelastic model for stress analysis using a two-dimensional axisymmetric model. A three-dimensional analysis was carried out to calculate the dislocation density in silicon crystals using the numerical method reported elsewhere. We took into account the activated mechanics of slip systems in different growth directions, immobilization of mobile dislocations, and the jog formation between different slip systems. The silicon crystals have 12 slip directions. The resolved shear stress in each slip direction can be calculated by the tensor transformation technique using stress components obtained from a three-dimensional analysis of the stress.

Results:

The result shows that the dislocation density increased during crystal growth and then remained constant at 1300 K in the case without considering the oxygen diffusion, shown by a dashed line, whereas the density became constant at 1500 K in the case with the oxygen diffusion. M'Hamdi reported that the density mainly increased during crystal cooling process, whereas the density increase occurred during both crystal growth and cooling processes by considering oxygen diffusion to dislocation cores. The oxygen concentration in dislocation cores increased remarkably at 1500 K, due to the oxygen diffusion from the bulk to dislocation cores at elevated temperature.

Conclusion:

This paper reports the relationship between oxygen concentration and dislocation multiplication in silicon crystals during a directional solidification method using numerical analysis. The analysis was based on the HAS model, and involved oxygen diffusion from the bulk to dislocation cores during the crystal growth, and the annealing process in a furnace. When the dislocation density was larger than 1.0×10^5 cm^{-2}, interstitial oxygen concentration in bulk decreased, due to the diffusion process of interstitial oxygen atoms between dislocations.

国際化推進共同研究概要

No.18
20RE-5

タ イ ト ル: Predictions of Viscous Damping of Floating Structure Based on Computational Fluid Dynamics Method

研究代表者: GAO, JUNLIANG

所内世話人: 劉 盈溢

研究概要: Floating wind turbines (FWT) introduce new challenges in evaluating the dynamic motion and the power generation performance. At present, there are three branches of methods to predict the performance of a floating wind turbine, i.e., physical experiment, numerical evaluation based on potential flow theory, and numerical simulation based on computational fluid dynamics. Physical experiments are often limited by the experimental site and the huge cost. Although the evaluation efficiency of the existing model (such as the FAST program, etc.) is very high, it often requires an artificial damping term for the Morison Model, which needs to be determined by physical experiments. Instead, we are seeking for a substitution method based on computational fluid dynamics (CFD) solvers, to do an equivalent work that an experiment does (e.g., evaluate the viscous damping in all six DOFs of FWT motions from the free decay test performed by a CFD method), hence to substantially reduce the cost required by a model test or on-site experiment.

Introduction

Offshore wind turbine offers a promising solution to harnessing abundant wind resources. With the development of technology, the offshore wind turbine industry is gradually moving from shallow water to intermediate water and deepwater. As one of the three mainstream concepts of the floating foundation to keep stability, the semi-submersible type has a smaller surge response than the TLP (Tension Leg Platform) type and a smaller pitch response than the spar type (Goupee et al., 2014). The installation cost of the mooring system of a semi-submersible foundation is also relatively lower than the other types of floating foundations (Liu et al., 2016). Researches have been undertaken on various aspects of the semi-submersible concept, involving model testing (Kim et al., 2017), numerical modeling and conceptual study (Liu et al., 2018).

At present, there are three branches of methods to predict the performance of a floating wind turbine (FWT), i.e., physical experiment, numerical evaluation based on potential flow theory, and numerical simulation based on computational fluid dynamics. Physical experiments are often limited by the experimental site and the huge cost. Although the evaluation efficiency of the existing model (FAST, etc.) is very high, it often requires the artificial damping term for the Morison Model, which needs to be determined by physical experiments. In the current study, to substantially reduce the cost required by a model test or on-site experiment, an open-sourced CFD software OpenFOAM is adopted to do an equivalent work that an experiment does.

Methodology

Governing equations

The multiphase flow solvers, *waveDyMFoam*, use the Navier–Stokes equations to describe the motion of the fluid continuum. These equations can be expressed as:

$$\frac{\partial \rho}{\partial t} + \nabla \cdot (\rho \vec{U}) = 0 \tag{1}$$

$$\frac{\partial \rho \vec{U}}{\partial t} + \nabla \cdot (\rho \vec{U}\vec{U}) - \nabla \cdot (\mu \nabla \vec{U}) - \rho \vec{g} = -\nabla p - \vec{f_\sigma} \tag{2}$$

where $\vec{U}$ is the flow velocity vector, ρ is the density of the fluid, μ is the dynamic viscosity, $\vec{g}$ is the acceleration due to gravity, p is the pressure of the fluid, and $\vec{f_\sigma}$ is the surface tension.

To track the shape and position of the free surface, the volume of fluid (VOF) method has been employed in OpenFOAM. In grid cells, the volume fraction used in the VOF method is defined as follows:

$$\gamma = \begin{cases} 0, & \text{in air} \\ 0 < \gamma < 1, & \text{on the surface} \\ 1, & \text{in water} \end{cases} \tag{3}$$

The velocity field can be obtained using the weighted averages using the equation $\vec{U} = \gamma \vec{U}_{water} + (1-\gamma)\vec{U}_{air}$. According to this equation of the velocity field, the transport equation of the VOF field can be expressed as:

$$\frac{\partial \gamma}{\partial t} + \nabla \cdot (\gamma \vec{U}) + \nabla \cdot [\gamma(1-\gamma)\vec{U}_r] = 0 \tag{4}$$

where $\vec{U}_{water}$ and $\vec{U}_{air}$ are the velocities of the corresponding water and air, respectively. $\vec{U}_r = \vec{U}_{water} - \vec{U}_{air}$ indicates the relative velocity between air and water.

The spatial variation of any fluid property ϕ (e.g., the fluid density ρ and dynamic viscosity μ) can be expressed as weighting using γ:

$$\phi = \gamma\phi_{water} + (1-\gamma)\phi_{air} \tag{5}$$

where the subscripts "water" and "air" denote the corresponding fluid property of water and air, respectively.

Body motion equations

In this study, the motion of the floating body is restricted to one degree of freedom, allowing solely the heave motion (z-direction). The vertical position of the floating box is solved using Newton's second law at the current time step n+1:

$$F^{n+1} = ma^{n+1} \tag{6}$$

where F^{n+1} is the total vertical force, and a^{n+1} is the body's vertical acceleration. Once the acceleration a^{n+1} is known, the vertical velocity v^{n+1} and vertical position z^{n+1} at the current time step n+1 are calculated using an integration strategy:

$$v^{n+1} = v^{n+1} + (1-\theta)a^n\Delta T + \theta a^{n+1}\Delta T \tag{7}$$

$$z^{n+1} = z^n + (1-\theta)v^n\Delta T + \theta v^{n+1}\Delta T \tag{8}$$

where n is the previous time step, ΔT is the time step, and θ is a blending parameter. For $\theta = 0$, the forward Euler method, which is explicit in time arises, and for $\theta = 1$, the backward Euler method, which is fully implicit in time, are employed.

Mesh motion

The mesh motion of the computational domain is calculated by solving the cell-center Laplace smoothing equation (Jasak and Tukovic, 2006):

$$\nabla \bullet (\kappa \nabla \boldsymbol{u}) = 0 \tag{9}$$

where κ is the diffusion field and $\boldsymbol{u}$ is the point velocity for modifying the point position of the mesh:

$$\boldsymbol{x}^{n+1} = \boldsymbol{x}^n + \boldsymbol{u} \cdot \Delta T \tag{10}$$

where $\boldsymbol{x}^n$ and $\boldsymbol{x}^{n+1}$ are the point positions before and after mesh motion, respectively, and ΔT is the time step.

Using the variable diffusion field κ, the deformation of each grid point is scaled from the total body displacement to no deformation. Further, κ is a function of the distance r between the center of the cell and nearest selected boundary, where $r \in (r_i, r_o)$. r_i and r_o are the inner and outer distances of the scaling, respectively.

Results

A numerical example of the Kyushu University FWT is performed applying the above method. Figure 1 shows the layout of the mooring system and the definition of the coordinate system. For comparison, natural periods of the FWT system calculated by the potential flow method are also listed in Table 1.

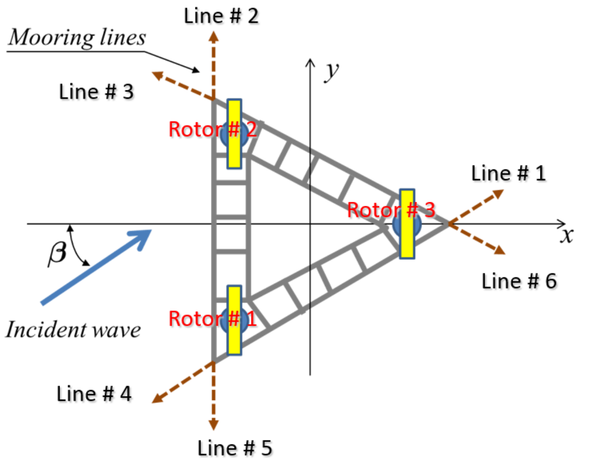

Figure 1. The layout of the mooring system of the semi-submersible FWT. The origin of the coordinate system for the subsequent analysis locates at the planar center of the triangular platform at MSL (Mean Sea Level).

Table 1. Natural frequencies of the FWT system calculated by the potential flow method.

Mode	Natural frequencies (rad/s)	
	without mooring	with mooring
Surge	-	0.07
Sway	-	0.07
Heave	0.36	0.36
Roll	0.31	0.32
Pitch	0.32	0.32
Yaw	-	0.09

Figure 2 shows a heave free decay test performed by CFD in OpenFOAM (Gao et al., 2019, 2021). Based on this figure, the heave natural period can be calculated as 17.44 s, which is very much close to the heave natural period calculated from the potential flow method, i.e., $2\pi/0.36=17.45$ s.

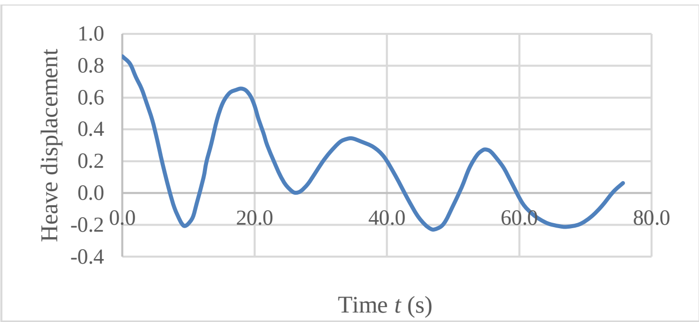

Figure 2. Free decay test simulated by CFD in OpenFOAM.

References

Goupee A., Koo B., Kimball R., Lambrakos K., Dagher H., 2014. Experimental comparison of three floating wind turbine concepts. *Journal of Offshore Mechanics and Arctic Engineering* 136(2): 020906.

Jasak, H., & Tukovic, Z. (2006). Automatic mesh motion for the unstructured finite volume method. *Transactions of FAMENA*, 30(2), 1-20.

Kim, H. C., Kim, K. H., Kim, M. H., Hong, K., 2017. Global performance of a KRISO semi-submersible multiunit floating offshore wind turbine: Numerical simulation vs. model test. *International Journal of Offshore and Polar Engineering*, 27(01), 70-81.

Liu, Y., Li, S., Yi, Q., Chen, D., 2016. Developments in semi-submersible floating foundations supporting wind turbines: A comprehensive review. *Renewable & Sustainable Energy Reviews* 60: 433–449.

Liu, Y., Yoshida, S., Yamamoto, H., Toyofuku, A., He, G., Yang, S. 2018. Response Characteristics of the DeepCwind Floating Wind Turbine Moored by a Single-Point Mooring System. *Applied Sciences*, 8(11), 648 2306.

Gao, J., Zang, J., Chen, L., Chen, Q., Ding, H., & Liu, Y. (2019). On hydrodynamic characteristics of gap resonance between two fixed bodies in close proximity. *Ocean Engineering*, 173, 28-44.

Gao, J., He, Z., Huang, X., Liu, Q., Zang, J., & Wang, G. (2021). Effects of free heave motion on wave resonance inside a narrow gap between two boxes under wave actions. *Ocean Engineering*, 224, 108753.

国際化推進共同研究概要

No.19

20RE-7

タ イ ト ル： Downwind Turbine Technologies, Model Development and Verification

研究代表者： HÖNING　Leo

所内世話人： 吉田　茂雄

研究概要：

　経済性に優れた将来の超大型風車，ならびに，導入地点を大幅に拡張する浮体式洋上風車に有望な風車のコンセプトとして，タワーの風下側にロータを配置したダウンウィンドロータが有望視されている．本ワークショップでは，風力エネルギーに関する国際共同研究プラットフォームである IEA Wind Task 40 を母体として，ダウンウィンド風車に関する技術的な課題，ならびに，得失の評価を実施している．各々の関連のテーマに関して， 2020/05/19-20，ならびに，2020/10/21-22 にワークショップを開催し，当該分野の世界最先端の技術についての情報交換，ならびに，今後の普及や標準化にあたっての討議を行った．

20RE-7 Downwind Turbine Technologies, Model Development and Verification

Applicant: Leo, Hoening, Fraunhofer IWES
RIAM Attendant: Shigeo Yoshida

1. OUTLINE OF THE WORKSHOP

1.1 Plenary Meeting, Online

(1) Date: 2020/05/19(tue)-20(wed)
(2) Place: Online (GoToMeeting)
(3) Participants:
(IWES) Leo Hoening, Bernhard Stoevesandt
(TUM) Carlo Sucameli
(X1 Wind) Rocio Torres
(NREL) Nick Johnson, Brian Smith, Pietro Bortolotti
(Hitachi) Shigehisa Funabashi, Soichiro Kiyoki, Shinya Ohara, Nobuo Namura, Takeshi Takimoto
(WEIT) Masataka Owada, Yoshitaka Totsuka
(KU RIAM) Shigeo Yoshida

1.2 Workshop, Online

(1) Date: 2020/10/21(wed)-22(thu)
(2) Place: Online (GoToMeeting)
(3) Participants:
(IWES) Leo Hoening, Bernhard Stoevesandt, Johannes Theron
(TUM) Carlo Sucameli, Helena Canet, Thorsten Lutz
(X1 Wind) Rocio Torres
(NREL) Nick Johnson, Pietro Bortolotti, Tyler Stehly
(BWC) Sandy Butterfield
(UTD) Todd Griffith
(UVA) Eric Loth
(AIST) Tetsuya Kogaki, Shigemitsu Aoki
(Hitachi) Soichiro Kiyoki, Shinya Ohara, Nobuo Namura, Takeshi Takimoto, Shinya Ohara
(WEIT) Masataka Owada, Yoshitaka Totsuka
(UTokyo) Atsushi Yamaguchi
(RCCM) Noriki Iwanaga
(KU RIAM) Shigeo Yoshida

1.3 Outlines of the Task

WP1) Model Development& Verification
  WP1-1) 2MW Baseline Turbine Model
  WP1-2) Tower Shadow
  WP1-3) Nacelle-Rotor Interaction
  WP1-4) Stability & Control
  WP1-5) Complex Terrain
WP2) Design and LCOE Assessment
  WP2-1) Blade Optimization for DTs
  WP2-2) Scalability Benefits for DTs
WP3 Recommended Practice
  WP3-1) Standards Evaluation for DTs
  WP3-2) RP for DTs

2. REPORTS

WP1-1) Baseline Model, UTokyo

Aeroelastic models of a 2MW baseline downwind turbine model were defined. Power coefficient to tip speed ratio is shown in Fig 1. The tower was designed to avoid resonance in the opration conditions as shown in Fig 2.

The Bladed and FAST models were delivered to the members to proceed the verification study in each research subject.

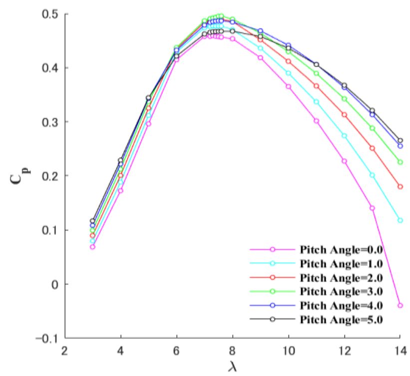

Fig 1 Power coefficient to tip speed ratio

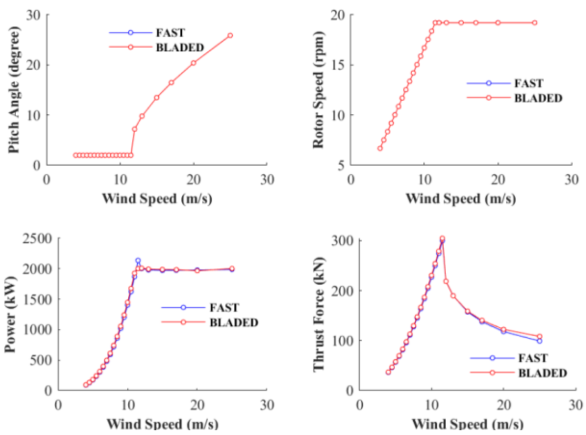

Fig 2 Steady characteristics of aeroelastic models

WP1-1) CFD Model Definition, KU

The CAD model of a 2 MW downwind turbine was provide by Hitachi. The CFD mesh which is applicabe for ANSYS Fluent was defined for the model. The rotor is rotatable using the sliding mesh around the rotor axis. Furthermore, the blades are also rotatable around the pitch axes of the 3 blades.

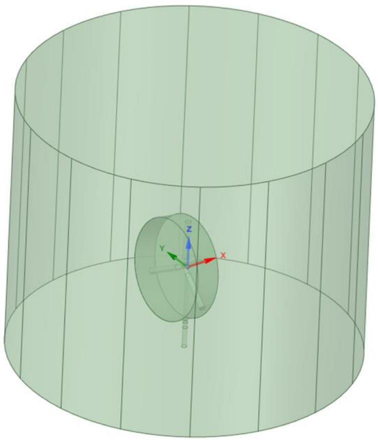

(a) CFD domain

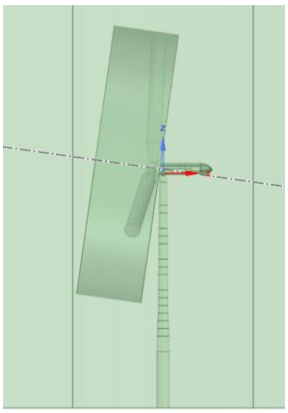

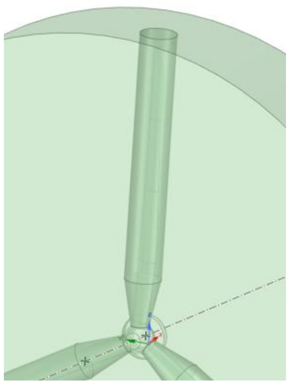

(b) Side view (c) Mesh around the blade

Fig 3 CFD model outline

Table 1 Dimensions of the CFD Model

Rotor Diameter	80 m
Hub Height	78 m
Domain Diameter	300 m
Domain Hight	240 m
Rotor Part Diameter	88 m
Rotor Part Thickness	21 m
Blade Part Length	40.3 m
Blade Part Diameter	5 m

WP1-2) CFD Result, IWES

- Model: Hitachi 2MW-80m downwind
- Wind speed: 8.6 m/s (steady)
- Pitch angle: 1.6 deg
- CFD solver: OpenFOAM
- 1/3 domain (steady), full WT (unsteady)
- Number of cells: 16million per blade

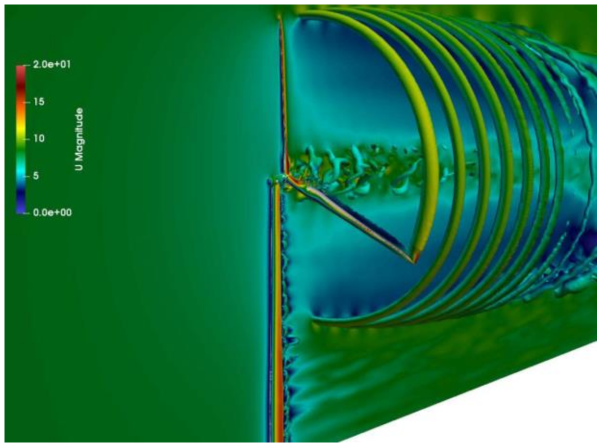

Fig 4 CFD model outline

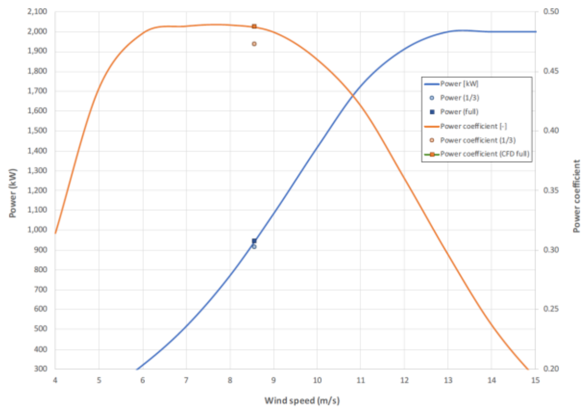

Fig 5 CFD model outline

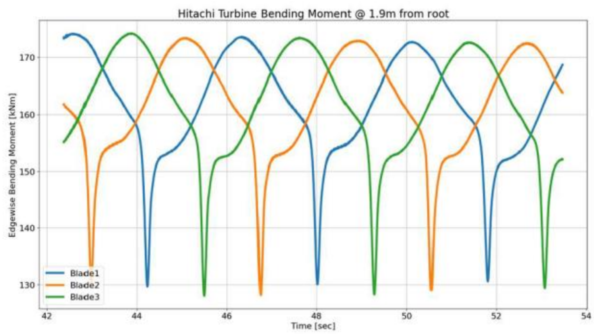

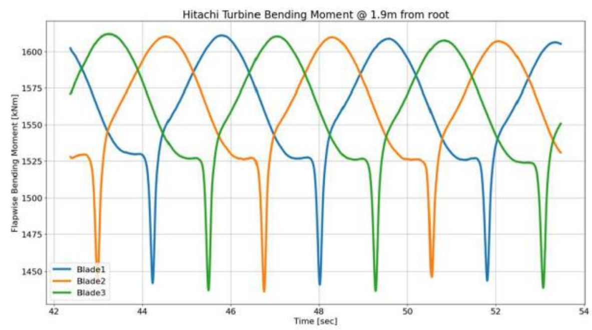

Fig 6 CFD result: blade root edgewise bending (top) and flapwisebending (bottom)

WP1-2) Tower Shadow, KU

The measurement data of a 2 MW commercial downwind turbine was provided by Hitachi. The data was analyzed.

(1) Data outlines

- Operation data: wind speed, wind direction, nacelle direction, rotor speed, pitch angle, rotor azimuth angle
- Load data: blade root flapwise/edgewise moment, tower top/base fore-aft/side-side moment

(2) Conditions

- Power generation (optimal: 8.6 m/s, rated: 16.6 m/s)
- Idling (19.9 m/s)

(3) Results

Tower shadow loads of are less remarkable as compared with those of the the prototype. Influences of wind shaer, turbulence, etc. will be studides in the future.

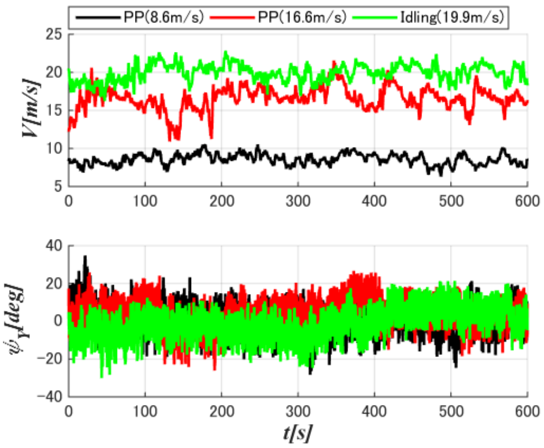

Fig 7 Field measurement data of a 2MW downwind turbine

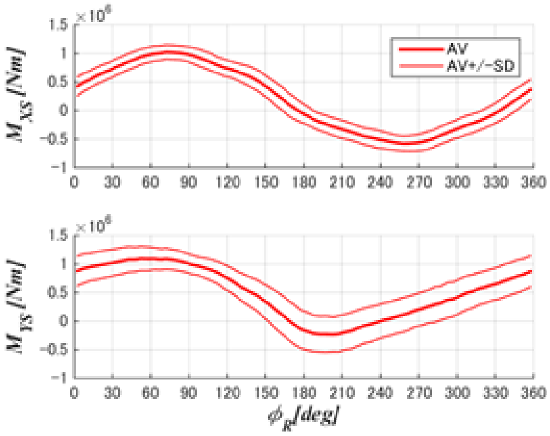

Fig 8 Blade root bending moments of the 2 MW commercial downwind turbine

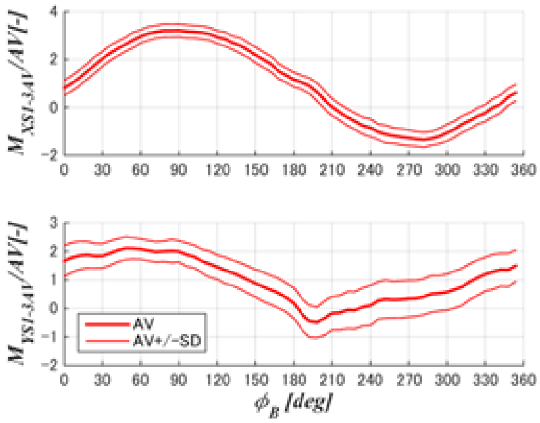

Fig 9 Blade root bending moments of the 2 MW ptotype downwind turbine as the reference

WP1-2) Tower Shadow, KU

Some research results on tower shadow modeling of downwind turbines in Blade-Element and Momentum (BEM) method, which was not considered in the former methods were reported.

(1) Load Equivalent Model [1]

The load equivalent model tower shadow model was introduced. The wind speed profile of the tower wake is defined based on the load fluctuation calculated by the CFD. It showed good agreement with the measurement.

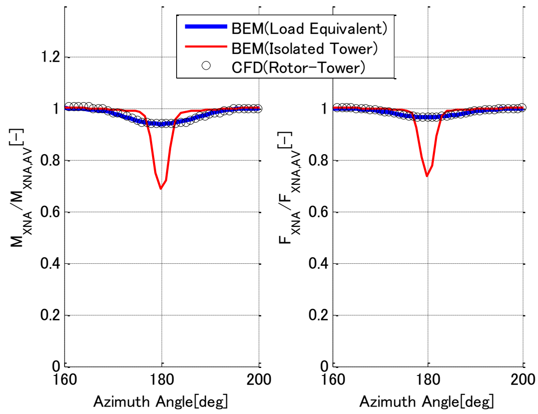

Fig 10 Rotor thrust and torque of a downwind turbine stiff model around the tower shadow at 13 m/s

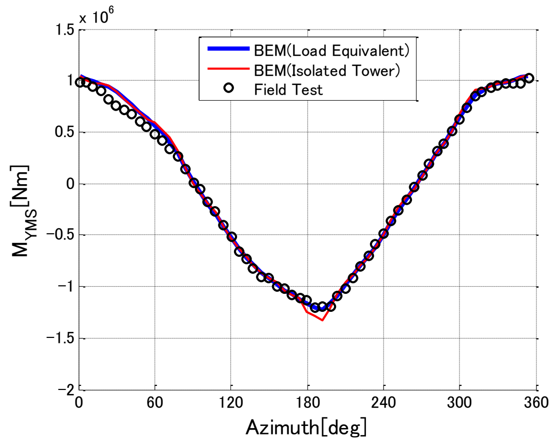

Fig 11 Mainshaft bending a 2 MW prototype downwind turbine at 13 m/s

(1) Tower Variable Load [2]

The variable load model of downwind turbine tower, which was not considered in the previous model, is formulated as below, using lifting-line theory.

$$\Delta C_{dT} = \frac{\pi D_T}{2 U_0^{\,2}} \left(-U_0 \frac{du}{dx_T} + r\Omega \frac{dv}{dx_T} - w \frac{dw}{dx_T} \right)$$

It was verified by the CFD of rotor-tower-nacelle configurations at rated and cut-out operating conditions. It shows fairly nice agreement with the CFD in particular out-board section and at low thrust conditions as shown in Fig 13. However, there still be some more room for improvement in inboard sections.

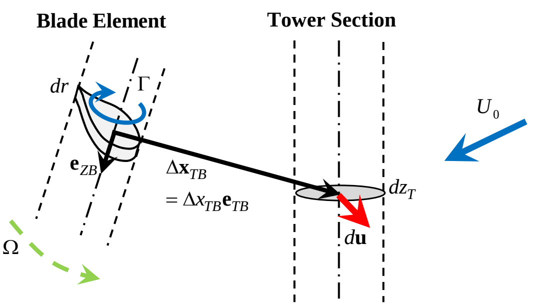

Fig 12 Outlines of the model

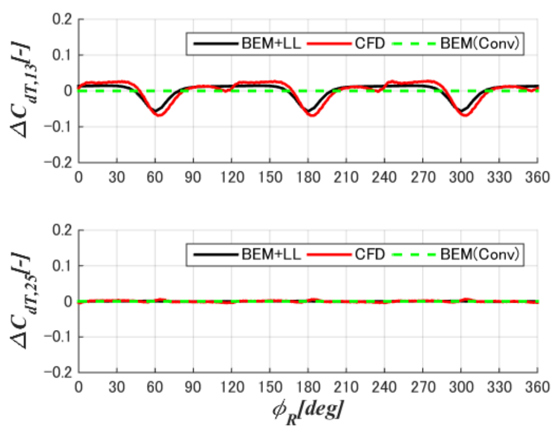

Fig 13 Variable loads of the downwind turbine tower at 100% rotor radius: (T) 13 m/s, (B) 25 m/s

(2) Tower Average Load [3]

The average tower load model was also introduced based on the momentum theory, which consists with velocity and pressure gradient terms.

$$\begin{aligned} \Delta C_{dTV} &= \Delta C_{dTV} + \Delta C_{dTP} \\ &= -C_{dT0}\left(1-\mu_T^{\,2}\right) + \frac{\pi}{2}\mu_T \frac{d\mu_T}{d\xi_T} \end{aligned}$$

The model was validated by the wind tunnel test. It shows good agreement with the wind tunnel test data as shown in Fig 14.

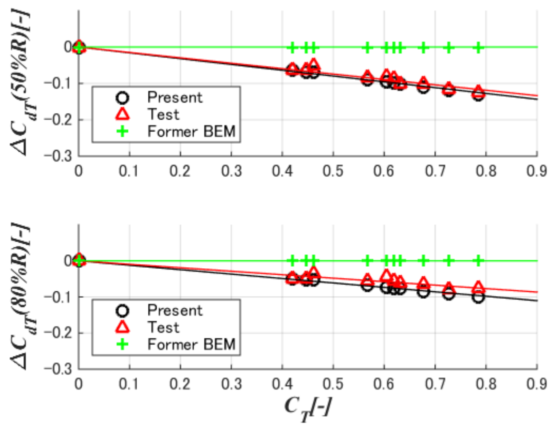

Fig 14 Rotor thrust to tower drag: (T) 13m/s, (B) 25 m/s

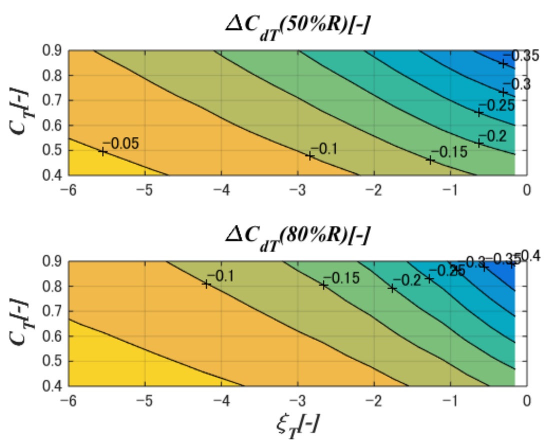

Fig 15 Tower section drag to the rotor thrust and the clearance between the rotor and the tower: (T) 50 %R, (B) 80 %R

(3) Dynamic Blade Load [4]

The dynamic blade load model was reported. This model was developed based on the former study of Munduate [5]. Two points were modified from the reference; 1) application of Moriarty's tower wake model [6] and 2) wake entrance condition. Fig 16 shows the analysis and experiment results on a 1.0 m diameter model. Where, UG indicates University Glasgow's former model and KU does present model. The present model was successfully shown the increase in load before the wake entrance was modeled better than the previous work.

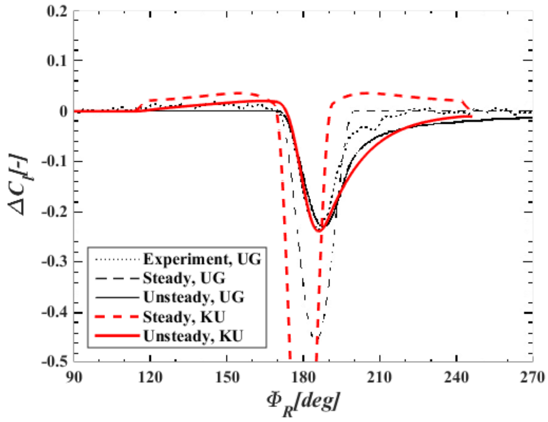

Fig 16 Blade section (75% rotor radius) lift coefficient to rotor azimuth, UG model

The scale effects of the model were investigated. Fig 17 is the simulation results for the similar models. The top, middle and bottom subplots are analysis results with x1 model (1 m rotor diameter), x3 (3 m), and x10 (10m), respectively. Here the tip speeds are set to be identical. As shown in these figures, the variation of the lift coefficients are decreasing as the scale getting larger.

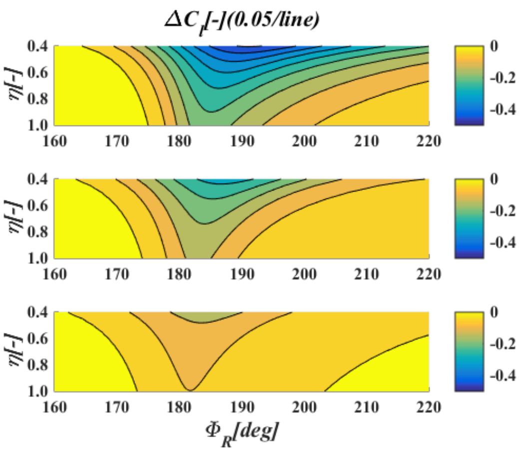

Fig 17 Blade section lift coefficient to rotor azimuth: scale (T) x1, (M) x3, (B) x10, KU model

WP1-4) Stability, Hitachi [7][8]

The extreme loads of a 5.2 MW DT in parked condition in Typhoon #21 in 2017 were simulated. Yaw angles by the measurement and the analysis are shown in Fig 20. Blade root flapwise bending moment are shown in Fig 22. The results are consistent with the measurement.

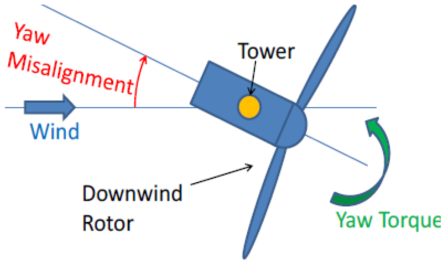

Fig 18 Passive yaw (free yaw)

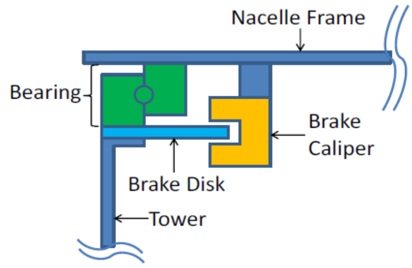

Fig 19 Typical yaw system

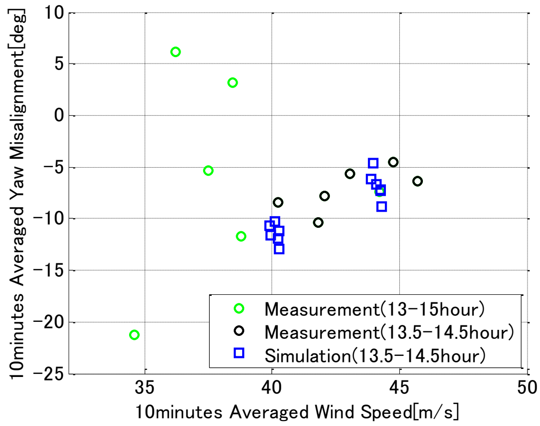

Fig 20 Yaw misalignment to wind speed

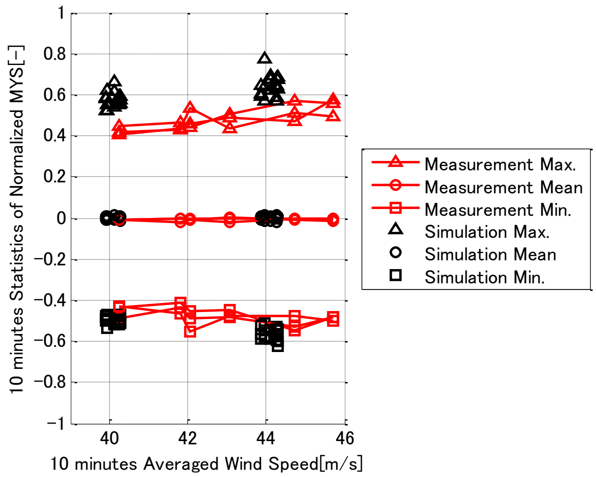

Fig 21 Blade root flapwise bending to wind direction

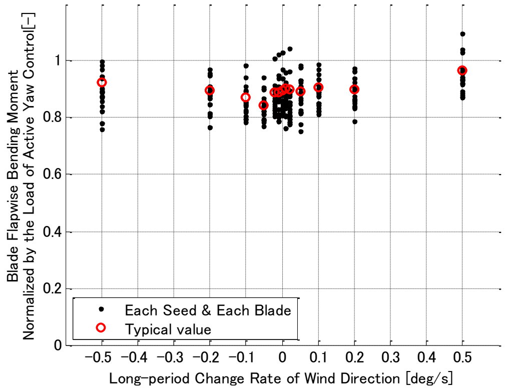

Fig 22 Blade root flapwise bending to wind direction change rate

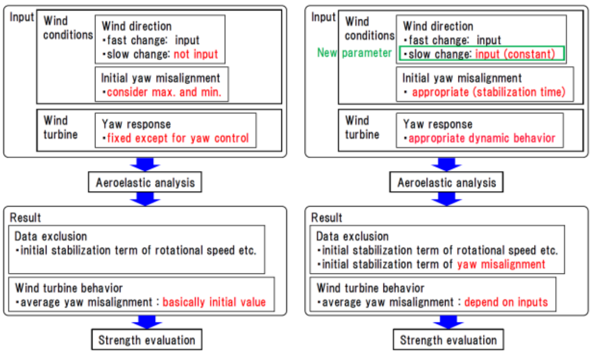

Fig 23 Recommendation for analysis of passive yaw idling in storm

WP2-2) Scalability Benefits, Hitachi[9]

1. Outlines

Fatigue calculation and tower shadow model were introduced in this research. Natural frequencies in flap-wise and edgewise are the output of the optimization. Design variables are not optimized for pre-bent blades as present cost is not considered. Less than 5m is recommended due to the manufacturing and transportation. The tower shadow model is too pessimistic. Therefore, the advantage of downwind turbines is underestimation.

WISDEM, the system engineering code developed by NREL, was modified to consider the tower shadow effect of downwind turbines.

2. Conditions

- Wind class: 1A
- Downwind: prebent 0 m
- Upwind-1: prebend max 6 m
- Upwind-2: prebend max 20 m

3. Results

Downwind turbine shows lower LCoE than upwind turbines.

Here, the cost of the production and transportation of the prebent blades are still not considered in the cost model of the prebent blades. Therefore, LCoE of the upwind turbines are estimated a little optimistic.

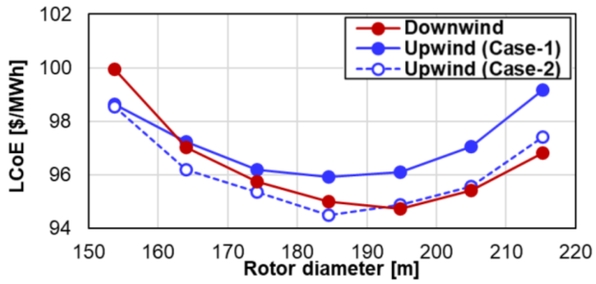

Fig 24 LCoE to rotor diameter

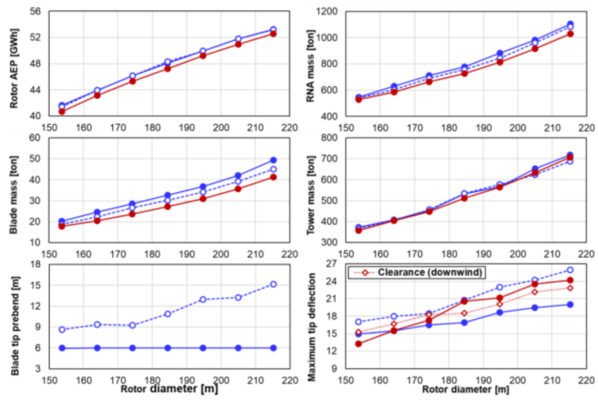

Fig 25 Design parameters to the rotor diameter

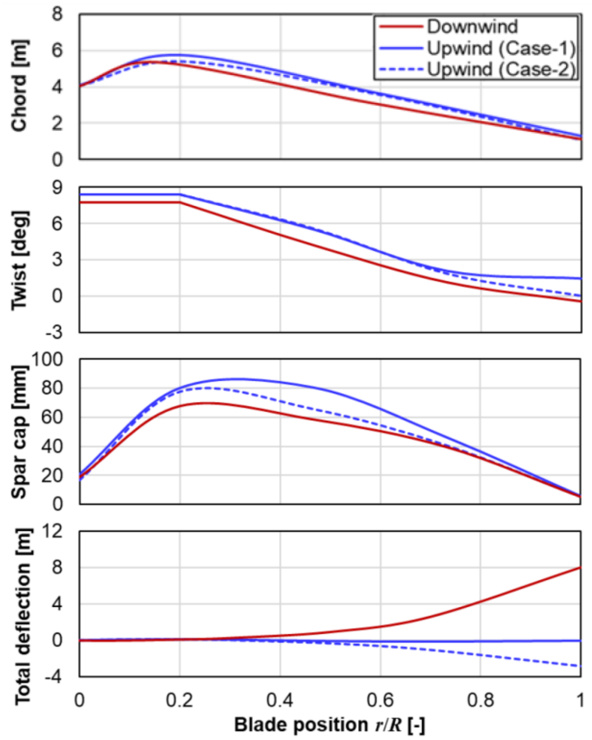

Fig 26 Optimal blade shapes

WP2-2) Largest Wind Turbine, UVA[10]

Morphing blades, which adapt the alignment of the blade in acoordance with the thrust and the centrifugal forces, are promising concept for super large wind turbines.

The studies in SUMR show promising results, such as 27% RNA mass reduction and 24% LCoE reduction, bu the fatigue load reduction.

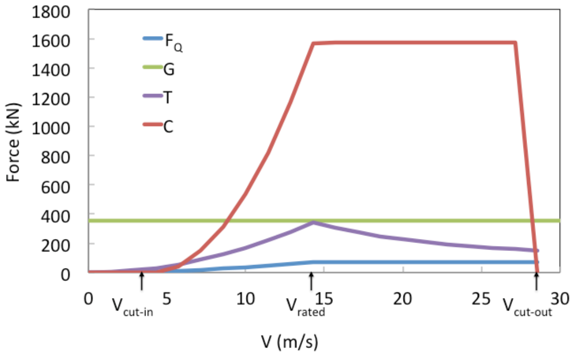

Fig 27 Typical force to wind speed

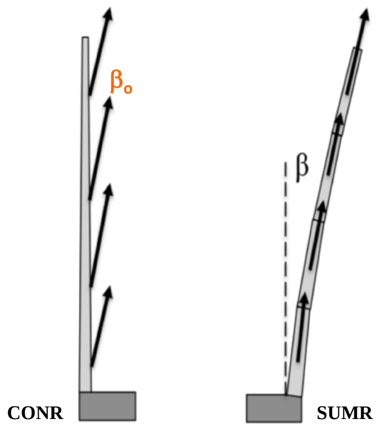

Fig 28 Concept of the SUMR blade

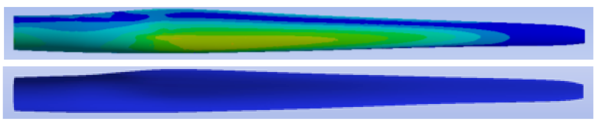

Fig 29 von Mises stress of CONR (top) and SUMR (bottom)

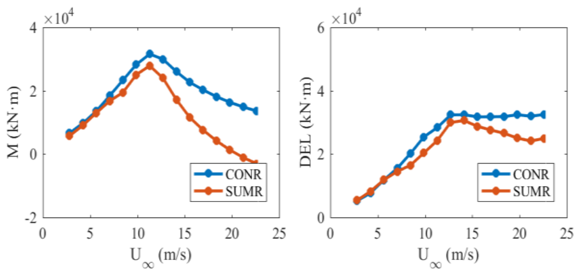

Fig 30 Average moment (left) and its DEL (right) to wind speed

Table 2 Dimensions of the CFD Model

	CONR 3-Blades	SUMR 2-Blades
Rotor Mass	100%	73%
Power Output	100%	98%
LCoE	100%	76%

3. REFERNCES

[1] Yoshida, S., Load Equivalent Tower Shadow Modeling for Downwind Turbines, European Wind Energy Conference, 2007.

[2] Yoshida, S., Combined Blade-Element Momentum - Lifting Line Model for Variable Loads on Downwind Turbine Towers, energies, 2018.

[3] Yoshida, S., et al., Rotor Thrust Effects on Mean Load of Downwind Turbine Towers, #40 Wind Energy Utilization Symposium, 2018.

[4] Yoshida, S., et al., Unsteady Tower Shadow Model for Downwind Turbines, #41 Wind Energy Utilization Symposium, 2019.

[5] Munduate, X., Coton, F.N., Galbraith, R.A.M., An Investigation of the Aerodynamic Responses of a Wind Turbine Blade to Tower Shadow, J. Solar Energy Engineering, 126, 1034-1040, 2004.

[6] Moriarty, P.J. and Hansen, A.C., AeroDyn Theory Manual, NREL/EL-500-36881, National Renewable Energy Laboratory, 2005.

[7] Kiyoki, S., et al., Evaluation of wind loads by a passive yaw control at the extreme wind speed condition and its verification by measurement, GRE2018, 2018.

[8] Okuno, A., et al., alidation of Extreme Loads of Wind Turbine by Measurement Data and Simulation, JWEA Wind Energy Utilization Symposium 2018.

[9] Namura, N., Shinozaki, Y., Design Optimization of 10MW Downwind Turbines with Flexible Blades and Comparison with Upwind Turbines, J.Phys.: Conf. Ser. 1618 042021, 2020.

[10] Noyes, C., et al., Analytic analysis of load alignment for coning extreme - scale rotors, Wind Energy, 2020:23:357-369, 2020.

国際化推進共同研究概要

No.20

20RE-8

タ イ ト ル： A Machine Learning based Software-In-the-Loop method to Predict dynamic responses of floating wind turbine

研究代表者： HU Zhiqiang

所内世話人： 胡　長洪

研究概要：

浮体式洋上風力発電システム用のセミサブ型浮体の運動特性解析に機械学習を応用する国際化推進共同研究について今年度は予定通り実施した。特に、Software-In-the-Loop-Simulation 手法に対して検討を行い、有望な成果が得られた。R3 年１月に応研で開催されたオンライン国際研究集会「The 2nd International Symposium on Novel Computational and Experimental Methods for Complicated Fluid-Structure Interactions」に参加し、「A Software-in-the-Loop Combined Reinforcement Learning Method for Dynamic Response Analysis of Floating Wind Turbines」のタイトルで共同利用成果の発表を行い、参加者との研究交流を行った。

Report for 2020 RIAM International Joint Research Project

[20RE-8]

A Machine Learning based Software-In-the-Loop method to Predict dynamic responses of floating wind turbine

Zhiqiang Hu
Marine, Offshore and Subsea Technology, School of Engineering, Newcastle University, UK

During year of 2020, although the pandemic brought some negative influences on the international collaborations, but the collaborative works between RIAM Kyushu University and Newcastle University have been carrying out steadily. The outcomes are listed as below.

1) Attendance of The 2nd International Symposium on Novel Computational and Experimental Methods for Complicated Fluid-Structure Interactions, at RIAM Kyushu University in Jan 2021 and was held online.

2) During the collaborative research in year 2020, a new AI technology-based method, named SADA, was proposed for the prediction of dynamic responses of FOWTs. Currently, it is SADA version 1.0. The methodology of SADA starts with the selection of Key Disciplinary Parameters (KDPs). The AI module in SADA was built by a coupled aero-hydro-servo-elastic in-house program *DARwind* with the machine learning algorithms deep deterministic policy gradient (DDPG). This latest research outcome has been presented in the RIAM conference in Jan 2021.

3) Based on the research in year 2020, a collaborative conference paper entitled 'Software-in-the-Loop combined Machine learning for Dynamic Responses Analysis of Floating Offshore Wind Turbines' OMAE2021-65524 has been submitted to OMAE Conference 2021. Prof Changhong Hu is the co-author of this paper. At this moment, the paper is under the revision status. If it can be accepted, it will be presented by Mr. Peng Chen, a PhD student of Zhiqiang Hu at Newcastle University in June 2021.

1. RIAM international symposium

The 2nd International Symposium on Novel Computational and Experimental Methods for Complicated Fluid-Structure Interactions was successfully held online on 29th Jan 2021. Professor Zhiqiang Hu attended this symposium and gave an presentation with topic on 'Software-in-the-Loop combined Reinforcement Learning Method for Dynamic Response Analysis of Floating Wind Turbines'. This presentation introduced the collaborative research outcomes of Zhiqiang Hu's research team at Newcastle University and Professor Changhong Hu's research team at Kyushu University during year 2020. This presentation introduced the in-depth knowledge, structure of SADA and challenges need to be overcome in the future. After the presentation, Zhiqiang Hu made fruitful discussions with other scholars online. After the symposium, professor Changhong Hu and Zhiqiang also made a detailed discussion and confirmed to continue the collaborative research in the field of AI-based knowledge and floating wind turbines.

2. Collaborative research on AI technology for floating wind turbine

In the year of 2020, a collaborative research on AI-based technology for dynamic responses analysis of floating wind turbine was conducted very well and fruitful research outcomes have been achieved. The SADA method is newly proposed for the prediction of dynamic responses of FOWTs with a smart application of artificial intelligence technology. Another new skill, the selection of Key Disciplinary Parameters (KDPs) is also proposed as the first key skill in SADA. The AI module in SADA was built by a coupled aero-hydro-servo-elastic in-house program DARwind with the machine learning algorithms deep deterministic policy gradient (DDPG). Basin experimental data was used in SADA for the AI training. The SADA method was used to analyze the dynamic responses of Hywind 5MW wind turbine and the results showed very satisfactory.

In addition, thanks for the support and collaboration in 2020, a collaborative conference paper submitted to the 40th International Conference on Ocean, Offshore and Arctic Engineering (OMAE2021). The paper is titled 'Software-in-the-Loop combined Machine learning for Dynamic Responses Analysis of Floating Offshore Wind Turbines'. This paper is under revision status. If it can be accepted for publication, the first author will give a presentation online in the OMAE2021 conference.

In year 2021, the collaborative research will be conducted to a further step. Currently, there are still some challenges in the anticipation of using SADA method for a higher accuracy. Some investigations on statistical criterion application in error estimation will be conducted as a priority. The aerodynamic influence will also be investigated to a further detailed extend. The AI technology application in offshore renewable energy is also the strong side of Professor Changhong Hu's research team. So, it is expected the novel method currently proposed will have a potential opportunity to be used in some other offshore renewable energy facilities, such as ocean wave energy converter.

国際化推進共同研究概要

No.21

20RE-9

タイトル： Novel computational and experimental approaches to the analysis of complicated fluid-structure interactions

研究代表者： WAN Decheng

所内世話人： 胡 長洪

研究概要：

本国際化推進共同研究について今年度は 2 年目で，共同研究・研究集会とも予定通り実施した。共同研究について、海洋工学分野での流体・構造連成解析問題に関する CFD 手法開発に関する検討が行われ、関連の研究成果は４編の国際学会論文に纏められ採択された。R3 年 1 月 29 日にオンライン国際研究集会「The 2nd International Symposium on Novel Computational and Experimental Methods for Complicated Fluid-Structure Interactions」が開催され、外国から 22 名、日本から 25 名の参加者があり、流体・構造連成解析問題に関する数値解析方法及び水槽実験方法の高精度化・高効率化に関して有意義な国際研究集会となった。

Report for 2020 RIAM International Joint Research Project

[20RE-9]

Novel computational and experimental approaches to the analysis of complicated fluid-structure interactions

Decheng Wan
School of Naval Architecture, Ocean and Civil Engineering, Shanghai Jiao Tong University, China

1. Purpose

Marine renewable energy devices are usually installed in a sea area where severe environmental conditions have to be considered. On the other hand, cost control is strictly required for those devices in order to pass economic evaluations. Therefore for successful design of those devices, accurate numerical methods as well as efficient experimental methods are required to evaluate the hydro- and aerodynamic performance of these devices. This joint research project focuses on one of the most important fundamental fluid mechanics problems in marine renewable energy development, the fluid-structure interaction problem. Researchers, especially younger researchers, including but not limited to SJTU and RIAM, are invited to exchange their knowhow on development of computational and experimental tools for the purpose.

2. Research Plan

This joint research project is planned for two years. FY2020 is the second year of the project. Besides continuing comparison and discussion of the existing CFD codes which are developed in SJTU and RIAM, emphasis of this year's joint research will be on discussion of the future CFD and experimental methods for analysis of complicated fluid-structure interaction problems in ocean engineering and marine renewable energy developments. In the end of FY2020, as the main event of this international joint research project, International RIAM Symposium on Novel Computational and Experimental Methods for Complicated Fluid-Structure Interactions will been carried out. Researchers involved in this joint research project will present and discuss their research progresses.

The members involved in this collaborative research are shown in the following table.

Researcher's Name	Name of University or Institute	Present Status or Grade (graduate students)	Researcher role
Decheng Wan	SJTU	Professor	Representative person (CFD)
Jianhua Wang	SJTU	Assistant Professor	Co-researcher (CFD)
Cheng Liu	SJTU	Associate Professor	Co-researcher (CFD)
Weiwen Zhao	SJTU	Assistant Professor	Co-researcher (CFD)
Liushuai Cao	SJTU	Assistant Professor	Co-researcher (CFD)
Xiaosong Zhang	SJTU	PhD student	Co-researcher (CFD)
Xiaobin Yang	SJTU	PhD student	Co-researcher (CFD)
Jinqi Li	SJTU	PhD student	Co-researcher (CFD)
Seiya Watanabe	RIAM	Assistant professor	Co-researcher (CFD)

Mohamed M. Kamra	RIAM	Research Fellow	Co-researcher (CFD)
Hongzhong Zhu	RIAM	Research Fellow	Co-researcher (Experiment)
Changhong Hu	RIAM	Professor	RIAM Attendant

3. Summary of Collaboration Research

In 2020, due to the international travel restriction, research discussions have been made online. Main topics that have been studied include (1) Numerical simulation of interaction between internal solitary waves and uniform bottom slope by MPS method; (2) RANS simulation and LES of tip vortex cavitation around hydrofoil; (3) development of a numerical model for simulation of vortex-induced vibration (VIV) of a long flexible riser under offshore platform horizontal motion; and (4) Multi-objective hull form optimization analysis of a trimaran's total drag at different speeds by CFD simulations. The research results have been presented at the 2020 ISOPE conference and the 2nd International Symposium on Novel Computational and Experimental Methods for Complicated Fluid-Structure Interactions.

International conference papers related to this joint research project in 2020 are listed as follows.

1) Xinze Duan, Jianhua Wang, Decheng Wan, CFD Investigations of Wake Flow Interactions in a Wind Farm with 14 Wind Turbines, International Journal of Offshore and Polar Engineering, 2020, 30(3): 257–265;
2) Yang Huang, Decheng Wan, Investigation of Interference Effects between Wind Turbine and Spar-Type Floating Platform under Combined Wind-Wave Excitation, Sustainability, 2020, 12(1), 246;
3) Xiao Wen, Decheng Wan, Changhong Hu, Numerical Study of Interaction between Internal Solitary Waves and Uniform Slope by MPS Method, Proceeding the Thirtieth (2020) International Ocean and Polar Engineering Conference Shanghai, China, October 11-16, 2020, pp.1986-1993
4) Shang Liang, Decheng Wan, Changhong Hu, CFD Study of Tip Vortex Cavitation around Hydrofoil, Proceeding the Thirtieth (2020) International Ocean and Polar Engineering Conference Shanghai, China, October 11-16, 2020, pp.2345-2351
5) Yuqi Zhang, Decheng Wan, Changhong Hu, Numerical Study of Vortex-Induced Vibration of a Flexible Riser under Offshore Platform Horizontal Motion, Proceeding the Thirtieth (2020) International Ocean and Polar Engineering Conference Shanghai, China, October 11-16, 2020, pp.2555-2562
6) Xinwang Liu, Decheng Wan, Changhong Hu, Multi-Objective Hull Form Optimization of Trimaran's Total Drag at Different Speeds, Proceeding the Thirtieth (2020) International Ocean and Polar Engineering Conference Shanghai, China, October 11-16, 2020, pp.3850-3857

As a main event of this international joint research project, 'The 2nd International Symposium on Novel Computational and Experimental Methods for Complicated Fluid-Structure Interactions' was held on January 29, 2021. Due to the global pandemic situation of COVID-19, the symposium has been held online. On the symposium, overseas and domestic scholars have been invited to present their recent researches on their recent research results on development of computational and experimental methods for complicated fluid-structure interactions. The program of the symposium is as follows.

The 2nd International Symposium on Novel Computational and Experimental Methods for Complicated Fluid-Structure Interactions

Date: January 29, 2021

Place: Zoom Meeting Room (From 9:00 Japan time)

Organized by Research Institute for Applied Mechanics, Kyushu University

TIME TABLE

9:30 - 9:35	Opening Address by Changhong Hu

Session 1	***Next Generation CFD Development***
9:35 - 10:30	**Feng Xiao** (Tokyo Institute of Technology) *Invited Lecture* Design New Fidelity Numerical Schemes by BVD Principle
10:30 - 10:55	**Jabir Salami**, Mohamed Kamra, Changhong Hu (Kyushu University) Development of Flux Reconstruction Method for Multiphase Flows
10:55 - 11:20	**Zheng Li,** Cheng Liu, Decheng Wan (Shanghai Jiao Tong University, China) High-Fidelity Numerical Simulation of Hydraulic Jump Phenomenon of a Surface-Piercing NACA Foil
11:20 - 11:45	**Yunong Xiong** (Tokyo Institute of Technology) Unify VOF and Level Set using THINC Scaling Method
11:45 - 12:10	**Xizeng Zhao** (Zhejiang University, China) Development of Three-Dimensional Wave Tank based on VPM-THINC/QQ Method and its Application

12:10 - 13:30	Lunch break

Session 2 ***Computational Fluid Structure Interaction***

13:30 - 13:55	**Seiya Watanabe** (RIAM, Kyushu University) A Cumulant Lattice Boltzmann Method for Free Surface Impact Pressure Prediction
13:55 - 14:20	**Yudai Yokoyama** and Takahito Iida (Osaka University) Verification of Enhanced MPS solver in Wedge Slamming for Development of Fluid-Ice-Ship Interaction Problem
14:20 - 14:45	**Xiaosong Zhang,** Jianhua Wang, Decheng Wan (Shanghai Jiao Tong University, China) A hybrid VOF/E-L Method for Simulating Complex Multiscale Bubbly Flows
14:45 - 15:10	**Tomoaki Hirakawa** (Akita University) A Boundary Element Method for Interaction of Wave and Arbitrary Shape Bodies

15:10 - 15:20	Break

Session 3 ***Ocean Renewable Energy Technologies***

15:20 - 15:45	**Yusaku Kyozuka,** Daisaku Sakaguchi (Nagasaki University) Demonstration Experiments of a Floating/Submersible Tidal Current Power System in Naru-Strait in Goto, Nagasaki
15:45 – 16:10	**Ali Alkhabbaz**, Byung Ha Kim, Ho Seong Yang, Young-Ho LEE (Korea Maritime & Ocean University, Korea) Concept Design Experiences of 8MW Floating Offshore Wind Platform at Korea Western Sea
16:10 - 16:35	**Yang lin**, Ma qingwei, Liao kangping (Harbin Engineering University, China) Aero-Elastic Modeling of FOWT using Classic Rotational Beam Theory and Finite Element Method
16:35 - 17:00	**Hongzong Zhu** (RIAM, Kyushu University) A Unified Seakeeping and Maneuvering Analysis of Multiple Linked Towing System with Triangular Bodies
17:00 - 17:25	**Zhiqiang Hu** (Newcastle University, UK) Software-in-the-Loop Combined Reinforcement Learning Method for Dynamic Response Analysis of Floating Wind Turbines

17:25 - 17:30	Closing Address by Decheng Wan

国際化推進共同研究概要

No. 22

20RE-10

タ イ ト ル： Flexible energy harvesting system

研究代表者： JEON Insu

所内世話人： 東藤　貢

研 究 概 要 ：　本研究では、天然高分子のセルロースと合成高分子の poly(3,4-ethylenedioxythiophene)-poly(styrenesulfonate)を原料として新しい製造方法を用いて新規ゲル材料を作製した。作製したゲルはすぐれた弾性率、強度、電気伝導性を示し、さらに-50～35℃の範囲でゲル状態を維持することが可能であった。このゲルは次世代の柔軟性を示す構造体用材料としての使用可能性が示唆された。

Flexible energy harvesting system

Chonam National University, Prof. Insu Jeon

Summary

In this research, we have developed a novel class of gels through a new fabrication route. The gels were synthesized by integrating cellulose, a natural biopolymer, with poly(3,4-ethylenedioxythiophene)-poly(styrenesulfonate), an exceptionally conductive and biocompatible synthetic polymer, in tripropylene glycol, a green organic solvent with extremely high-boiling and low-freezing temperature. The prepared gels exhibited properties with the highest Young's modulus, tensile strength, and electrical conductivity of ~500 MPa, ~55 MPa, and ~200 S m^{-1}, respectively. Moreover, the gels maintained their properties for 14 d over a wide temperature range (−50 to 35 °C), covering almost the entire atmospheric temperature range on Earth. Owing to these remarkable properties, the developed gels are prominent candidates for many applications in next-generation flexible devices.

Method

First, isotropic water-equilibrated (Cellulose/PEDOT:PSS)(x/y) hydrogels were prepared (the detailed procedure is described in the Supporting Information). The hydrogels were subsequently immersed in TriPG (tripropylene glycol) solvent for ~2 d for solvent exchange with several TriPG solvent replacements. Lastly, the gels were stabilized in air at ~25 °C for 1 d to obtain the desired isotropic (Cellulose/PEDOT:PSS) TriPG gels, which were subjected to subsequent characterization.

Results

To fabricate a TriPG gel with optimal composition, we prepared a series of (Cellulose/PEDOT:PSS)(x/y) TriPG gels (where x and y are the initial cellulose and PEDOT:PSS concentrations (wt%), respectively) using the steps illustrated in Figure 1, and analyzed their properties utilizing tensile tests, and electrical conductivity measurements.

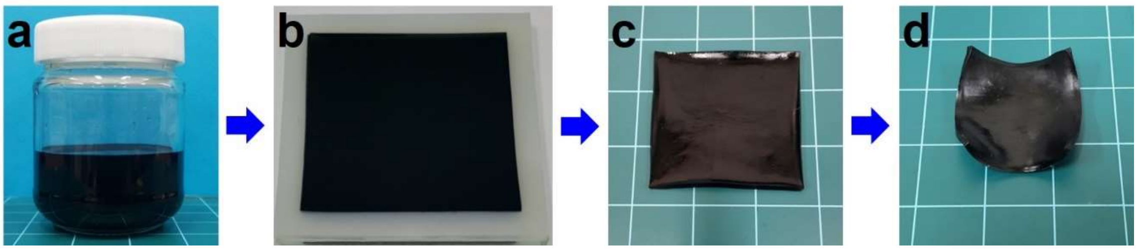

Figure 1. Fabrication process of (Cellulose/PEDOT:PSS)(x/y) TriPG gels.

When the PEDOT:PSS concentration was increased from 0 to 1 wt% at a set cellulose concentration of 1.5 wt%, the Young's modulus, tensile strength, and work of extension of the TriPG gels increased gradually (Figure 2). However, when the cellulose concentration was increased from 0.5 to 1.5 wt% and the PEDOT:PSS concentration was set to 1 wt%, the mechanical properties of both the TriPG gels increased gradually. These changes in mechanical properties of the gels were in line with the changes in the final solvent content of the TriPG gels. Our composition variation study indicated that TriPG can serve as a good solvent for integrating both cellulose and PEDOT:PSS in gel materials, despite their highly contrasting chemical structures. Therefore, the mechanical properties of the TriPG gels increased proportionally with the concentrations of cellulose and PEDOT:PSS. Because cellulose is electrically non-conductive and PEDOT:PSS is highly conductive, the electrical conductivity of the TriPG gels and corresponding hydrogels strongly depended on the final PEDOT:PSS concentration and relative cellulose and PEDOT:PSS concentration in the gels.

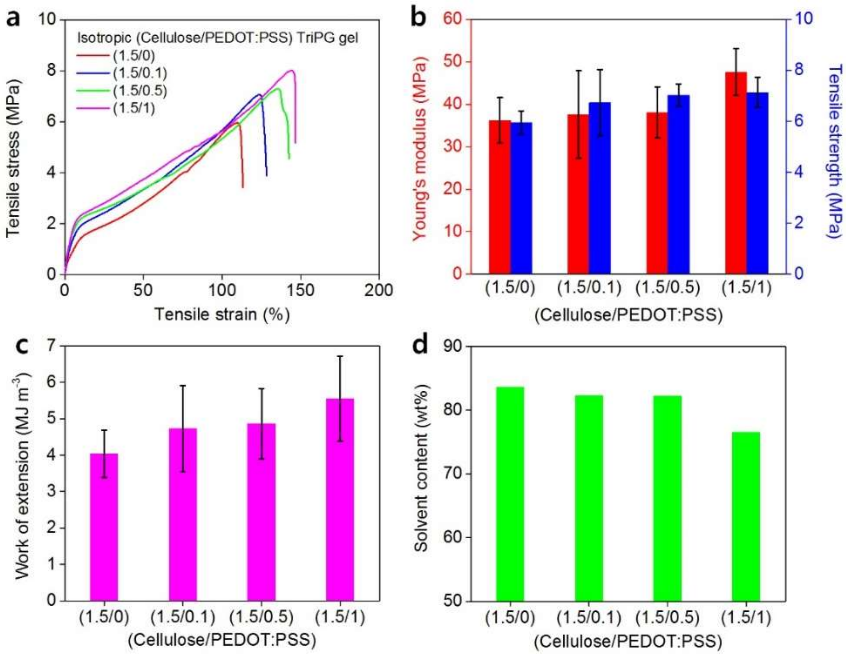

Figure 2. (a) Typical tensile stress–strain curves of the isotropic (Cellulose/PEDOT:PSS) TriPG gels prepared by varying the PEDOT:PSS concentration in the range of 0–1 wt% at a set cellulose concentration of 1.5 wt%. (b) Young's modulus and tensile strength, (c) work of extension, and (d) solvent content of prepared (Cellulose/PEDOT:PSS)(x/y) TriPG gels.

Conclusion

We successfully developed a novel class of gels by integrating cellulose and PEDOT:PSS, which are bio-friendly high-value polymers, in TriPG, a green organic solvent. Despite the significant differences in structure and properties of the polymers, the novel fabrication method proposed in this study allowed us to fabricate a hybrid gel with excellent mechanical and electrical properties, and extremely high stability over a wide temperature range. Considering these remarkable properties and facile synthesis, the developed gels are expected to have high potential for numerous applications in next-generation flexible devices.